A Platform for Robot-Assisted Intracardiac Catheter Navigation

by

Yusof Ganji

A thesis
presented to the University of Waterloo
in fulfillment of the
thesis requirement for the degree of
Doctor of Philosophy
in
Electrical and Computer Engineering

Waterloo, Ontario, Canada, 2009

I hereby declare that I am the sole author of this thesis. This is a true copy of the thesis, including any required final revisions, as accepted by my examiners.

I understand that my thesis may be made electronically available to the public.

Abstract

Steerable catheters are routinely deployed in the treatment of cardiac arrhythmias. During invasive electrophysiology studies, the catheter handle is manipulated by an interventionalist to guide the catheter's distal section toward endocardium for pacing and ablation. Catheter manipulation requires dexterity and experience, and exposes the interventionalist to ionizing radiation. Through the course of this research, a platform was developed to assist and enhance the navigation of the catheter inside the cardiac chambers. This robotic platform replaces the interventionalist's hand in catheter manipulation and provides the option to force the catheter tip in arbitrary directions using a 3D input device or to automatically navigate the catheter to desired positions within a cardiac chamber by commanding the software to do so. To accomplish catheter navigation, the catheter was modeled as a continuum manipulator, and utilizing robot kinematics, catheter tip position control was designed and implemented. An electromagnetic tracking system was utilized to measure the position and orientation of two key points in catheter model, for position feedback to the control system. A software platform was developed to implement the navigation and control strategies and to interface with the robot, the 3D input device and the tracking system. The catheter modeling was validated through in-vitro experiments with a static phantom, and in-vivo experiments on three live swines. The feasibility of automatic navigation was also verified by navigating to three landmarks in the beating heart of swine subjects, and comparing their performance with that of an experienced interventionalist using quasi biplane fluoroscopy. The platform realizes automatic, assisted, and motorized navigation under the interventionalist's control, thus reducing the dependence of successful navigation on the dexterity and manipulation skills of the interventionalist, and providing a means to reduce the exposure to X-ray radiation. Upon further development, the platform could be adopted for human deployment.

Acknowledgements

First and foremost, I gratefully acknowledge the supervision of Prof. Farrokh J. Sharifi, whose support and guidance made this ambitious project a reality. I also offer my gratitude to my co-supervisor, Prof. Safieddin Safavi-Naeini whose advice and mentorship helped me pass through the difficulties and obstacles of the project.

In my advisory committee, I express my gratitude toward Prof. Hamid R. Tizhoosh for his kind advice, whenever I asked for it. I also thank Prof. Daniel E. Davison and Prof. Otman Basir for their support and encouragement in this research.

It is my pleasure to convey my sincere gratitude to Dr. Asim N. Cheema, Interventional Cardiologist with St. Michael's Hospital in Toronto, for his generous guidance, contributions, and support, his invaluable collaboration, and his genuine interest that made this research possible.

The contributions of Devin Ostrom, Technical Officer with Robotics and Manufacturing Automation Lab (RMAL) at Ryerson University, is greatly appreciated. Devin offered his professional expertise and service in the design and construction of the robotic assistant and other electro-mechanical elements of this work.

This project would not have been possible without the contributions of many individuals. I appreciate the valuable advice of Dr. Borys Shchokin, with Ryerson University. The consultation of Drs. John McPhee, Amir Khajepour, Hamid Jahed, and Ehsan Toyserkani, with University of Waterloo, is also acknowledged.

This research is indebted in part to the contributions received from the industry. I particularly acknowledge the kind support of Mr. Jeff Stanley, with NDI Medical Research. NDI's contribution by lending Aurora®is also acknowledged. I express my gratitude toward Mr. Joseph B. Koblish, with Boston Scientific Corporation's EP Technologies, for providing the specifications of the SteeroCath-T catheter and generously contributing catheter samples. I also thank Mr. John Hauck, with St. Jude Medical's Atrial Fibrillation Division, for lending a silicone heart model.

This thesis is the culmination of a four-year endeavour, and many brilliant minds and kind hearts helped me through this journey. I would like to sincerely thank Hamidreza Bolandhemmat, Fariborz Rahimi, Mehrdad Hosseinizadeh, and Drs. Shahryar Rahnamayan, Nasser Lashkarian, Mohammad Shavezipur, and Daryoosh Saeedkia for the abundantly helpful discussions we had in the course of this project. I shall thank my friends Dr. Hamid Zarrabizadeh and Maziar Siar, in addition to Dr.

Ali Tehrani, Dr. Alireza Bayesteh, Mohaddesseh Azimlu, Dr. Saeed Behzadipour, Dr. Shahin Jafarabadi Ashtiani, and Alireza Bayat for their companionship and support in various ways.

I thank my family for their constant love and encouragement. In the end, I express my deepest gratitude beyond words to my wife, Hanieh Aghighi, who is the definition of beauty in so many dimensions, who blesses my life every day, and who bestowed on me the inspiration and confidence to thrive and achieve.

Dedication

To

my mother

for her unconditional love and her infinite faith.

Contents

List of Tables

List of Figures

List of Algorithms

Nomenclature

α	Angle subtending pull-wire arcs
ϵ_p	Task-space position error threshold
ϵ_q	Joint-space position error threshold
γ	The characteristic radius factor in pseudo-rigid model
κ_Θ	The stiffness coefficient of torsional spring
λ	Damping factor
ω_a	Actual orientation of the distal shaft tip
ω_s	Orientation reading from Aurora® sensor
ψ	Roll angle
Θ	Angle of deflection in pseudo-rigid model
θ	Deflection angle
θ_0	The steering dead-zone angle
θ_2	Twist angle in kinematic model
θ_3	Deflection angle in kinematic model
Θ_{knob}	The steering angle at which steering direction is reversed
θ_{knob}	Rotation angle of the steering knob
θ_{knob}^{bl}	Backlash angle in when steering direction is reversed
θ_{twist}	Handle twist angle
$\tilde{p}$	Positioning error

φ Yaw angle

ϑ Pitch angle

$\vec{a}$ Sensor calibration vector

$\vec{b}$ Sensor calibration vector

$\vec{v_1}$ Sensor calibration vector

$\vec{v_4}$ Sensor calibration vector

$\vec{v_6}$ Sensor calibration vector

${}^{S}\vec{a}$ Calibration vector in sensor coordinate frame

${}^{S}\vec{b}$ Calibration vector in sensor coordinate frame

${}^{S}\vec{v_1}$ Calibration vector in sensor coordinate frame

${}^{S}\vec{v_4}$ Calibration vector in sensor coordinate frame

${}^{S}\vec{v_6}$ Calibration vector in sensor coordinate frame

B_1 Intercept in linear translation actuation transfer

B_2 Intercept in linear twist actuation transfer

D Intracardiac disturbance

d The clearance of the pull-wire end from the centre-line of the catheter

$d\theta/ds$ Beam curvature

d_1 Translation parameter in kinematic model

d_4 Kinematic model parameter

d_7 End section of the kinematic model

d_{handle} Handle translation

E Young's modulus

EI Flexural rigidity of beam

F Pull wire tension force

I Moment of inertia

J_ω Orientation Jacobian

J_p Position Jacobian

K Spring constant

k_1 Slope in linear translation actuation transfer

k_2 Slope in linear twist actuation transfer

k_3 Backlash factor in steering knob

K_c Controller gain

K_J Joint-space controller gain

K_T Task-space controller gain

K_{handle} Handle actuation transfer gain

L Deflectable section or beam length

l_S Aurora® sensor coil length

M Moment load

O_0 Distal shaft virtual base

O_1 Deflectable section or model base

O_4 Deflection section end

O_6 Catheter tip

p_a Actual position of the catheter tip

p_d Desired position of the catheter tip

p_m Position of catheter tip as calculated from kinematic model

p_s Position reading from Aurora® sensor

p_{target} Target position for trajectory planner

q Model joint-space parameters vector

q_a Actual joint-space parameters

q_d Desired joint-space parameters

Q_i Orientation quaternion for sensor S_i

q_{handle} Desired actuation parameters at the handle

q_{ma} Actual joint parameters of robotic assistant

q_{md} Desired joint parameters of robotic assistant

R_1 Radius of outer pull-wire arc

R_2 Radius of inner pull-wire arc

r_c Distal shaft radius

R_F^A Falcon to Aurora® coordinate conversion matrix

r_S Aurora® sensor coil radius

r_{cam} Radius of steering knob cam

$R_{O_1}^A$ Mode base to Aurora® coordinate conversion matrix

$R_{S_i}^A$ Sensor S_i to Aurora® coordinate conversion matrix

S_1 Base sensor

S_2 Tip sensor

T_0^7 Homogeneous transformation matrix of the distal shaft kinematic model

t_1 Time instant

t_2 Time instant

w $\det(J_p)$

w_t Singularity threshold

${}^A\vec{y_S}$ Unit vector along the Y axis of base sensor (S_1) in Aurora® coordinate frame

${}^A\vec{z_S}$ Unit vector along the Z axis of base sensor (S_1) in Aurora® coordinate frame

${}^S\vec{y_S}$ Unit vector along the Y axis of base sensor (S_1) in sensor coordinate frame

${}^S\vec{z_S}$ Unit vector along the Z axis of base sensor (S_1) in sensor coordinate frame

Chapter 1

Introduction

1.1 Catheter and Catheterization

Steerable or active catheters are versatile devices mainly deployed in the fields of interventional cardiology and cardiac electrophysiology. The prevalent application domain of steerable catheters is in the treatment of cardiac arrhythmias. Arrhythmias, which are abnormalities of the heart rhythm, constitute one of the most common clinical problems in cardiology [1]. Cardiac catheterization is often required for the accurate diagnosis and management of complex arrhythmias. Catheterization is also the standard of treatment for symptomatic tachyarrhythmias and the preferred therapy in other patients unresponsive to or not suited for pharmacological treatment.

Catheters are typically introduced through femoral vein or artery into the body, and are positioned inside cardiac chambers to perform invasive electrophysiologic studies (EPS) and radio frequency (RF) ablation or cryo-ablation. Catheter-based procedures are normally conducted under fluoroscopic guidance which subjects the patient as well as the interventionalist to an intermittent yet continual and accumulative exposure to the ionizing radiation of fluoroscopy.

In catheter navigation, the interventionalist manipulates the handle or body of the catheter in order to bring the catheter's distal end into contact with the intracardiac anatomy or endocardium. The distal end houses the ablation cap and a number of electrodes used in EPS. The navigation of the catheter to the desired positions on the endocardium and maintaining the contact for the required duration is inherently difficult, due to the flexibility of the catheter and its distal shaft. In addition, cardiac contractions and patient's respiration complicate precise

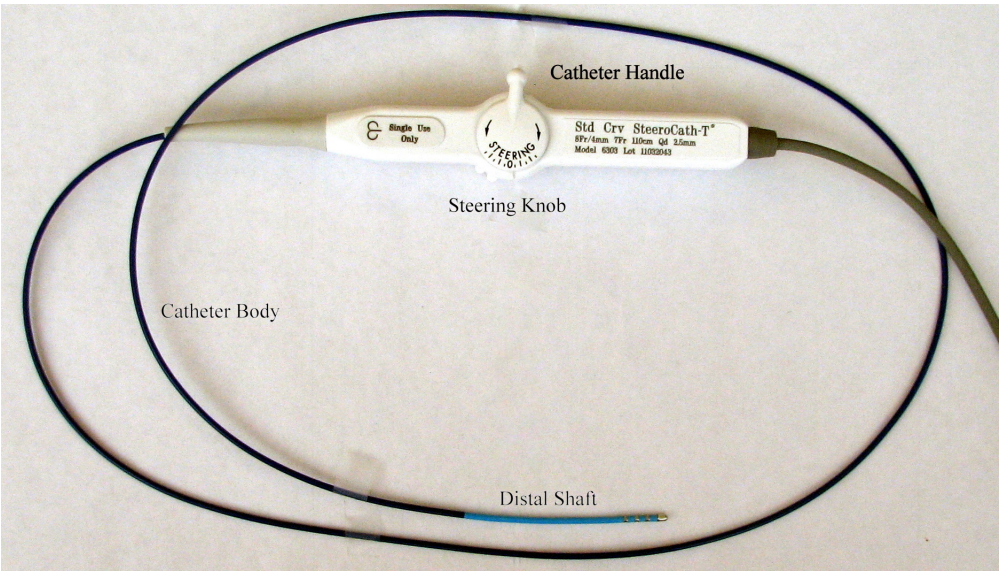

Figure 1.1: A sample steerable catheter. The catheter sections are marked in the picture.

manoeuvring of the distal tip. As a result, a stable contact between the tip and the endocardium at the intended positions is difficult to achieve and maintain. This means the interventionalist might need to make repetitive attempts in directing the catheter tip to reach arrhythmogenic zones before pacing or ablation can take place. To enhance catheter navigation, various methodologies have been utilized in biomedical device industry. There are also several methods proposed in academia to tackle navigation issues. In the section to follow, the literature in this field is reviewed.

1.2 Catheter Navigation Methods and Technologies

In this section, the existing technologies along with the published approaches in the field of catheter navigation are reviewed. In this context, three main areas of catheter tracking, catheter steering and catheter modeling are identified and surveyed in the subsequent sections.

The instantaneous position or shape configuration of the distal shaft of the catheter is required to be known in order for navigation to be realized. When the catheter is tracked and its position is known, the navigation system or the operator

of the system can decide how to manipulate the catheter to reach or maintain a target position. Section 1.2.1 presents the state of the art in tracking technologies.

To steer the catheter to target positions, an actuation mechanism is required to manipulate the catheter handle or body. Catheter manipulation is performed manually in everyday catheterizations, but a number of systems have been developed to leverage manual steering of the catheter, using different actuation methods. Section 1.2.2 reviews the published work in this area.

To achieve automatic navigation of catheter tip position, when the handle or proximal section of catheter is actuated, the properties of catheter deflection and the relationship between manipulations at the handle and the resultant displacements at the tip is required to be studied. Section 1.2.3 provides an overview of catheter modeling methodologies in the literature.

In summary, by utilizing a catheter model a strategy can be designed to control the position of the catheter. For closed-loop position control and navigation, a tracking system is needed to provide the catheter position feedback and a steering mechanism is required to manipulate the catheter. When the existing literature is reviewed, an approach will be identified and developed to realize catheter navigation, in the following chapters.

1.2.1 Catheter Tracking

Tracking and localization of a catheter's distal shaft inside cardiac chambers is an area of active research. Commercial solutions mostly try to visualize a static model of the heart chambers and illustrate instantaneous pose of the catheter relative to this model. In the following, commercially available systems that offer tracking of intracardiac catheters and some level of association of catheter position with respect to the endocardium are reviewed.

- **CARTO XP EP Navigation System** (Biosense Webster, Diamond Bar, CA) is a mapping and ablation navigation system. The navigation system consists of three coils fitted below the patient's bed, generating an ultra low electromagnetic field (5×10^{-6} to 5×10^{-5} Tesla) around the patient's chest. These three electromagnetic fields are temporally and spatially distinguishable by the location sensor mounted on the tip of the catheter. The sensor can measure the distance from each coil as a function of the electromagnetic power received. Given the three distance measurements, the 3D position of

the catheter is determined by triangulation. The accuracy in localization is below 1 mm [2]. In practice, two locatable 8F[1] catheters are guided by fluoroscopy to reach heart chambers. One is used as the reference catheter and the other is moved inside the endocardial space. The catheter constantly reads the bio-electric signal received. When the catheter is in contact with the endocardium as the recorded signal indicates, the location can be marked through the system's graphical interface as a point on the endocardium associated with its ECG (electrocardiogram) readings. After a cycle of marking, a map is constructed from the collection of marks in three dimensional space. This map reflects the electrical activities with a colour coding scheme [3]. After construction of this electroanatomical model, the catheter is illustrated with respect to the model and ablation can be planned and performed.

- **Localisa®** (Medtronic Inc., Minneapolis, MN) uses three orthogonal surface electrode pairs inducing 1 mA AC current at frequencies around 30 KHz through the thorax. To figure out the position of catheters inside the heart, the voltage drop along the heart is measured. Knowing the impedance of skin and lung, and reading the voltage at the catheter, the 3D position is calculated [4, 5]. The localization accuracy is reported to be better than 2 mm in vitro and in vivo. Points of interest can be tagged by the operator through the system's graphical user interface (GUI) but a model of cardiac chamber is not constructed.

- **EnSite NavX™** (St. Jude Medical, St. Paul, MN) uses three electrode patch pairs to generate an electrical field around the torso to locate catheters, similar to Localisa. Catheters can record intracardiac ECG for EPS. Using the catheter locations and by moving the catheter inside the cardiac chamber a 3D model of the chamber is generated which can serve as a guide in manoeuvring the catheter by the electrophysiologist. Similar to CARTO, generating an activation map on this 3D surface is a lengthy procedure which requires moving the catheter around the chamber and recording the ECG when touching the endocardium. To overcome this problem another version of the system, Ensite Array uses an array of electrodes to realize non-contact mapping.

  Ensite Array utilizes a catheter-mounted Multi Electrode Array (MEA), (a woven braid of 64 0.003-in-diameter wires) is mounted on a 7.6 ml balloon on a 9F catheter to create a non-contact unipolar electrode [6]. The raw far-field

[1] F stands for French, the unit of diameter for catheters. 3F equals 1.0 mm.

electrographic data from the MEA are acquired and fed into a multichannel recorder and amplifier system, sampled at 1.2 KHz, and filtered with a bandwidth of 0.1 to 300 Hz. The amplifier also has 16 channels for contact catheters and 12 for the surface ECG electrodes. A ring electrode located on the distal shaft of the MEA catheter in the descending aorta is used as a reference for both noncontact and contact unipolar electrogram recordings.
Any catheter position can be found with respect to the MEA by passing a 5.68 KHz, low-current locator signal between the catheter being located and ring electrodes distal and proximal to the MEA on the noncontact catheter. The MEA detects and determines the locator signal angles and thus localizes the source. The potential distribution on the MEA created by potentials at the blood-endocardial boundary is described by Boundary Element Model (BEM). The inverse computation estimates the action potentials on the endocardium from the electrode readings. Ensite can measure the received potential from 3360 predefined points and visualize the readings on virtual ventricular map (this map is a system parameter). The accuracy in catheter localization is 3.2 mm if the distance between the catheter and the MEA is less than 5 cm [7]. In [8] fundamentals of such an approach to cardiac mapping is reviewed and a similar system is developed.
It is worth noting that position measurement technique in Localisa and EnSite NavX is subject to impedance calculation errors especially during the ablation. As the temperature rises at the ablation site, the impedance rapidly changes and the catheter might be shown to move away from the site. The electrophysiologist cannot determine whether the catheter was actually moved or the change of impedance resulted in the illusion of losing the contact with the substrate.

- **RPM™** (Real-time Position Management™, Boston Scientific, Natick, MA) In this system, two reference catheters are placed in known positions in the heart. One catheter is placed in either the right atrial appendage or the coronary sinus, and one reference catheter is positioned in the right ventricular apex. The reference catheters are equipped with four ultrasound transducers and the ablation catheter contains three ultrasound transducers. An ultrasound transmitter and receiver device sends a continuous cycle of ultrasound pulses (at 558.5 KHz) to the transducers of the reference and ablation catheters. By assuming the speed of sound in blood to be 1550 m/sec, and using sonomicrometry[2] principles, the distance between individual transduc-

[2]Sonomicrometry is defined as range finding using ultrasound. Specifically, the term sonomi-

ers is calculated. The 3D positions of transducers are estimated from distance measurements [10].
Such 3D position calculations depend on the position of the reference catheters [11]. Since the spatial configuration of catheters relative to each other rather than their absolute position is calculated, the measurement accuracy depends on the accuracy of reference catheter placement. An accuracy of 2-8 mm in positioning has been reported.

All available commercial solutions localize catheter position and rely on 3D electroanatomical visualization for ablation navigation. Visualization of a static model is an attempt to compensate for the lack of a real-time imaging modality. The 3D model does not reflect the actual endocardial structure and is utilized as the only available method. In all the above systems, fluoroscopy is a required imaging modality, however, the radiation time is reduced compared to conventional navigation [12].

Electromagnetic tracking, electrical localization and ultrasonic position measurement are the major methods identified in catheter localization. Magnetocardiography (MCG) is an alternative approach used to localize any intracardiac current source, such as the origin of ventricular tachycardia or an amagnetic catheter [13]. The accuracy of such measurement calculations is very limited (above 5 mm)[14].

Another approach is to utilize imaging modalities in the localization or tracking of the catheter. For instance, magnetic resonance imaging (MRI) has been used to track and localize MR-compatible catheters [15]. However, such methods demand the availability of imaging system and the compatibility of the interventional devices, both of which are limiting factors in practice.

An ideal catheter localization/tracking system should provide real-time position measurements of the catheter with minimum reliance on extra support systems, such as medical imagers. If the tracking system can be used in-vitro, it can be more easily integrated into the development of a navigation system. Among the surveyed methods, electromagnetic tracking, similar to that of CARTO XP system,

---

crometry refers to the calculation of distances between ultrasonic transceivers by measuring the time of flight of a sonic wave-front from the transmitter to the receiver and scaling by the velocity of sound in tissue. In fact, in catheterization, this technique of positioning is called Sonomicrometry Catheter Localization (SCL). A computation method called MultiDimensional Scaling (MDS)[9] is used to find the 3-D location of sonomicrometry transducers based on their distances from each other. For n transducers, $n(n-1)/2$ distance measurements are required to compute their positions.

is identified as a candidate that meets such requirements. In fact, Aurora® electromagnetic tracking system (NDI, Waterloo, ON, Canada) is used in this research to realize catheter tracking.

1.2.2 Catheter Steering

In order to enable interventionalists to direct catheter and guide-wire to target positions efficiently, there are only two very new commercial systems under development:

Niobe® (Stereotaxis, St. Louis, MO) realizes magnetic navigation [16, 17] using a special magnetic catheter. In this system, two permanent magnets are placed on the sides of patient table and the catheter is navigated inside their magnetic field, as seen in figure 1.3. To deploy Niobe®, the catheterization lab must be magnetically compatible with the system. The cardiologist can control movement of catheter in the direction desired through the system's console. Fluoroscopy is the modality used for guidance; however, the physician manipulates the catheter from the control room and is not exposed to ionizing radiation. Niobe®offers the steering capabilities needed but with an added cost of a customized catheterization lab. The system has been successfully deployed for electrophysiological mapping and cardiac ablation operations [18, 19, 20]. However, application of a magnetic system is limited when patients have implantable cardioverter defibrillator (ICD) or pacemaker due to the presence of ferrous metals in the construction of such devices. A shortcoming of this system is the limited force exerted by catheter tip, hindering effective contact or navigation in some cases. Niobe®has also been utilized in conjunction with CARTO to track and visualize the steered catheter in the electroanatomical map of cardiac chambers resulting in a more effective navigation.

Sensei™ (Hansen Medical, Mountain View, CA) is a robotic system for assisted catheter navigation [21, 22]. The system takes advantage of two steerable sheaths (inner 10.5F and outer 14F) through which a passive EP catheter is deployed. The sheaths are operated by a robotic system. The catheter position can be controlled in three dimensions and a more stable manoeuvring compared to manual steering is achieved. In terms of visualization, the system relies on conventional fluoroscopy.

Figure 1.2: Niobe®system setup paired with Siemens AXIOM Artis dFC™Single-plane C-arm fluoroscopy machine in the centre. Reproduced with permission from Figure 1 in [17].

Figure 1.3: Sensei™system setup. Reproduced from Figure 5 in [23], with kind permission of Springer Science and Business Media.

Both systems realize the remote manipulation of the catheter, thus reducing the exposure to the radiation of fluoroscopy for the interventionalists. However, the cost of such systems could be a prohibitive factor in their utilization. In academia, there have been attempts to build steerable catheters utilizing micro-hydraulic actuators [24, 25, 26], and shape memory alloys [27, 28]. In such catheters, the actuators are collocated with and housed inside the deflectable shaft. These systems rely on specialized catheters or sheaths along with their actuation mechanisms to realize catheter steering.

To facilitate the manipulation and navigation of conventional catheters, without the bulk of support systems that entail operating room customizations and added costs, parallel to this work, Cercenelli, et al. [29] have mounted a typical catheter on a robotic system that enables motorized manipulation of the catheter and repetition of recorded manipulations. A robotic system that replaces the interventionalist's hand in catheter handle manipulation is a feasible way to achieve motorized steering. This idea is further enhanced through this research to achieve automatic and assisted catheter navigation.

1.2.3 Catheter Modeling

Catheter navigation requires a method to control the position of the catheter tip. To control the position, how the catheter deflects, rotates and moves in response to the actuations at the handle needs to be studied and modeled. This means a method is needed to model the kinematics, statics or dynamics of the catheter shape changes in response to the actuations at the handle. Based on the model developed for the catheter a control strategy can be devised. In this section, the published catheter models are reviewed.

In order to review catheter modeling methodologies, a distinction is needed to be made between passive catheters and active or steerable catheters. Steerable catheters embed a mechanism to deflect the distal shaft of the catheter using a knob on the handle. When deflected the catheter is shaped like an arc. Passive catheters do not offer any deflection control mechanism and could be preformed to suit specific applications. For navigation purposes, a steerable catheter is preferred as it provides for better control over catheter tip position.

Most of the literature on catheter modeling have targeted the simulation of the catheter when it lies inside tubular and vascular structures. Such simulations usually apply numerical modeling approaches. One general approach is to model

the catheter or a similar device such as guide wire and endoscope, as a multibody system composed of rigid links coupled with joints. Ikuta et. al [30] have modeled the endoscope as a series of links connected with visco-elastic joints each with two rotational degrees-of-freedom (DOF). They simplify the equations of motion of the endoscope eliminating most of the dynamics due to inertial and Coriolis terms. In their work, the configuration of the endoscope depends on the contact and reaction forces between the endoscope and the intestine that surrounds it. Similarly, Dawson et. al [31] have developed an interventional cardiology simulator in which the catheter is modeled as a multibody undergoing contact, contrast injection, and operator force exerted at the proximal end. In such methods, the catheter is passive and deforms in response to the forces at the proximal end and interaction forces with the known surrounding anatomy. A similar approach is to discretize the flexible instrument, and to find the optimum configuration of the discrete segments based on some criteria. For instance, Kukuk and Geiger [32] have found the most plausible configuration of the endoscope given the physical and mechanical constraints. It is noted that catheters are flexible devices and their movements is affected by their flexural rigidity and the spring energy due to bending, as contrasted to endoscopes that are composed of actual links. Konings et. al [33] have developed an iterative analytical algorithm for guide-wire simulation to minimize the total guide-wire bending and vessel wall deformation energy. Their interesting quasi-static method and the preceding dynamic models deal with passive devices with known constraints. To be applied to real operations, such methods need to be extended to steerable catheters in the absence of known contact forces.

Another method is to model the catheter as a continuum of flexible beams simulated by finite element modeling (FEM). In their virtual catheter prototyping system, Cai et. al [34] have constructed the catheter from arc segments that are modeled by finite elements. In another paper, Lawton et. al [35] have formalized the finite elements as Cosserat rods [36] and have found the catheter configuration by searching for the equilibria that minimize the bending energy. Nowinski and Chui [37] have constructed the catheter FEM model based on linear elasticity theory. Their model cannot represent large geometric non-linearities of the catheters. Cotin et. al [38] have reported an incremental FEM-based approach and Lenoir et. al [39] have developed a physics-based FEM model for catheter and guide-wire simulation. Wang et. al [40] have proposed a hybrid approach by constructing the catheter as a multibody of flexible beams. In their approach, a multibody dynamic analysis yields catheter displacements and a non-linear finite element analysis predicts the catheter deformations. An advantage of FEM models is the ability to

mimic the actual catheter's deflection. However, the computation time could be an issue for real-time modeling. Similar to multibody approach, FEM-based methods rely on known constraints to model bending and motion of passive devices.

Polynomial models such as splines have also been reported [41]. Such models provide an optimum shape of the flexible device. However, the simulations are not physics-based and are not capable of realistic modeling of elastic bending.

The existing models outlined above have focused mainly on passive catheters or active catheters with in-situ actuators. The problem of passive catheter modeling techniques is the requirement that the anatomy surrounding and constraining the catheter should be known a priori. The existing models search for the best fitting configuration of the catheter based on the given constraints. In real operation, such patient-specific data do not exist. In addition, when the catheter lies in intracardiac chambers, the anatomical constraints are different from the vascular structures and passive catheter models do not address intracardiac applications. The issue with the models for active catheters with in-situ actuators is that each model is only applicable to the specific actuation mechanism used in a prototype catheter. Therefore, the existing models cannot be adopted for commercially available steerable catheters.

To the best of the author's knowledge, no model has been developed for commercially available steerable catheters, which generally utilize pull-wires to realize actuation. Another issue is that all the methods solve the forward problem of finding catheter tip motion in response to manipulations at the handle. To control the catheter tip position, the inverse problem should be solved instead. Specifically, to achieve a desired motion or to reach a desired position, the appropriate handle manipulations should be found. As the catheter is an under-actuated flexible mechanism, the problem domain needs to be restricted, so that the catheter system becomes deterministic and a unique inverse solution could be found. As the forces acting on the catheter are not known, the modeling method needs to either estimate or eliminate them, to reach a solution. In the following chapter, a kinematic approach is proposed to eliminate external forces factors under certain conditions.

1.2.4 Summary

The existing systems and methodologies attempt to enhance catheterization procedures by providing more precise control over the catheter's distal shaft position, by tracking and visualizing the distal shaft and its surrounding anatomy, and re-

ducing the interventionalist's reliance on fluoroscopy for navigation. However, the systems do not realize automatic navigation and are very costly. In addition, the large size of double-sheath solution (14F) offered by Sensei™limits its deployment on all patients.

By harvesting the reviewed methodologies in catheter modeling, tracking and navigation, this thesis is an attempt to realize a novel methodology for enhanced catheter navigation. A kinematic approach will be developed to reach an approximate model of steerable catheters' distal shaft configuration based on the known actuations at the handle, without requiring the knowledge of the interacting forces between the catheter and its surrounding anatomy. A commercial steerable catheter deployed routinely in catheterization labs will be used in the navigation system in contrast to specially-designed catheters or sheaths. The catheter will be tracked using an electromagnetic tracking system with two sensors attached to its distal shaft. A robotic system will be utilized to replace the interventionalist's hand in manipulating the catheter handle. Finally, the navigation system will utilize the robotic system to navigate the tracked catheter automatically inside the heart.

1.3 Thesis Contributions

This thesis is an endeavour to develop and validate a prototype system to assist the interventionalist in performing catheter-based procedures and to facilitate the navigation of the catheter by planning and automating catheter manipulations using a commercial off-the-shelf steerable catheter. To realize such a system, multiple disciplines and technologies have been utilized and integrated. This research contributions are summarized as follows.

- Distal shaft modeling [42, 43, 44, 45]
  - A kinematic model for the distal shaft of steerable catheters, and the study of distal shaft workspace and singularities under the kinematic model
  - A static modeling methodology for the planar deflection of the catheter's distal shaft
- A complete platform for robot-assisted intracardiac catheter navigation, which includes the following novelties [42, 43, 44]
  - A method for catheter tip position control, based on the kinematic model

  - A strategy for semi-automated catheter navigation
  - Three navigation methodologies of motorized, assisted and automatic catheter manipulation.
  - A robotic mechanism for assisted catheter manipulation
  - CathNav: A software platform for robot-assisted catheter navigation

- Validation of modeling and navigation [42, 43]
  - In-vitro validation of kinematic modeling through the construction of a static phantom
  - In-vivo validation of kinematic modeling
  - In-vivo validation of automatic navigation through the developed platform

1.4 Thesis Structure

In this chapter, the literature in the areas pertinent to catheter navigation was reviewed. An overview of the state-of-the-art of the technologies and systems developed for the purpose of enhancing catheter navigation was provided. The published approaches to model catheters and similar devices were also surveyed. The contributions made through this research were also previewed. The rest of the thesis is structured as follows.

In chapter 2, the catheter navigation approach is introduced and the theoretical tools required to implement and realize catheter navigation are developed. In this chapter, the distal shaft of the catheter is modeled as a continuum manipulator composed of rigid components, and the manipulator kinematics are investigated. Using the model, the distal shaft workspace and its kinematic singularities are studied. The statics of distal shaft deflection is also reviewed and a method is proposed to validate the principles that govern the distal shaft deflection and provide the basis of the kinematic model. Based on the model, a strategy for catheter tip position control and finally catheter navigation is devised.

Chapter 3 describes the developed system design and implementation. It outlines the main system components, including robotic assistant, electromagnetic catheter tracking, software platform and 3D input device. The functionality of each subsystem and how the components are integrated are discussed in this chapter.

Chapter 4 presents the results of the experiments conducted to verify the validity of the kinematic model of the catheter's distal shaft. In this chapter, the experimental setups for the static and kinematic experiments are described, and the validity of modeling is demonstrated through statistical analysis of the results.

Chapter 5 presents the experiments conducted on swine to demonstrate the feasibility of successful navigation using the developed system. In this chapter, the system setup in the catheterization lab is illustrated and navigation experiments are explained. Finally, it is shown that the system can navigate the catheter inside the right atrium of beating heart of swine patients.

Chapter 6 discusses the merits and issues of the system, provides directions for future developments, and concludes the thesis.

Chapter 2

Catheter Position Navigation[1]

2.1 Introduction

This chapter provides the theoretical tools required to realize the navigation of a conventional steerable catheter. Through this chapter, the following are addressed:

- Forward kinematic problem - When the catheter is actuated at the handle, the catheter tip moves and the distal shaft deforms. The motion and deformation of the catheter are formulated as a function of actuations effective at the distal shaft. In section 2.2 the mechanical structure of the catheter is studied. Based on the structure of the catheter, the distal shaft of the catheter is modeled as a continuum robot and its kinematics is studied in section 2.3 . The statics of the shaft deflection is also analyzed and the model's workspace and singularities are characterized.
- Inverse kinematic problem - To utilize the kinematic model for the purpose of position control, an inverse kinematic control method is formulated in section 2.4.
- Navigation problem - In order to utilize the developed catheter model along with the inverse kinematic control methodology, a hierarchical navigation strategy is designed in section 2.5.

Through the course of this chapter, the navigation approach in this research is presented. The implementation and validation of the navigation methodology constitutes the subsequent chapters of this thesis.

[1]This chapter is partly published in [42, 44, 45, 43].

2.2 Steerable Catheter Anatomy

Commercial steerable or active catheters have a common standard structure. They are composed of three main sections, as illustrated in figure 2.1.

1. Handle - It is the part that is left outside the patient's body and is manipulated for navigation of the catheter tip. It houses a steering knob that allows the deflection of the catheter's distal shaft.

2. Body - The long body of the catheter is composed of a tube with internal metal-braiding for better transfer of torque to the distal section.

3. Distal shaft - It is the steerable section of the catheter that deflects in response to manipulation of the steering knob. It also houses ablation cap and ECG electrodes of the catheter. The distal shaft is usually more flexible and more elastic compared to the catheter body.

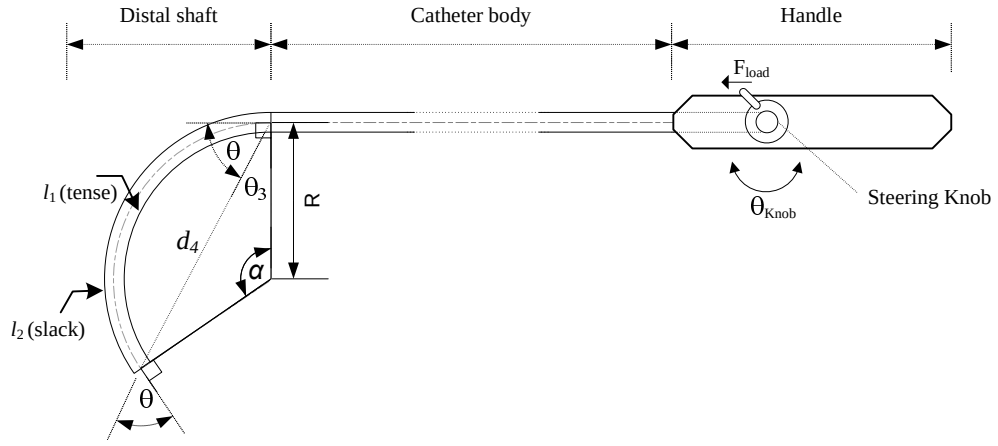

Figure 2.1: Catheter structure.

Although active catheters might differ from vendor to vendor in terms of their internal structures, the bending mechanism is essentially the same and is based on pull-wires and thin plates. If the catheter can bend in two directions, there are two pull-wires running in parallel inside the catheter body. A schematic of the bending mechanism of a typical bidirectional catheter is presented in figure 2.1. To select a catheter for this research, several steerable catheters, including RF-Conductr (Medtronic Inc., Minneapolis, MN), LiveWire (St. Jude Medical, St.

Figure 2.2: SteeroCath-T ablation catheter.

Paul, MN) and Ten-Ten (BostonScientific, Natick, MA) were dismantled and their internal mechanisms were examined, and SteeroCath-T ablation catheter (Boston Scientific, Natick, MA) was adopted for demonstrations and experiments (see figure 2.2).

The catheter handle is equipped with a steering knob that is directly attached to a cam inside the handle. There are two pull wires attached to the cam. The tension in the pull wires is changed by rotating the steering knob, and consequently, the cam. The wires run along the body of the catheter inside a flexible coil-like tubing and attach to two thin steel plates in the distal shaft. A metal ring encircles the plates. A wider steel plate is placed between the two thin plates and is fixed to the metal ring such that all the plates lie parallel with each other. This structure is housed in a flexible covering that does not allow the plates to bend independently. The wider plate extends to the catheter's distal end and is attached to the ablation tip. The two thin plates are soldered to the sides of the wide plate. With this construction, and due to the pretension of the plates, the distal shaft exhibits the elasticity of a spring, allowing no torsion along the length. The layering of the three plates provides an extra advantage seen in the laminated beams, which are more resistant to vibration and damp the vibrations exerted on them. Figure 2.3 provides a close-up of the internal structure of the distal shaft of SteeroCath-T. The dimensions and materials information acquired from the manufacturer are presented in table 2.1.

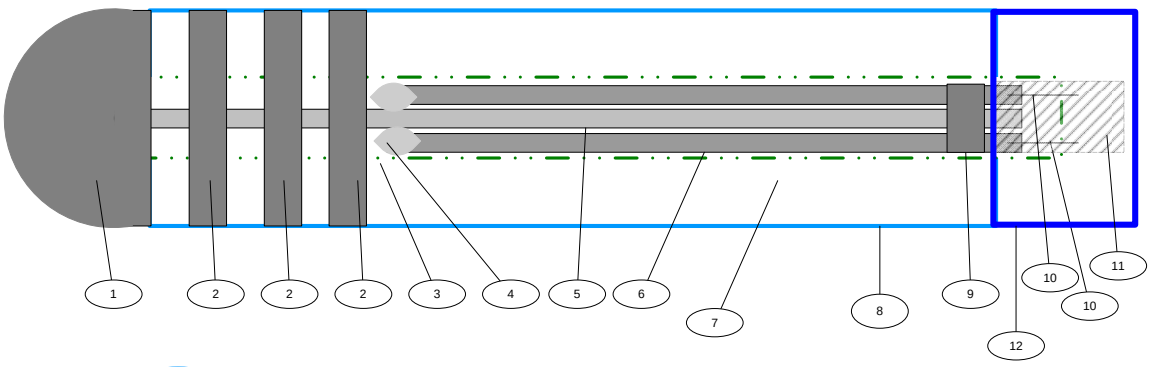

Figure 2.3: Anatomy of the distal shaft.

Table 2.1: Distal shaft components marked in figure 2.3. ID stands for inner diameter and OD denotes outer diameter.

#	Description
1	Ablation Tip, 90% Pt,10% Ir, 5 mm long, 0.092” diameter
2	ECG Electrode
3	Kevlar reinforced PFA Teflon, ID =0.036”, OD=0.048”, 0.012” thick
4	Soldering point
5	304 stainless steel, full hard, 0.2% yield strength 160 ksi, 0.035” wide, 0.005” thick, 4.0” long
6	304 stainless steel, full hard, 0.2% yield strength 160 ksi, 0.014” wide, 0.004” thick, 3.0” long
7	Empty space
8	35D PEBAX (distal shaft external cover) 0.012” thick, ID=0.068”
9	Attachment Ring
10	Pull-wire, 304 stainless steel, 0.011” diameter
11	Coil-like winding (over the pull wires) made of 0.009” diameter stainless steel wire
12	Main body cover, 72D PEBAX reinforced with braided wires on the inside

To bend the distal shaft, the steering knob/cam is turned, one wire is placed under tension, pulling the attached plate, while the other wire is released from tension. Since all the plates are attached at the tip, the tension acts as an axial force toward the plates at the tip. This force results in the buckling, followed by the bending of the plates in a plane orthogonal to the plates' surfaces. The bending is characterized by the tension of the inner plate resulting in compression and the extension of the outer plate whose attached pull wire is relaxed. When no force other than the wire tension acts on the distal shaft, it should bend in the plane perpendicular to the plates' surfaces. In addition to bending, twisting at the handle or the proximal section of the body results in the twisting of the distal shaft. Also insertion and retraction of the catheter body results in similar translations in the position of the catheter tip.

2.3 Distal Shaft Modeling

2.3.1 Introduction

The purpose of modeling is to find the formulations that predict the pose of the catheter tip in response to actuation displacements applied to the catheter handle. The formulations will be utilized to design and implement the control strategy that directs the catheter position when it is placed inside the cardiac chambers. Evidently, given the uncertainties in the instantaneous configuration of the catheter and its surrounding cardiovascular walls, the modeling cannot be accurate. On the other hand, due to the availability of position feedback, a controller will be able to achieve an acceptable tracking performance if an approximate and nonlinear model can be formulated. The steerable section of a steerable catheter is its distal shaft. To realize catheter navigation, the catheter tip or the distal-shaft end position must be controlled. The catheter body, from handle to distal shaft base, transfers the handle actuations to the distal shaft, and its effect on the shape of the distal shaft, and its end pose is limited, if the distal shaft base pose is known. With this premise, a model of the distal shaft is sought. More formally, the model will have to provide a mapping from actuation space to end pose of the distal shaft:

$$Model : (translation, twist, steering)_{handle} \mapsto (x, y, z, \psi, \vartheta, \varphi)_{distal} \tag{2.1}$$

where ψ, ϑ, φ are roll, pitch and yaw angles of the distal end respectively. In this model, unknown forces acting on the catheter are not included as inputs, but

the model could adapt its internal states to account for the effects of external forces on the distal-shaft end pose. The inverse problem would require a reverse map from the desired end pose to the handle actuation required to realize the desired pose. Apparently in this model, the catheter is an under-actuated system, and position and orientation of the distal-shaft end could exhibit coupling. In the kinematic model developed in the upcoming sections, this coupling is demonstrated and distal-shaft end position will be utilized to realize navigation.

We model the distal shaft as a continuum robot manipulator and taking advantage of control methodologies in the robotic literature, the catheter navigation could be achieved. Robinson and Davies [46] have defined a continuum robot as a robot with no distinct joints and rigid links. Instead, the robot bends along its length continuously, similar to an elephant's trunk and a squid's tentacle. By this definition, the distal shaft can be called a single-section continuum robot. Typically, the distal shaft sweeps a planar curve as it bends. Besides, the actuation mechanism of the catheter is placed at its handle that lies outside the patient's body during the operation. By the definition of Robinson and Davies [46], this means that the catheter is an extrinsic manipulator, as opposed to an intrinsic one that entails the collocation of the actuators with the structure that undergoes motion. The distal shaft of the catheter can be considered a single-section extrinsic planar continuum robot. By this definition, the distal shaft model is developed in the subsequent sections.

2.3.2 Kinematic Model

Based on the principle proposed by Hannan, Walker and Jones [47, 48], and as described in [44, 42], we model the distal shaft with rigid links and joints. The model is depicted in figure 2.4. The coordinate frames are assigned according to the Denavit-Hartenberg (D-H) convention [49].

It is assumed that the distal shaft bends with zero torsion, and with constant curvature, due to its mechanical structure and in the absence of deforming external forces. Zero torsion implies planar deflection, and the constant curvature means that the bending section always takes the shape of a circular arc. The two assumptions are validated through static modeling and experimentation later on. Based on the two assumptions, and with reference to figure 2.4, to reach from the base of the distal shaft (O_1) to the end of the bending section (O_4) in three-dimensional space, two rotations followed by one translation, and followed by two rotations are required. As a result, the catheter model will be composed of three sections:

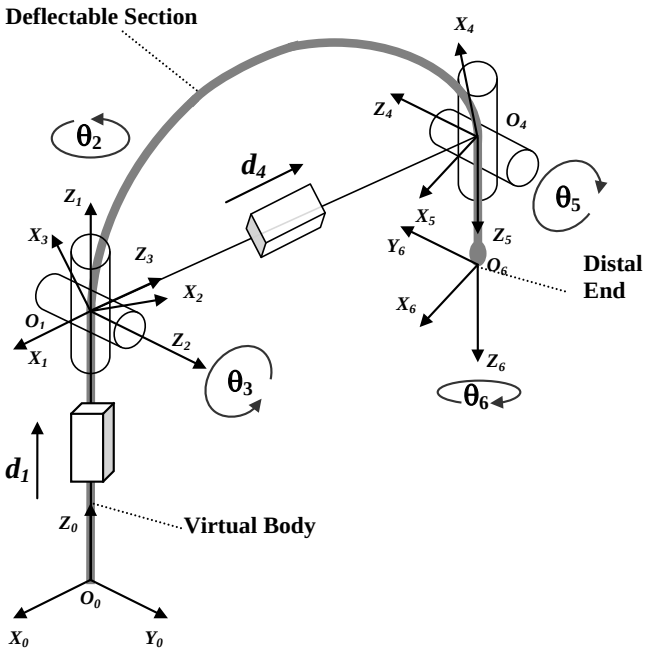

Figure 2.4: Distal shaft model and the assigned D-H coordinate frames.

1. O_0O_1 - This section constitutes the virtual base of the distal shaft. The translation of the distal shaft is represented by a prismatic joint. As the distal shaft is always aligned with the catheter body just below the distal shaft base (O_1), the prismatic joint can suitably model the differential motion of the distal shaft base, assuming the coordinate frames 0 and 1 are parallel. It is noted that as long as the displacement of the body (d_1) and not the actual position of the model base is of concern, the prismatic joint can represent the displacements.

2. O_1O_4 - The bending section of the distal shaft is represented by two revolute joints, one prismatic joint and two revolute joints. Consequently, the flexible bending section is modeled by rigid components.

3. O_4O_6 -This section represents the distal end of the catheter that is almost rigid. It houses a number of electrocardiogram (ECG) electrodes and the ablation cap. The ablation cap is considered the end-effector of the manipulator model. The length of this section is an intrinsic parameter of the catheter and is constant.

Based on the assigned D-H coordinate frames illustrated in figure 2.4, the D-H parameters can be summarized in table 2.2. The curvature constancy and the

Table 2.2: D-H Table. The distal end is unnumbered.

Link	a	α	d	θ	Joint variable
1	0	0	d_1	0	d_1
2	0	$\pi/2$	0	θ_2	θ_2
3	0	$\pi/2$	0	$\pi/2+\theta_3$	θ_3
4	0	$\pi/2$	d_4	0	d_4
5	0	$\pi/2$	0	$\pi+\theta_5$	θ_5
6	0	$\pi/2$	0	θ_6	θ_6
7	0	0	d_7	0	d_7

coupling between parameters yield $\theta_5 = \pi/2 - \theta_3$ and $\theta_6 = \pi - \theta_2$. The constant length of the distal end (O_4O_6) is denoted by d_7. The joint parameter θ_3 is better illustrated in figure 2.1.

Using table 2.2, the forward kinematics of the model is calculated. The homogeneous transformation matrix describing the position and orientation (pose) of the catheter tip with respect to the virtual base O_0 is found, as follows.

$$T_0^7 = \left[\begin{array}{ccc|c} c\theta_2{}^2 c2\theta_3 - s\theta_2{}^2 & c\theta_2 s2\theta_3 & -c\theta_3{}^2 s2\theta_2 & c\theta_2(d_4 c\theta_3 + d_7 s2\theta_3) \\ c\theta_3{}^2 s2\theta_2 & s\theta_2 s2\theta_3 & -s\theta_2{}^2 c2\theta_3 + c\theta_2{}^2 & s\theta_2(d_4 c\theta_3 + d_7 s2\theta_3) \\ c\theta_2 s2\theta_3 & -c2\theta_3 & -s\theta_2 c2\theta_3 & d_1 + d_4 s\theta_3 - d_7 c2\theta_3 \\ \hline 0 & 0 & 0 & 1 \end{array}\right] \quad (2.2)$$

The position vector obtained from equation 2.2 provides the basis for all the kinematic calculations. Before studying the characteristics of the catheter model in terms of the resultant workspace and its singularities, a static model of the distal shaft deflection is also formulated in the subsequent section. The static model will be utilized to verify the fundamental assumptions of constant curvature and zero torsion.

2.3.3 Static Model

The kinematic modeling presented in section 2.3.2 is based on the assumptions that the deflection occurs with constant curvature and zero torsion. In this section, to demonstrate that the assumptions are valid and based on the mechanics of the distal shaft, a static model of shaft deflection is developed.

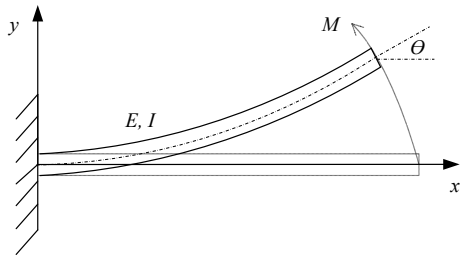

Figure 2.5: The effect of bending moment on a beam.

In case of the catheter plates, the tension in one wire causes exertion of a load at the soldering point (see figure 2.3). This load or force is always parallel to the surface of the plates and acts as a bending moment. The distal shaft is a beam cantilevered at the ring where all the plates end. This point is fixed as the catheter is deflected. As a result the distal shaft can be modeled as a cantilever beam with a load at the free end. The effect of weight of the plates and the covering materials are assumed to be negligible compared to the bending forces. The effect of bending moments on a beam is expressed by Bernoulli-Euler equation,

$$M = EI\frac{d\theta}{ds} \tag{2.3}$$

where M is the moment, θ angular deflection along the beam, s length of the beam curve, E Young's modulus of the material, and I the beam moment of inertia, , as illustrated in figure 2.5. The Bernoulli-Euler equation states that the bending moment is proportional to the beam curvature ($d\theta/ds$). For planar deflections, as in the catheter case, the curvature can be written as

$$\frac{d\theta}{ds} = \frac{d^2y/dx^2}{[1+(dy/dx)^2]^{3/2}} \tag{2.4}$$

where x is the coordinate along the undeflected beam axis and y is the transverse deflection. As a result, we have

$$M = EI\frac{d^2y/dx^2}{[1+(dy/dx)^2]^{3/2}}. \tag{2.5}$$

Equation (2.5) governs almost all planar elastic deflections. Dynamics and statics of deflections can be studied using this equation. Solving the equation for a closed form solution is not readily possible. When the deflections are small, the squared slope of the curve dy/dx can be assumed negligible. In this case the classical moment-curvature relationship is obtained,

$$M \cong EI\frac{d^2y}{dx^2}. \tag{2.6}$$

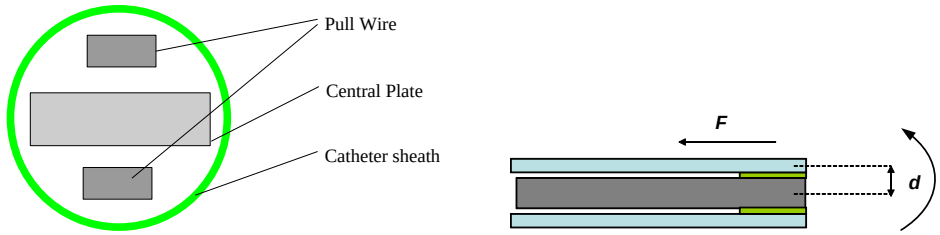

(a) (b)

Figure 2.6: (a) The cross-section of the distal shaft of a bidirectional catheter. (b) The end moment load created by the pull wire tension force F at the distance d from the centre line.

Small deflection assumes that $C = \frac{1}{[1+(dy/dx)^2]^{3/2}} \cong 1$. This assumption is valid for small deflection angles (e.g., $\theta < 10$ deg.) In our case, θ can go above 90 degrees. Consequently, catheter deflections cannot be approximated by small deflections model and large deflection analysis is required. When the beam curvature is constant and the bending is planar, (2.3) is readily used to calculate the coordinates of the free end of the beam with reference to its cantilevered end at equilibrium. As depicted in figure 2.6, M can be found by

$$M = Fd, \tag{2.7}$$

where F is the pull wire tension force, and d denotes the clearance of the pull-wire end from the centre-line of the catheter. If the flexural rigidity of the catheter, EI, is known, and no external load is applied to the catheter, the bending becomes a statically determinate problem and can be solved numerically using the chain algorithm, as described in [50]. However, the distal section is not a totally rigid mechanism, and as it deflects, its mechanical structure deforms. As a result, unless the exact configuration of the bent distal shaft structure is known, the flexural rigidity cannot be analytically calculated.

To find the flexural rigidity experimentally, a model is required that can accurately describe the deflection of a flexible structure like the catheter. On the other hand, the model should provide a closed-form formulation for the flexural rigidity. A pseudo-rigid body model [51] is such a model. In this model, the flexible beam is approximated with two rigid links pivoted together with a dimensionless torsional spring that emulates the beam's resistance to deflection. The pivot is placed at the distance γL from the free end, where γ is called the characteristic radius factor and $0 < \gamma < 1$. Figure 2.7 depicts the pseudo-rigid model. For end-moment loading,

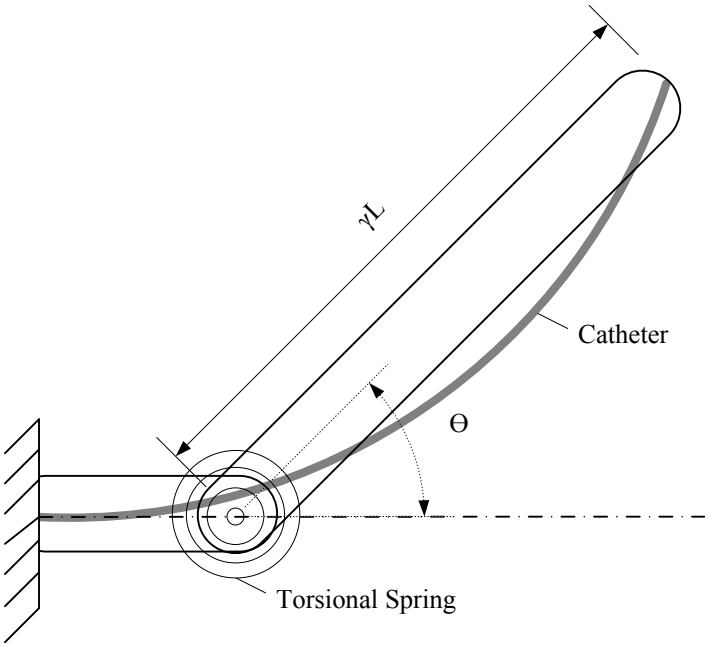

Figure 2.7: The bending section of the catheter and its cantilevered pseudo-rigid model.

the tip deflection follows (2.8),

$$M = K\Theta, \tag{2.8}$$

where M is the end moment load, K is the spring constant, and Θ is the angle of deflection. The spring constant is obtained by the following formula,

$$K = \gamma\kappa_\Theta \frac{EI}{L}, \tag{2.9}$$

where κ_Θ represents the stiffness coefficient of the torsional spring, and EI is the flexural rigidity of the beam. In end-moment loading, $\gamma = 0.7346$ and $\kappa_\Theta = 2.0643$, for deflection angles $\Theta \leq 124.4°$ [51]. By substituting (2.9) and (2.8) into (2.7), the flexural rigidity is obtained,

$$EI = \frac{FdL}{\gamma\kappa_\Theta\Theta}. \tag{2.10}$$

Using (2.10) and (2.3), the two-dimensional coordinates of the catheter end tip in response to a known force applied at the steering knob can be found. To summarize, the following procedure is utilized to find the presumed constant curvature:

The static model end position in the bending plane can be calculated using the chain algorithm [50] with the curvature value obtained through the above procedure. The chain algorithm essentially finds the end position by integrating the

Algorithm 2.1 Experimental curvature calculation

1: Fixate the catheter such that the assumed bending plane perpendicular to catheter's central plate is known.
2: Apply a known static force (F_{load} in figure 2.1) to the steering knob, such that the distal shaft bends and reaches an equilibrium shape.
3: Calculate the pull wire tension (F in figure 2.6) from F_{load}, i.e., $F \cong F_{load} \cos\theta_{knob}$.
4: Based on the actual position of the deflectable section end (x, y), find pseudo-rigid angle of deflection $\Theta = \arcsin y/(x - (1-\gamma)L$.
5: Calculate flexural rigidity EI using (2.10).
6: Calculate end moment M using (2.7).
7: Calculate curvature $(d\theta/ds)$ at the deflectable section end, using (2.3).

curvature over a discretized length of the beam or the distal shaft in this case. If the end position of the model and the actual position of the deflectable section end correspond, the validity of zero torsion and constant curvature assumptions are demonstrated. This methodology will be utilized in validation experiments described in chapter 4. The only limitation in this methodology is that pseudo-rigid model parameters κ_Θ and γ are valid for deflections less than 124.4°. The static modeling is intended to show that the kinematic model assumptions are based on the physics of distal shaft bending and the kinematic experiments will rigorously investigate the validity of the model. As a results, the aforementioned limitation in static modeling is justified. In the static experiments, the deflection angle will not exceed this limit.

2.3.4 Model Workspace

Based on the developed kinematic model, the workspace of the distal shaft can be studied. In order to construct the reachable workspace of the catheter using the forward kinematics transformation (2.2), it is intuitive to start with one degree of freedom (DOF) and then add the remaining DOFs one by one. Beginning with the deflection, represented by θ_3 in the model, figure 2.8(a) depicts the position of the catheter tip as the catheter bends in its plane of deflection, assuming the distal shaft base (O_1 in figure 2.4) is at the origin or $(Y, Z) = (0, 0)$. Apparently, when the catheter is in straight configuration, the angle θ_3 takes the value of $\pi/2$. As the catheter bends in one direction, θ_3 decreases till the bending segment end touches the virtual base at the value of $-\pi/2$. If the catheter is bidirectional and

it bends symmetrically, the mirror image of the profile with respect to the Z axis will correspond to bending in the reverse direction.

By adding the twist angle (θ_2) to the DOFs, the three-dimensional surface in figure 2.8(b) is generated for $\frac{-\pi}{2} \leq \theta_3 \leq \frac{\pi}{2}$ and $0 \leq \theta_2 \leq 2\pi$. The cross-section of this surface is the envelope in figure 2.8(a). It is noted that symmetrical bidirectional catheters are redundant, and any point p_i on the workspace in figure 2.8(b) is reachable by two configurations of (θ_2^i, θ_3^i) and $(\theta_2^i + \pi, -\theta_3)$.

Adding the last DOF, or the displacement d_1, completes the reachable workspace by shifting the 3D surface in figure 2.8(b) up or down in the Z direction, into the 3D volume that the catheter can reach. In practice, the catheter body does not remain straight for large displacements and the shift is only valid for differential translations of the body.

2.3.5 Differential Kinematics

In (2.2), parameters d_1 and θ_2 are directly actuated from the proximal end or handle. Catheter insertion and retraction change d_1, and catheter twist results in the variations of θ_2. How the catheter insertion/retraction/twist at the handle is translated into the changes in d_1 and θ_2 is not predictable unless the configuration of the entire body of the catheter and its contact zones with the surrounding luminal structures, the friction at contact zones, and the flexural rigidity of both the catheter body and the surrounding tissues are known. Due to the existence of the preceding unknown parameters in real operation, to control the position of the catheter, it is essential to identify the relationship between the actuation at the handle and d_1 and θ_2 at the distal shaft on the fly.

The parameters θ_3 and d_4 are coupled and together characterize the deflection of the distal section. As shown in figure 2.1, the curvature constancy of deflection results in the distal shaft to form a circular arc. The two pull-wires form two parallel arcs. The arcs subtend the angle $\alpha = \pi - 2\theta_3$. The catheter is axially inextensible and incompressible, which means the centre line of the catheter that represents the catheter in the model also forms the arc. As a result, the effective length of the arc is constant, i.e., $L = R\alpha$. This arc subtends the chord $d_4 = 2R\cos\theta_3$. After substitution, the relationship between d_4 and θ_3 is obtained,

$$d_4 = \frac{L}{\frac{\pi}{2} - \theta_3} \cos\theta_3. \tag{2.11}$$

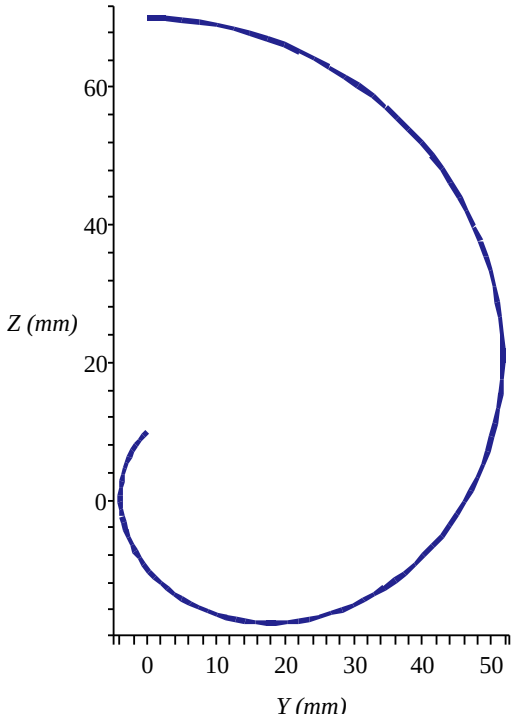

(a)

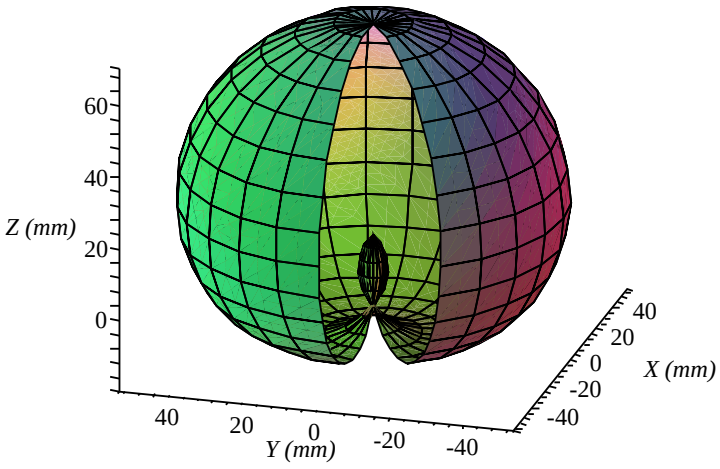

(b)

Figure 2.8: Catheter workspace for deflectable section length (L) of 60 mm and the distal end length (d_7) of 10 mm. The base of the distal shaft is at the origin. (a) The position profile of the catheter tip as θ_3 spans $-\pi/2$ to $\pi/2$. (b) The reachable workspace of the catheter tip as θ_3 spans $-\pi/2$ to $\pi/2$, θ_2 spans $-\pi$ to π, and $d_1 = 0$.

Using (2.11), the number of variables in position vector obtained from (2.2) reduces to three. This is a desirable result since it allows the construction of a square 3×3 position Jacobian, required for workspace analysis and for position control algorithms. The analytical position Jacobian is presented in (2.12) where s and c stand for sin and cos respectively.

$$J_p(\theta_2,\theta_3)=\begin{bmatrix} 0 & -s\theta_2(\frac{Lc\theta_3^2}{\frac{\pi}{2}-\theta_3}+d_7s(2\theta_3)) & c\theta_2(L(\frac{-s(2\theta_3)}{\frac{\pi}{2}-\theta_3}+\frac{c\theta_3^2}{(\frac{\pi}{2}-\theta_3)^2})+2d_7c(2\theta_3)) \\ 0 & c\theta_2(\frac{Lc\theta_3^2}{\frac{\pi}{2}-\theta_3}+d_7s(2\theta_3)) & s\theta_2(L(\frac{-s(2\theta_3)}{\frac{\pi}{2}-\theta_3}+\frac{c\theta_3^2}{(\frac{\pi}{2}-\theta_3)^2})+2d_7c(2\theta_3)) \\ 1 & 0 & \frac{L}{2}(\frac{2c(2\theta_3)}{\frac{\pi}{2}-\theta_3}+\frac{s(2\theta_3)}{(\frac{\pi}{2}-\theta_3)^2})+2d_7s(2\theta_3) \end{bmatrix} \tag{2.12}$$

To obtain the orientation Jacobian, the geometric Jacobian is constructed yielding a 6×6 matrix. After simplification of coupled joint parameters, the orientation Jacobian is found as presented in (2.13). Clearly, the orientation depends only on two parameters of θ_2 and θ_3.

$$J_\omega(\theta_2,\theta_3)=\begin{bmatrix} 0 & -\cos\theta_2\sin(2\theta_3) & 2\sin\theta_2 \\ 0 & -\sin\theta_2\sin(2\theta_3) & -2\cos\theta_2 \\ 0 & 1+\cos(2\theta_3) & 0 \end{bmatrix} \tag{2.13}$$

The Jacobian matrices obtained above will be used in the analysis of model singularities and in inverse kinematic control of the catheter position in the subsequent sections.

2.3.6 Model Singularities

The catheter is modeled as a serial manipulator. In order to control the tip position of the catheter, the singularities in the workspace are required to be analyzed as well. At singular configurations, the mobility of the manipulator end-effector - or the catheter tip in the model - locally decreases. In other words, in a subspace of the manipulator joint variables, i.e., the null-space of its Jacobian, the changes in the joint variables will not affect the end-effector pose.

Aside from the workspace boundaries that are singular by definition, at singular configurations inside the reachable workspace, the Jacobian becomes rank-deficient, subject to variable constraints $\frac{-\pi}{2}\leq\theta_3\leq\frac{\pi}{2}$ and $0\leq\theta_2\leq 2\pi$. The position Jacobian J_p is a 3×3 square matrix, so there is no row-rank deficiency and the determinant of the Jacobian can be set to zero to find the singularities. Interestingly, the

determinant will only depend on θ_3, yielding two equations to be solved together, as follows.

$$\frac{L\cos\theta_3^2}{\frac{\pi}{2}-\theta_3} + d_7\sin(2\theta_3) = 0 \tag{2.14}$$

$$L(\frac{-\sin(2\theta_3)}{\frac{\pi}{2}-\theta_3} + \frac{\cos\theta_3^2}{(\frac{\pi}{2}-\theta_3)^2}) + 2d_7\cos(2\theta_3) = 0 \tag{2.15}$$

Solving (2.14) and (2.15) yields two roots of $\theta_3 = \pm\pi/2$, independent of d_7 and L. As mentioned earlier, when $\theta_3 = \pi/2$ the catheter is straight and any change in θ_2 does not affect the tip position. The same is true at $\theta_3 = -\pi/2$ when the bending segment end O_4 coincides with the virtual base O_1. Consequently both roots are intuitively justified. It is noted that the singularities in the distal shaft configuration hold even if the modeling loses its fidelity.

The orientation Jacobian J_ω (2.13) is singular as it is always rank-deficient, because a column in J_ω is zero. This means that the angular velocity vector at the tip cannot be controlled arbitrarily by joint velocities. This important result reveals the intrinsic mechanical property that catheter orientation is not controllable in general, unless an external force deforms the catheter body to reach the same position but at a different orientation. On the other hand, to reach a desired orientation, the catheter cannot be positioned as desired. The shaft has three independent degrees of freedom for actuation, which is sufficient for positioning the catheter tip but insufficient for orienting the tip arbitrarily. In other words, for each position in the catheter's workspace, there is only one orientation that is associated with the position. In fact, the hemispherical symmetry of the ablation tip compensates for the lack of orientation control in the catheter. When the catheter tip is at a desired position, the catheter can function regardless of the tip's orientation. The results are summarized formally as follows.

Corollary 1 (Position Singularities)**.** *The singular configurations of the catheter tip's reachable workspace are at $\theta_3 = \pm\frac{\pi}{2}$. At these configurations, the twist angle (θ_2) does not affect catheter tip position.*

Corollary 2 (Orientation Singularities)**.** *The orientable workspace of the catheter tip is null, i.e., the orientation of the catheter tip cannot be configured arbitrarily for a given position.*

2.4 Catheter Position Control

2.4.1 Inverse Kinematic Control

The objective of the system is to control the catheter's tip position. The catheter's virtual joint parameters ($q = [d_1 \quad \theta_2 \quad \theta_3]^T$) are actuated at the handle. However, the catheter is not composed of rigid links and direct measurement of virtual joint parameters is not possible. To control the catheter tip position in lieu of uncertain joint parameters, operation/task space control is the practical choice, as opposed to joint space control [49]. In other words, the function of the controller is to take the tip from its current position to a desired position, rather than changing joint parameters in such a way that the desired position is achieved.

The positioning error $\tilde{p}$ is

$$\tilde{p} = p_d - p_a, \quad p_d, p_a \in \mathbb{R}^3. \tag{2.16}$$

where p_a is the actual position of the catheter tip, and p_d is the desired position. The controller's objective is to position the catheter such that $\tilde{p} \to 0$ in a finite time.

The catheter is modeled as a continuum manipulator. The model is basically a multibody of rigid links and joints. To control the movement of rigid multibodies, inverse kinematics is the available method. Jacobian transpose [52] and Jacobian (pseudo) inverse [53] are the stable and common methods in inverse kinematics control. Due to low convergence speed and sensitivity to noise, Jacobian transpose method is not a suitable choice for real-time control of catheter position in the intracardiac setting. Given that the kinematic model is non-redundant and the distal shaft position Jacobian (2.12) is a square matrix, the Jacobian inverse provides a solution for differential or resolved motion rate control [53]. Assuming $\delta p \equiv \tilde{p}$, the estimated joint-space error vector δq is found,

$$\delta q = J_p^{-1}(q)\delta p. \tag{2.17}$$

Figure 2.9 illustrates the control diagram for navigation using the task-space Jacobian inverse method.

2.4.2 Damped Least Square Method

Jacobian inverse methods tend to produce very large joint velocities/displacements in the neighbourhood of singular configurations. To resolve the Jacobian inverse

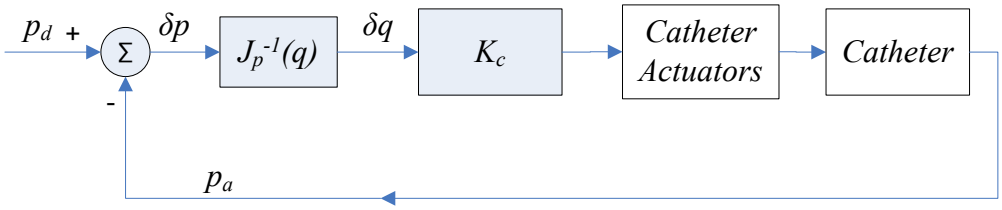

Figure 2.9: Jacobian inverse position control diagram.

instability issue near singularities, a damped-least-square (DLS) method [54] is utilized to obtain feasible joint motions at the cost of slower convergence. Using this method, equation (2.17) changes to

$$[\delta d_1 \ \delta\theta_2 \ \delta\theta_3]^T = J_p^T(J_p J_p^T + \lambda I)^{-1}[\delta x \ \delta y \ \delta z]^T, \tag{2.18}$$

where λ is the damping factor [55] computed by

$$\lambda = \begin{cases} \lambda_0(1 - \frac{w}{w_t})^2 & w < w_t \\ 0 & w \geq w_t \end{cases}, \tag{2.19}$$

where $w = \det(J_p)$ and w_t is the threshold below which the catheter is assumed to be near singular configurations. Using (2.19) the position of the catheter tip can be controlled from the base of the distal shaft. The DLS method is the same Jacobian inverse when damping factor $\lambda = 0$, with proven stability and robustness near singularities [55]. If the transfer of manipulations at the handle to the distal shaft is formulated, catheter navigation can be achieved.

2.4.3 Handle Actuation

In the forward kinematics, five parameters: d_1, θ_2, θ_3, d_4, and d_7 are present. The displacement due to the pushing and pulling (d_1) and the twist angle (θ_2) are directly actuatable. Also, the deflection angle (θ_3) is actuated by the knob on the catheter handle. The ablative section has a constant length d_7 for any catheter type. To formulate how actuations at the handle are transferred to the distal shaft, the specific mechanism of the SteeroCath-T catheter is considered, as depicted in figure 2.10.

By considering the mechanical structure of the catheter, the deflection angle is formulated as a function of the steering knob rotation. In the absence of external

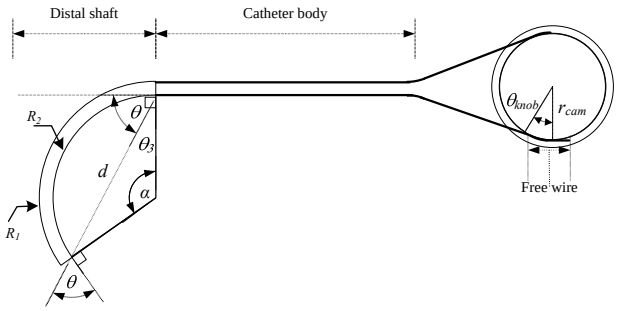

Figure 2.10: Deflection mechanism of SteeroCath-T catheter.

loads and when the wires do not stretch under tension. deflection is only a function of steering knob angle such that

$$\theta_3 = f(\theta_{knob}), \tag{2.20}$$

where θ_{knob} represents the rotation angle of the knob. When the knob is turned and the distal shaft bends, the plates in the shaft deflect to form two parallel arcs. The geometry of the arcs shown in figure 2.1 yields the relationship between the knob angle and the deflection angle which is expressed as

$$\Delta l = (R_1 - R_2)\alpha = r_{cam}(1 + k_3)\theta_{knob}, \tag{2.21}$$

where α is the angle subtending the arcs, $0 \leq k_3 \leq 1$ is the backlash factor to account for the tension-free wire displacement, and R_1 and R_2 are radii of the two arcs. In an ideal case, when both pull wires are tensioned, $k_3 = 1$. In practice, the value of k_3 needs to be identified by least squares fitting. From figure 2.1,

$$\theta = \frac{\alpha}{2} = \frac{\pi}{2} - \theta_3. \tag{2.22}$$

Replacing α from (2.21) in (2.22) results in the following linear relationship between the input knob rotation and the output catheter deflection:

$$\theta = \frac{r_{cam}(1 + k_3)}{2(R_1 - R_2)}\theta_{knob} + \theta_0 \tag{2.23}$$

where θ_0 denotes the steering dead-zone angle at near-zero deflection. However, when the direction of knob rotation is changed, the wire that is slack undergoes tension. The short length of the free wire in figure 2.1 must be traversed by the cam before any tension can be exerted. As a result, the backlash phenomenon is

intrinsic in the bending mechanism. In other words, the knob needs to be rotated by the angle

$$\theta_{knob}^{bl} = r_{cam}(1 - k_3)\Theta_{knob}, \tag{2.24}$$

before reverse bending can occur and Θ_{knob} is the angle at which the direction of the rotation is reversed at the knob. Equations (2.23) and (2.24) indicate that the deflection angle is a hysteretic function of the knob rotation. This is examined and validated by the experiments outlined in section 4.2.

Similar to the knob rotation angle, the handle twist is also estimated to follow a linear relationship with the distal shaft rotation angle. The catheter body is reinforced by braided steel wires in the cover and a spring-like steel tubing through which the pull wires are threaded. It is intuitively expected that the construction of the catheter body is relatively resistant to torsion and, the transfer of the twist angle at handle to the shaft is estimated to be linear as follows:

$$\theta_2 = k_2\theta_{twist} + B_2, \tag{2.25}$$

where k_2 and B_2 are the scalar parameters whose values depend on the friction in the vascular path through which the catheter is threaded. k_2 is a measure of rigidity of the catheter body and its surrounding tubular structures, and B_2 represents the backlash that is expected when the direction is changed. The same relationship can hold in the transfer of translation at the handle to the distal shaft, i.e.,

$$d_1 = k_1 d_{handle} + B_1. \tag{2.26}$$

The time-varying parameters in (2.25) and (2.26) shall be identified in actual operation by the controller. In practice, the relationships between the handle actuations and the resultant distal shaft parameters are not necessarily linear. Nonetheless, the above formulas can be linearization of possibly higher order relationships, that are identified and updated on the fly. This is in line with our Jacobian-based control approach that linearizes non-linear geometry of the kinematic model at any given point.

2.5 Navigation Architecture

Based on the methods developed for catheter modeling and inverse kinematic control, and after identification of how actuation is transferred from the handle to the distal shaft, a strategy to realize catheter navigation can be devised. As position

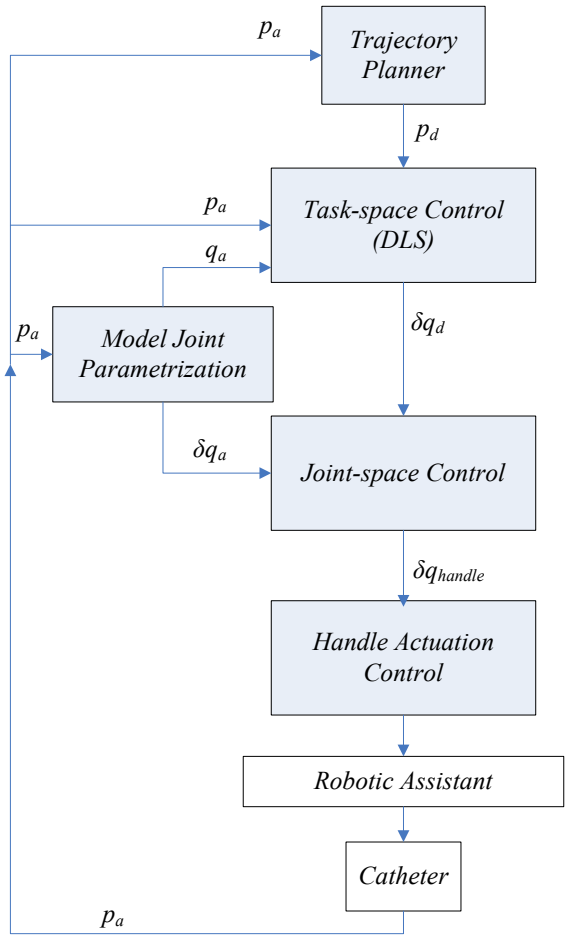

Figure 2.11: Hierarchical navigation architecture.

of the tip of the catheter, the distal shaft joint parameters and the handle actuation are all components of the navigation system, a hierarchical multi-level control architecture is required. The navigation architecture is outlined in figure 2.11.

The components of the navigation architecture and their designated functionalities follow.

- Trajectory Planner - To reach any target position automatically, a trajectory needs to be planned to take the tip from its instantaneous position to the target position. This trajectory could be a straight line to the target or a more customized curve that avoids any anatomical structures on the way. If not avoided, such anatomical structures will be obstacles that could hinder the navigation to the target. The trajectory planner provides the desired position vector $p_d = [x \quad y \quad z]$ to Task-space Control.

- Task-space Control - Position control of the catheter tip is realized through inverse kinematics using DLS method. Based on the desired (p_d) and actual (p_a) position vectors, the desired joint-space parameters δq_d are found by this component. Jacobian calculations require model joint parameters ($q_a = [d_1 \;\; \theta_2 \;\; \theta_3]$) that are provided by Model Joint Parameterization component. Task-space control can be used for "assisted" navigation of the catheter toward target positions.

- Model Joint Parameterization - The virtual joints parameters of the distal shaft model ($q = [d_1 \;\; \theta_2 \;\; \theta_3]$) cannot be directly measured. The joint parameters are identified from pose measurements of the distal shaft and are fed to the Joint-space Control and Task-space Control modules. The precision of this parameterization in matching the reality of catheter shape is a critical factor in a successful navigation. This component is further explained in the subsequent chapter.

- Joint-space Control - This component is responsible for tracking the desired joint-space parameters given the estimated virtual joint variables. Based on the tracking error ($e = \delta q_d - \delta q_a$), and using the handle actuation model developed in section 2.4.3, the required actuations at the handle are calculated and provided to the Handle Actuation Control.

- Handle Actuation Control - This component controls the robotic actuation mechanism that performs catheter handle manipulations. It interfaces with the physical robot and its driver/motor control systems. Control at handle actuation level can be used for "motorized" navigation of the catheter.

- Robotic Assistant - It is the mechanical system that replaces the interventionalist's hand and performs catheter manipulation as commanded by the Handle Actuation Control.

With the presented scheme, the navigation can be realized utilizing only the position feedback of the distal shaft of the catheter. In this scheme, no extra sensory data is required to realize position control. The Trajectory Planner might rely on external sensory and input devices to acquire the target position for navigation. The architecture described in this section, provides the foundation on which the navigation system is implemented. This hierarchical structure provides the flexibility to implement navigation in automatic, assisted, and motorized modes. Navigation modes are described in the next chapter.

2.6 Conclusion

In this chapter, the catheter's distal shaft structure was studied. Based on the mechanism of catheter's deflection, a rigid model characterizing the motion of distal shaft was developed, and its reachable workspace was studied. The singularities of catheter model were also analyzed. It was concluded that with this model, due to the limited number of DOFs, the catheter's orientation and position cannot be controlled simultaneously. As the position of the catheter is the subject of navigation, this limitation does not pose a problem.

The rigid model is based on the assumption that catheter deflection is governed by two principles of constant curvature and zero torsion. To demonstrate that the assumptions are valid and rooted in the mechanics of the catheter's distal shaft, the statics of catheter deflection was studied and a methodology was presented to verify the assumptions.

To control the position of catheter tip and realize navigation, inverse kinematic control using DLS method was proposed and an architecture was designed to realize navigation. The details and implementation of the navigation architecture, along with the components of the navigation system are presented in the next chapter.

Chapter 3

Navigation Platform[1]

3.1 Introduction

In chapter 2 an architecture was developed to realize catheter navigation. In this chapter, the implementation of the architecture and the major components of the navigation system are described. The internal mechanism of each component is also explained, and the interactions between the components are outlined.

Based on the navigation scheme demonstrated in figure 2.11, the following components of the system are identified. Figure 3.1 illustrates an overview of major system components and their interactions. A conceptual setup of the system components in catheterization lab is provided in figure 3.2.

Robotic Assistant - The robotic system that manipulates the catheter handle/body and replaces the electrophysiologist's hand. Section 3.2 provides the detailed specifications of the constructed robotic mechanism.

Position Tracking - The catheter position feedback is the critical sensory data required for the navigation. To track distal shaft's position, the Aurora® electromagnetic (EM) measurement system (NDI, Waterloo, ON, Canada) is deployed as elaborated in section 3.3.

3D Input - To allow for an intuitive mechanism for the electrophysiologist to direct the navigation of the catheter, an input device capable of three-dimensional position input is utilized along with the GUI. The operator can use this device to command the navigation of the catheter, as described in section 3.4.

[1]This chapter is partly published in [42, 44, 43].

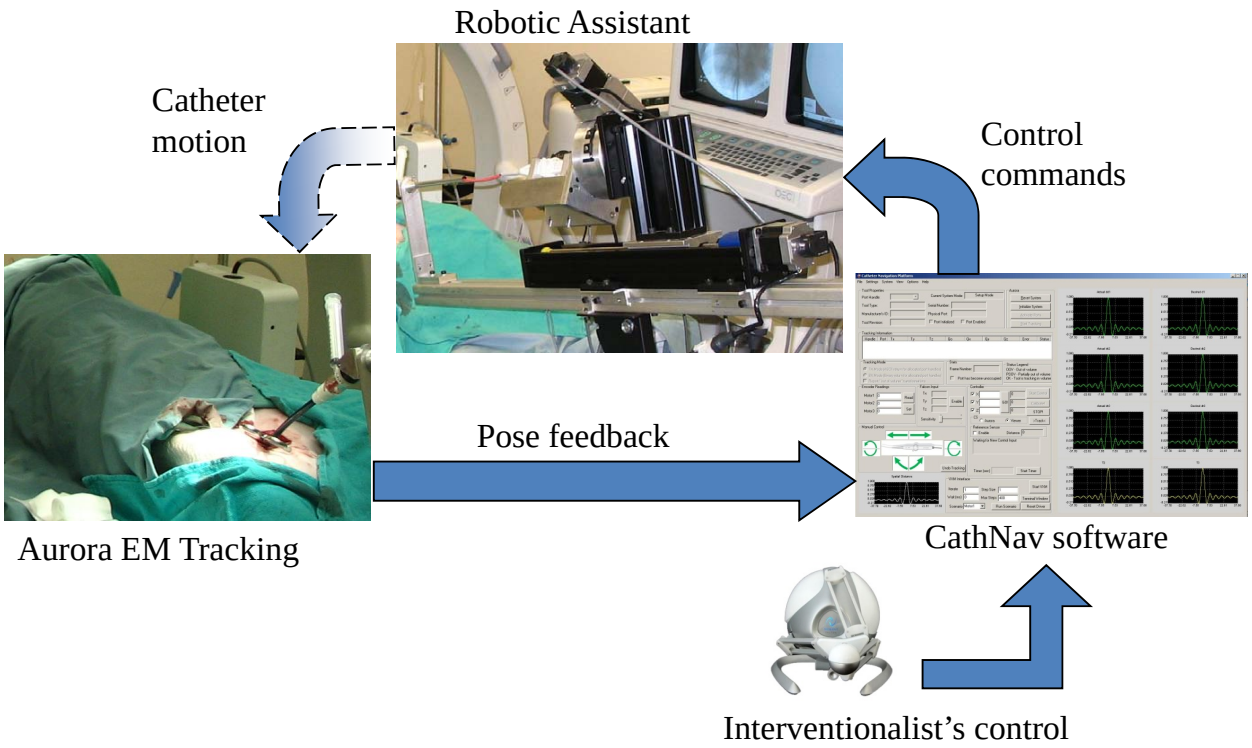

Figure 3.1: An overview of system components and their interactions.

Navigation Software - The heart of the navigation system is its software that implements all the control algorithms, interfaces with robotic assistant, position tracking, and other external components of the system, and provides the graphical user interface (GUI) for the operator/interventionalist to supervise and manage the navigation sequence. The software was named CathNav. Section 3.5 provides the software design, and its features, functionalities, and their implementation.

In addition to the system components, the calibration algorithm, model parameter estimation method, and coordinate systems conversion procedures are reviewed in sections 3.6. Finally, an overview of the robot controller is provided in section 3.7.

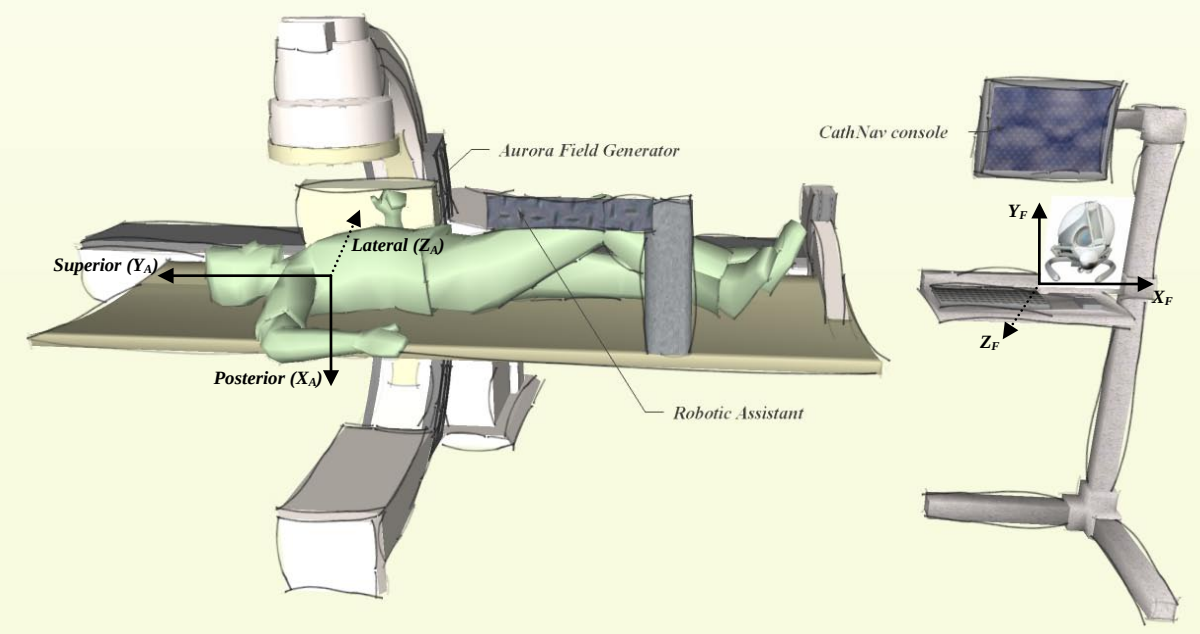

Figure 3.2: Conceptual setup of the system in the catheterization lab. The main coordinate systems (see section 3.6.3) are illustrated.

3.2 Robotic Assistant

3.2.1 Design Specification

The electrophysiologist manipulates the catheter handle/body by three DOFs: twisting the handle/body to achieve twist at the distal shaft, controls the steering knob to achieve deflection at the distal shaft, and inserting/retracting the catheter into/from the entry port (e.g., femoral vein) to realize displacements at the distal shaft. As the three DOFs are decoupled motions, the robotic platform can be constructed by assembling ready-made linear/rotary stages, each actuating one DOF. The main advantage of ready-made stages is that all the precision machining is done by the stage manufacturer, the backlash or slippage is usually negligible and the package is conveniently sealed, all of which make such stages a suitable choice for an academic prototype system. The stages can be actuated with stepper or servo motors.

The platform shall be positioned beside the catheter entry port that is in the upper thigh of the patient. The catheter is mounted on the robot, so that the robot can perform the manipulations on the catheter. The platform can be composed of a linear slide for insertion/retraction of the catheter, and a rotary stage that is

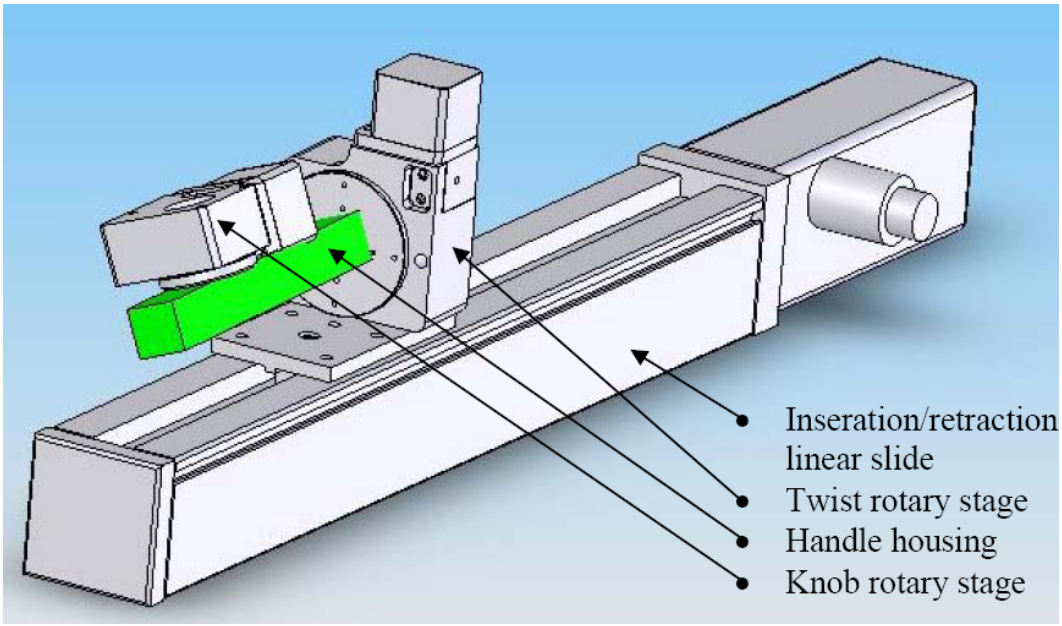

Figure 3.3: The conceptual design of a robotic assistant composed of linear and rotary stages.

mounted on top of the slide. A fixture containing the housing of the catheter handle needs to be designed and mounted on the rotary stage parallel to the linear slide. On the housing, a second low-speed low-profile rotary stage will be installed which turns the steering knob on the handle. The design concept is illustrated in figure 3.3.

The specifications for the stages of the robotic assistant are summarized in table 3.1. The travel range is given based on the catheter's specification, assuming that catheter insertion prior to intracardiac navigation is performed manually. The resolution and accuracy parameters are based on the measurement system capabilities. Appendix A provides more details on how the specifications are calculated. Compared to human operator's performance in catheter manipulation, the accuracy is beyond human capabilities. Resolution and speed are subject to limits of human motor control, no study of which is available in the context of catheterization.

The catheter operates on the principle that a flexible tube can transfer motion from one end to the other when constrained in a luminal structure. When the robotic assistant operates, a proximal portion of the catheter body lies outside of the patient body. This flexible portion is not constrained, and can kink and bend that limits the effective transfer of the handle twist and translation to the distal shaft effectively. A telescopic tubular mechanism that constrains the catheter body

Table 3.1: The specifications for linear and rotary stages of the robot.

Parameter	Linear translation	Handle twist	Knob control
Travel Range	24.22 cm	±540°	±45°
Resolution	0.2 mm	0.1°	0.025°
Accuracy	0.3 mm	0.2°	0.05°
Max Speed	67 mm/s	360°/s	45°/s

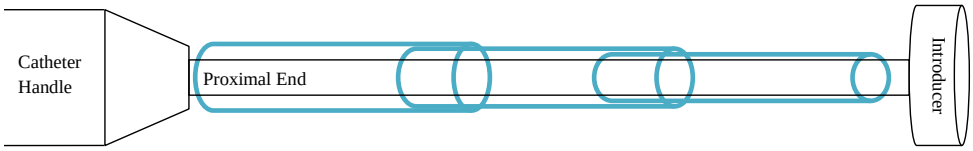

Figure 3.4: The conceptual diagram of a telescopic mechanism between the catheter handle and its port of entry into an introducer sheath.

between the handle and the port of entry resolves this issue. The mechanism has to keep the proximal section straight, while allowing for its insertion into and retraction from the port of entry. It should also allow the catheter to twist. The range covered by this mechanism from full retraction to full expansion depends on the size of the animal/patient and the catheter itself. Figure 3.4 provides a conceptual diagram of a three-section telescopic mechanism in operation. For the standard catheter length of 110 cm, the length of the mechanism could vary between 20 cm (fully retracted for a large animal) to 70 cm (fully expanded, for an adult patient).

3.2.2 Constructed Robot

The constructed robotic assistant is composed of stages manufactured by Velmex, Inc. (Bloomfield, NY). The specifications of the robot is presented in table 3.2.

The robotic assistant is illustrated in figure 3.5. The stages are all operated by stepper motors coupled with shaft encoders. The motors operate at 400 steps per revolution. The encoders are 400 counts per revolution and when used in quadrature mode provide 1/4 step resolution, yielding 0.0125° and 0.05° resolution for handle twist and knob control stages respectively. The linear stage, is composed of a lead screw providing a translation of 0.4 inch per turn coupled directly with the stepper motor's shaft. The handle twist stage has a gearbox with a reduction ratio of 72:1. The knob control stage has a gearbox ratio of 90:1. The linear stage has two limit

Table 3.2: The specifications of the constructed robotic assistant.

Parameter	Linear translation	Handle twist	Knob control
Model Number	BiSlide MN10-0100-E04-21	B4818TS	B5990TS
Travel Range	25.4 cm	-	-
Resolution	0.0254 mm	0.05°	0.01°
Accuracy	0.0762 mm	0.2°	0.05°
Max Speed	304.8 mm/s	200°/s	40.2°/s
Max Power/Torque	56.49 Nm	56.49 Nm	2.26 Nm

switches at both ends, and each rotary stage has a zero reference switch.

The linear stage acts as the base of the robot. The handle twist rotary stage is attached to a vertical post mounted on the sliding plate of the linear stage. An L-shaped adapter piece was attached to the twist rotary stage. On the adaptor the knob control rotary stage was mounted. A small fixture machined to couple the steering knob was assembled on the knob control stage. A sliding fixture was also mounted on the L-shaped adapter to hold the catheter handle coupled with the knob control rotary stage. The sliding feature of the fixture allows for easy mounting and unmounting of the catheter handle. In animal experiments described in chapter 5, the robot was mounted on an adjustable stand so that the height and angle of the catheter could be adjusted with respect to the animal body and point of entry.

The three motors of the assembly are driven and controlled by a pair of master-slave VXM stepping motor controllers (Velmex Inc., Bloomfield, NY) each capable of controlling two motors simultaneously. VXM connects to the computer via RS-232 serial interface at up to 38400 bits per second data rate. The three shaft encoders are connected to a four-channel encoder interface (USB1, US Digital, Vancouver, WA). The encoder interface provides the encoder readings to the host computer via a USB[2] interface. Further details on how the navigation software controls the robotic assistant is provided in section 3.5.

3.3 Position Tracking

Electromagnetic (EM) tracking is becoming an established medical navigation tool. Aurora® (NDI, Waterloo, ON, Canada) is an EM tracking system with verified accuracy and applicability [56, 57, 58]. In 6DOF measurements, Aurora® achieves

[2]Universal Serial Bus.

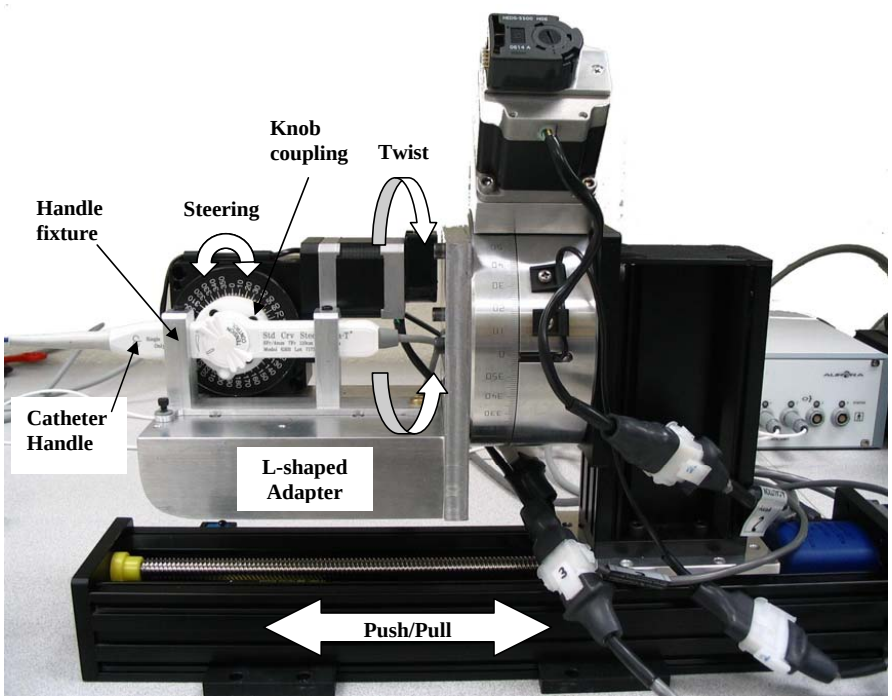

Figure 3.5: Three degree-of-freedom robotic assistant. The catheter handle is mounted on the robot.

an RMS accuracy of 0.6 mm in position and 0.4° in orientation. The precision values are 0.4 mm and 0.2° in position and orientation, respectively. Both precision and accuracy figures are at normal operating conditions where no source of distortion is present.

The Aurora® system is composed of three main components:

- Field Generator - It generates an electromagnetic field realizing the measurement volume for the system. The sensors are tracked within the measurement volume. In the deployed system, the volume is a cube of 50×50×50 cm.
- System Control Unit (SCU) - It powers the field generator, interfaces with the sensors and provides the measurement readings through a serial RS-232 interface to the host computer. The measurements can be read at an update rate of 40 Hz.
- Flexcord sensors - Each sensor coil can provide a 5 or 6 DOF pose reading. Each sensor connects to SCU through a Sensor Interface Unit (SIU). 6DOF sensors are actually two 5 DOF coils fixed relative to each other and secured in a polyimide tube. Figure 3.6(a) displays the schematics of a 6DOF sensor

coil. For each sensor, the measurements are provided in terms of the 3D vector of position coordinates and a quaternion representing the orientation, with respect to the field generator's coordinate frame, shown in figure 3.2. In 5DOF measurements, the rotation of a sensor around its lengthwise axis is not measured.

Two sensor coils were used to track the catheter position and to estimate the catheter model's joint parameters. One sensor coil was attached to the base of the distal shaft (at O_1 in figure 2.4) and the other sensor was attached to the tip section (O_4O_6 in figure 2.4). Figure 3.6(b) shows a close-up of the sensors attached to the distal shaft. The sensors were glued to the shaft using contact cement and then were rubber-coated for a better bond and seal. In order to match the model with catheter's actual position, the pose readings from the sensors were calibrated so that the base sensor represented O_1 and the readings from the tip sensor yielded the position of O_4 and O_6. Sensor attachment and calibration procedures are presented in section 3.6.1. A heat shrink tubing was used as a sheath that covered the catheter body and sensor wires that ran along the catheter body in parallel. The added thickness of the sensors and the sheath, increased the asymmetric tracked catheter's diameter to 15-18F. The sheath-covered tracked catheter will be referred to as catheter assembly henceforth.

3.4 3D Input Device

To control the position of the catheter tip and to navigate the catheter in the 3D space, a 3D input mechanism is required. The 3D input allows the system operator to enter a 3D vector of displacements or positions. The navigation software provides the option to enter such a value through the keyboard. However, keyboard input is not an intuitive choice for use in the operating room. The regular computer mouse lacks a third dimension. A 3D input device is required for this purpose.

A 3D mouse named SpaceNavigator™(3Dconnexion, Fremont, CA) was first selected as the navigation console. A picture of this device is provided in figure 3.7(a). The device was integrated with CathNav and was tested to control the catheter position. However, the coupling between the mouse's three DOFs due to its input mechanism and its small form factor undermined precise input to the computer. For instance, it was very difficult to command a displacement along a specific axis. It was also difficult to adjust the absolute value of the displacement as desired. As a result, a better input device was sought.

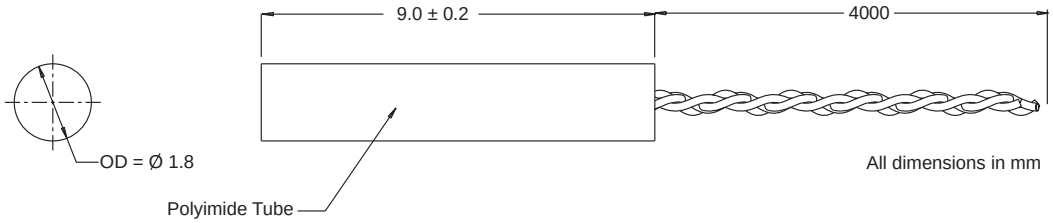

(a)

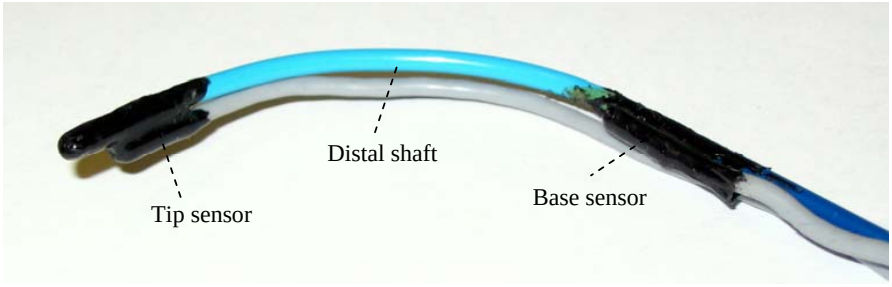

(b)

Figure 3.6: (a) The schematics of a 6DOF flexcord. (b) Aurora®sensors attached to the distal shaft of the catheter.

(a) (b)

Figure 3.7: (a) SpaceNavigator™3D mouse. (b) Falcon 3D input device.

3D Joysticks are also possible choices, but due to their low resolution and range of input, such devices are not suited for this application. Falcon (Novint, Albuquerque, NM) is a low-cost 3D input device with an intuitive input mechanism, designed similar to a Delta parallel robot [59]. The device is illustrated in figure 3.7(b). It has a 3D workspace of 10×10×10 cm with a position resolution of 400 dpi[3] or 0.635 mm. It can also generate a force feedback of more than 2 lbs. The force feedback feature of the device is not used in CathNav currently, but it could be utilized in future developments to provide some form of tactile feedback to the operator. This possibility is further discussed in chapter 6.

The 3D input vector is used in assisted mode of navigation in the software, as described in the subsequent section.

3.5 Navigation Software

3.5.1 Introduction

CathNav, the navigation software developed in this project, is the core component that interfaces with all the devices of the system, provides the user interface for

[3]dots per inch

the operation of the system and implements the navigation architecture presented in section 2.5. In the following subsections, the software functionality, design and inner mechanisms are presented.

3.5.2 Software Functionality

The main function of CathNav software is to interface with the various devices of the system to realize navigation through the collective control of all the devices. The hardware interfaces of the devices include:

1. Motor controllers - The pair of VXM controllers interface with the computer through one RS-232 serial interface at the data rates up to 38400 bits per second (bps).

2. Encoder interface - The USB1 encoder reader device interfaces with the computer through one USB 1.0 interface, at the speed of up to 12 mbps. It can sample up to four encoders at the rates of up to 1.5 MHz for quadrature cycle input.

3. Aurora®- It interfaces with the computer at the speed of 112,500 bps. Up to four sensor pose readings are provided at the rate of 40 Hz.

4. Falcon input device - It interfaces with the computer through a USB 2.0 interface at an update rate of 1000 Hz.

CathNav is installed on a portable computer that does not have any serial interface. Both Aurora® and VXM serial interfaces connect to the computer through USB-to-Serial adaptors. As a result, a total of four USB devices are connected to the computer via a four-port USB hub. The software is developed in Visual Studio 2005 environment in Visual C++ programming language and runs on Windows Vista operating system. It is written utilizing object orienting programming (OOP) methodologies and is based on MFC (Microsoft Foundation Classes). For vector, quaternion and matrix processing, VL Vector Libraries [60] were utilized.

CathNav is responsible for initialization, configuration, and operation of the devices. Each device communicates with the computer through its own communication protocol and driver interface at different data rates with different sampling rates. The main requirement of CathNav is to control the system devices with their heterogeneous interfaces so that real-time catheter navigation can take place. To

achieve this goal, the software design cannot follow the traditional single-thread sequential programming paradigm. The design of CathNav and how it accomplishes this requirement is elaborated on in the following section.

3.5.3 Software Design

CathNav's main function is to implement closed loop real-time position control of the catheter. This means the readings from external devices are needed to be provided to the controller at the rate equal to the bandwidth of the controller and the controller's output must be issued to the devices at the same rate. Real-time control of multiple input/output (I/O) devices requires a multi-threaded approach to software development. In this approach, the software is composed of a number of parallel subprocesses or threads, each communicating with one or more devices. Although the computer has only one CPU (central processing unit), the threads can share the CPU by divining the CPU time between each other and by releasing the CPU when blocked on an I/O operation. The threads share the same memory space within the program. However, they need synchronization and inter-process communication (IPC) mechanisms so that they can coordinate the division of the processing tasks between them. CathNav was designed to realize the task of real-time navigation following a multi-threaded paradigm.

The input/output mechanism of each device of the system determines whether a dedicated thread is required to handle data communication with the device. To reach the overall software design, the I/O mechanism of the devices are revisited:

1. Motor controllers - The VXM accepts program code written in the form of an ASCII string through the serial interface. The VXM runs the program and returns a special character (‘^’) indicating it is ready to accept new command codes. Using the VXM driver, CathNav needs to issue a command, wait for the response and then issue a new command. The controllers cannot be interrupted or receive a new command while the previously issued command is being executed. It turns out that VXM is the slowest device that CathNav communicates with. To achieve the fastest communication rate possible, a dedicated thread is required to issue a new command upon acknowledgement of the previous command received from the VXM on the serial port.

2. Encoder interface - The driver for the encoder interface, provides the latest encoder readings through a simple function call. CathNav does not need to

busy-wait for the response, as it returns without delay. No dedicated thread is required to call this function.

3. EM Sensor - Aurora® has a specific protocol for text or binary communication with the host computer. After initialization, to read latest sensor measurements, a command is issued to Aurora® through the serial interface, and the response is received within 25 ms. A thread is required to scan Aurora® at the fastest rate possible.

4. Falcon input device - The driver provides the position readings through a call-back mechanism. The call-back function updates the readings every 1 ms. Similar to the encoder interface, no dedicated thread is required for this device.

Two dedicated threads are required to handle communication with four devices as summarized above. The controller can have a separate thread that receives position feedback from Aurora® and controls the robotic assistant through the VXM based on the operator input from 3D input device or GUI. This thread can implement the navigation architecture, seen in figure 2.11. Figure 3.8 illustrates CathNav software components and the data flow between them. As seen in the figure, AuroraThread realizes communication with Aurora® system and saves pose readings in a data structure called AuroraData. This data structure is guarded with a semaphore through which access to pose readings is synchronized between AuroraThread and ControlThread. ControlThread performs the main task of navigation and issues commands to VXMThread. VXMThread implements the low-level control of the robot actuators through VXM.

CathNav is the main program that launches all the threads. The main CathNav process implements the graphical user interface (GUI) of the system. The user operates the system through the GUI. CathNav controls the operation of the threads based on the user input received from GUI. The CathNav navigation features and GUI are presented in the subsequent sections.

3.5.4 Navigation Levels

The main task of CathNav is to realize navigation. Utilizing a flexible design, based on hierarchical navigation architecture presented in section 2.5, CathNav provides the option to its operator to navigate the catheter at three level of automation as follows:

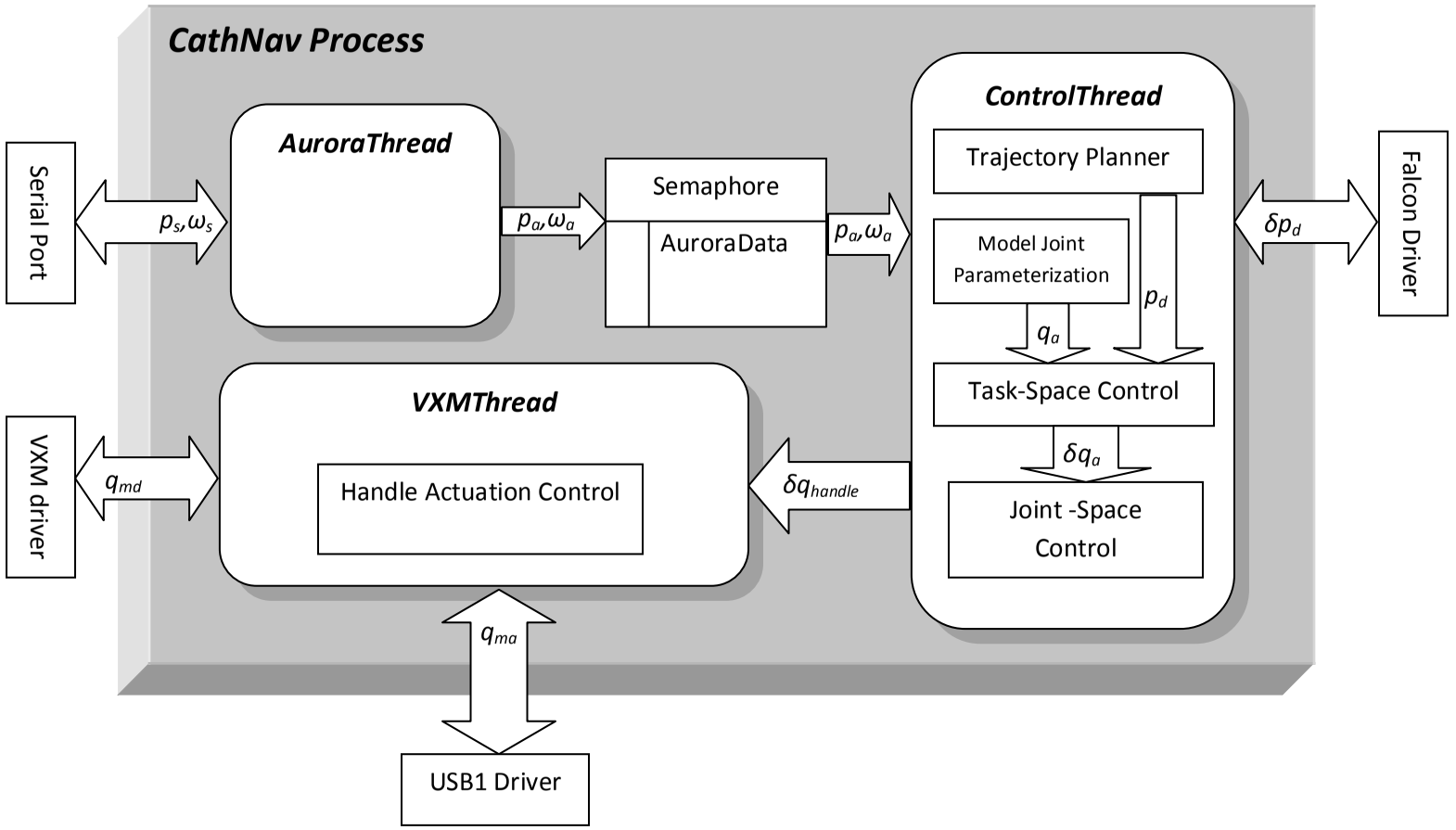

Figure 3.8: The overall design of the CathNav software including the main components and the data flow between them. p stands for position and ω denotes orientation. The subscripts m and s indicate robot motor and EM sensor parameters respectively. Similarly, a and d denote actual and desired values.

Motorized Navigation - At this level, the operator can command the three DOFs of the robotic assistant directly. Through the CathNav user interface the operator can twist, bend and translate the catheter by directly moving the stages of the robot. This feature is available so that the convenience of manual manipulation can be utilized with precise and direct control of the robot. The commands issued at this level constitute the set points of handle actuation control.

Assisted Navigation - Using the 3D input device, or through CathNav user interface, the operator can provide direction vectors to the task-space controller. This way the system can move the catheter tip as commanded by the operator. At this level, the catheter manipulations to move the catheter in the commanded directions are calculated and realized automatically by the system.

Automatic Navigation - At the highest level, only the target position vector is provided to CathNav's trajectory planner and the system takes the catheter tip from its current position to the commanded target position.

By the three modes of navigation available in CathNav, the operator has a new set of tools to utilize for effective catheter steering and navigation. The next section, describes the CathNav user interface.

3.5.5 Graphical User Interface

The graphical user interface (GUI) of the system serves as the control panel through which a user such as an electrophysiologist can supervise and manage the operation of the navigation system. Through the GUI, the user monitors the status of the system and the sensor readings, issues commands to the navigation system, and directly manipulates catheter handle through the system. Figure 3.9 illustrates the main window of the GUI.

In figure 3.9, the window is divided into four main areas each serving a specific functionality, described as follows.

1. Aurora - The user can initialize and reset Aurora® system, activate sensor ports and start/stop tracking of the sensors. In tracking mode, the actual sensor data (position p_s and orientation ω_s in figure 3.8) is read continuously from the device by AuroraThread and is displayed in "Tracking Information"

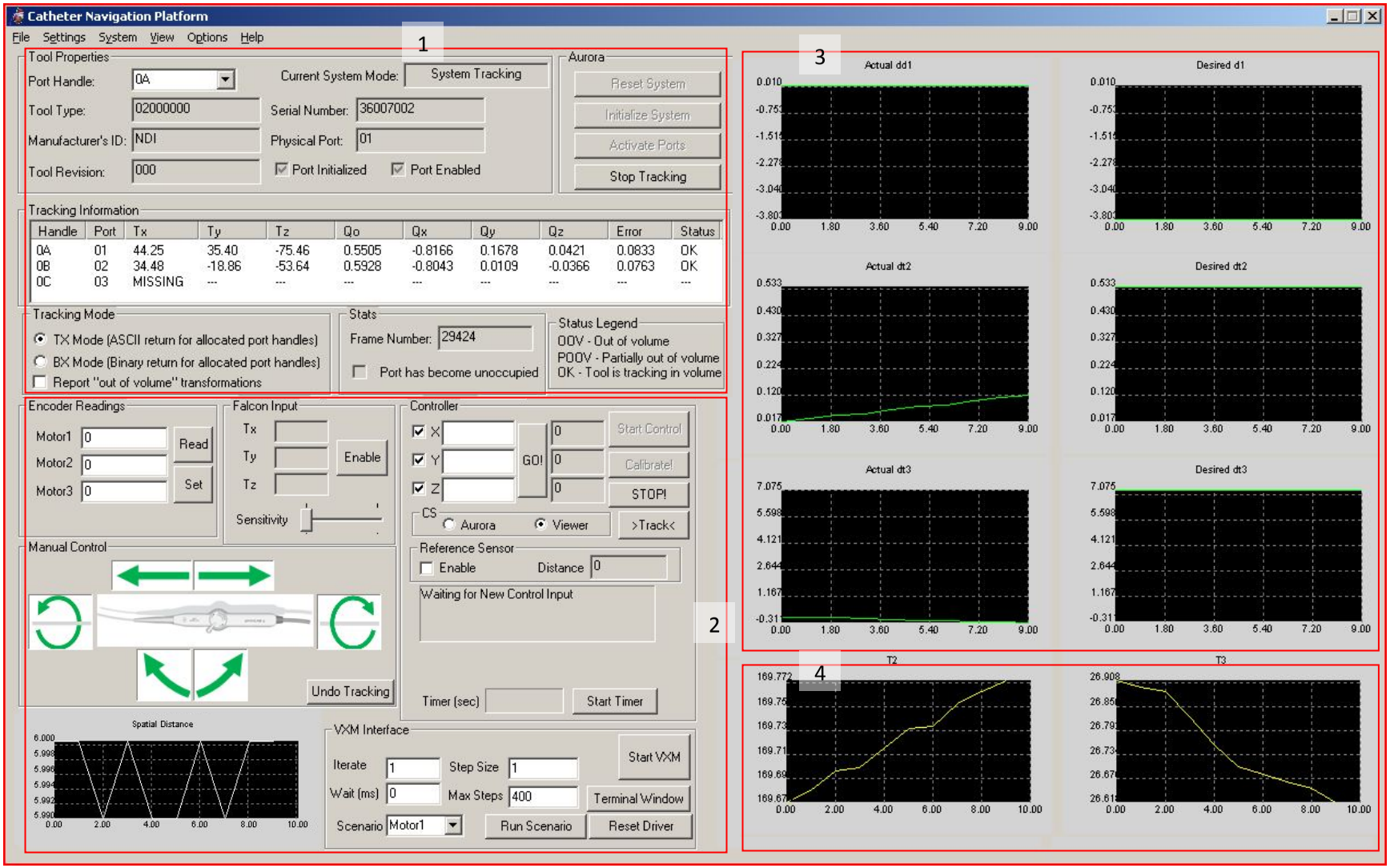

Figure 3.9: The graphical user interface of CathNav software.

group box. Various Aurora® system parameters are also displayed in this area.

2. Navigation - This area is the main section of the GUI. The group boxes in this area include:

   - Controller - Through the user controls provided in this group box, the operator can enter the 3D set points (δp_d) for the task-space controller for assisted navigation. Automatic navigation is also commanded from this area. CathNav displays messages to the user regarding its current status of the navigation or control tasks in this area. The operator can override the navigation at any instant by pressing the 'STOP' button in this area, to safely halt automatic navigation or to restart navigation to a different target. A stop-watch timer is also provided in this section that is used to measure the duration of different manoeuvres in the experiments.
   - Falcon Input - The input received from the Falcon (δp_d in figure 3.8) is displayed in this box. The sensitivity to the device inputs is also adjusted here. δp_d is scaled by the sensitivity level factor. Higher sensitivity levels imply desired position p_d provided to task-space controller is further away from the current position p_a.
   - Encoder Readings - In this box, the current position of robotic assistant actuators (q_{ma} in figure 3.8) are displayed. Each encoder's counter is read as quadrature pulse counts and is converted to the displacement position or rotation angle of their corresponding Velmex stages.
   - Manual Control - This area provides the facility to directly manipulate the catheter handle as desired for motorized navigation. The operator can enter the desired handle parameters (q_{handle} in figure 3.8) through this area. In in-vivo validation experiments, described in chapter 5 , this feature is also used to return the catheter to a base position. "Undo Tracking" button in this box allows the user to command the system to reverse all the manipulations performed on the handle during a navigation session, to return the catheter to its original position.
   - VXM Interface - Through this box, the user can send commands to the VXM directly. Various manipulation scenarios can be readily chosen in this box. The scenarios manipulate the handle through different trajectories and return back to the beginning position. This feature was

developed and utilized extensively in in-vitro validation experiments, presented in chapter 4.

- Spatial Distance - This graph tool displays the task-space controller's performance in terms of the distance of the catheter tip to the target position set for the controller ($|p_d - p_a|$ in figure 2.11) in mm versus time in seconds. In other words, the overall performance of navigation is readily displayed in this graph.

3. Joint Space Controller Graphs - This area contains graphs that display the performance of the joint-space controller. The three graphs on the left display the actual joints differential displacement (δq_a). The corresponding graphs on the right, are the desired joint parameters (δq_d) as set by the task-space controller. All joint displacements (in mm or degrees) are plotted versus the joint-space controller's iterations.

4. Joint Parameters - The twist and deflection angles (θ_2 and θ_3) in degrees are plotted versus joint-space controller's iterations in the two graphs in this area.

3.6 Underlying Algorithms

To achieve catheter navigation, CathNav relies on some fundamental algorithms for calibration, model parameters estimation and measurement, and conversion of coordinate systems between the Aurora® system, the 3D input device, the robotic assistant and the distal shaft model. In this section, those algorithms are reviewed.

3.6.1 Position Calibration

The most critical component of the navigation system is the position tracking of the catheter's distal shaft. Aurora® system provides the position and orientation of the sensor coils located inside the measurement volume of its field generator. However, the sensor readings do not represent a point on the catheter's centre line. The kinematic model provides an estimate of catheter's centre line configuration. To utilize the proposed modeling in navigation, the position of actual points on catheter's centre line are inferred from the sensor readings. As mentioned in section 3.3, two 6DOF sensors are used to represent the base and the end of the deflecting section of distal shaft. There is an offset between the actual points on the catheter

and the sensors. This offset needs to be found through a calibration process prior to the deployment of the system.

The offset is used to adjust the sensor readings during the actual operation of the system. However, prior to finding this offset, a suitable arrangement of the sensors attached to the distal shaft must be devised. The sensors should be attached to the catheter minimizing their adverse effects on the dynamic properties of the catheter (e.g., bending and flexibility). The sensor coils are rigid and their wires are flexible. As a result, the coil cannot be attached to a the flexible section of the distal shaft.

Figure 3.10 depicts possible sensor configurations with respect to the distal shaft. In all configuration, the tip sensor is mounted on the side of the bending plane of distal shaft, so that it does not restrict the catheter's deflection in both directions. By attaching both sensors to one side of the catheter, as seen in figure 3.10(a) it is possible to assume that the sensors are located at the centre line of a virtual catheter passing through the sensors, and no special correction of position readings would be required. In this case however, the sensor wires would have to overlap in the catheter assembly and distal shaft bending might be disrupted by the wires.

An ideal case could be to attach the sensors on both sides of the catheter, as shown in figure 3.10(b). When the distal shaft is lying straight as in the figure, the average of position readings will yield the middle point on the distal shaft's centre line and the calibration can be simplified. The symmetry of this configuration, results in a smooth and symmetric catheter assembly as well. However, such configuration results in the maximum diameter of the assembly which is not desired.

The third possibility, shown in figure 3.10(c), does not pose the issues of the other two options. The configuration of the sensors on the catheter in figure 3.6 follows this scheme. It is noted that the smoothness of the catheter surface with attached sensors as well as the overall diameter is an important practical issue. Smaller and smoother assembly facilitates insertion and deployment in-vivo.

To find the parameters of kinematic model (see figure 2.4), the position vectors of O_1 and O_4, or both ends of the deflectable section are needed. The distal tip position O_6 is also required as the navigation goal is to control distal tip position. This means from the position readings of the two sensors, three landmark positions (O_1, O_4, O_6) have to be calculated. The relative position of the landmarks with respect to the sensors can be assumed constant. Each sensor has its own coordinate system that is constant too. If the vector connecting base sensor (S_1) to O_1 is

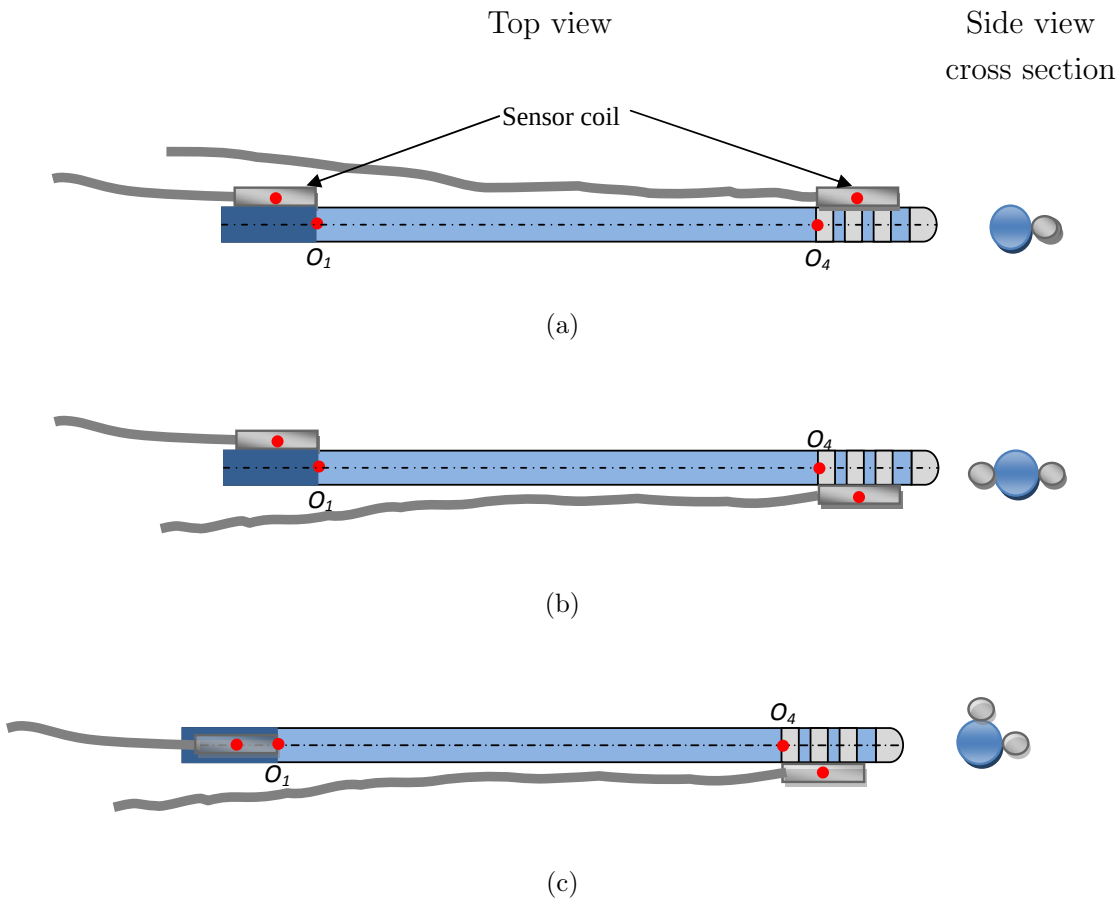

Figure 3.10: Possible configurations of Aurora® sensor coils attached to the distal shaft of the catheter. The top view of the distal shaft is demonstrated on the left with the sideview's cross section on the right. The dot on the sensor coil represents its centre point whose position is reported. The dots on the catheter are O_1 and O_4. (a) Both sensors are attached to one side aligned with each other . (b) Each sensor is attached to one side of the catheter. (c) Tip sensor is attached to the side and the base sensor is attached on the top.

found through calibration, it can be used to map base sensor position to distal shaft base position. Similarly, the tip sensor (S_2) position can be mapped to O_4 and O_6. The resultant mapping vectors will be the characteristic parameters of any specific catheter assembly, that can be experimentally found once and then utilized in navigation. The vectors are demonstrated in figure 3.11. The X and Y and Z axes in sensor coordinate frame are fixed by construction and do not change.

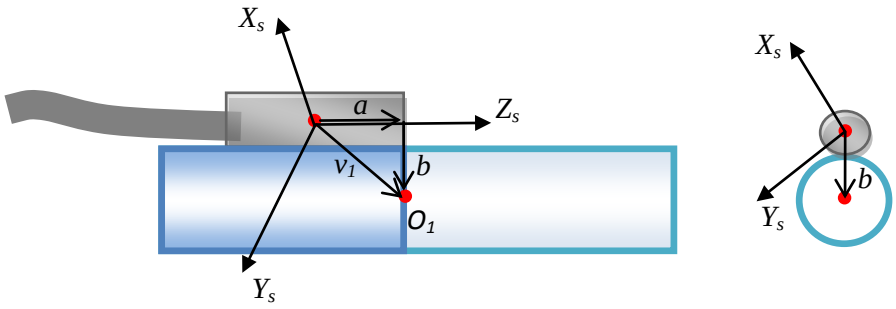

(a)

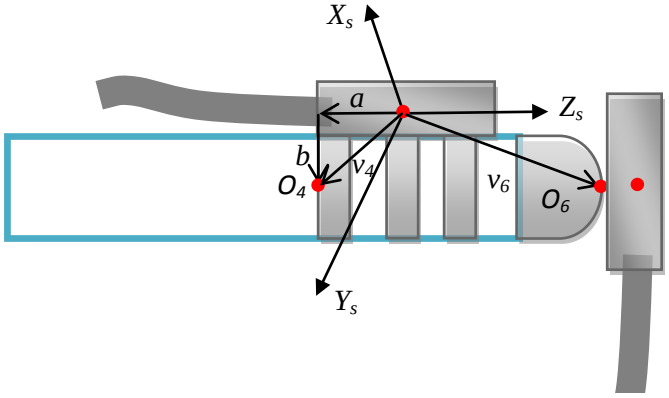

(b)

Figure 3.11: (a) Base sensor calibration vectors, (b) Tip sensor vectors along with a third sensor used for calibration.

In the following, all position vectors are in Aurora®field generator's coordinate frame which serves as the global coordinate system across all navigation modules. Position readings of the sensor coils are by default in Aurora® coordinate frame. In all the calibration algorithms to follow, coordinate system conversion is the main component that is explained in section 3.6.3. The calibration vector for O_1, denoted

by $\vec{v_1}$ is calculated as,

$$^{S}\vec{v_1} = {}^{S}\vec{a} + {}^{S}\vec{b} \tag{3.1}$$

where $^{S}\vec{a} = (0, 0, l_S/2)^T$ in sensor coordinate frame and $|^{S}\vec{b}| = r_S + r_C$. l_S denotes the length of the sensor coil, r_S is the radius of the coil, and r_C is the radius of the distal shaft. A similar relationship holds for the tip sensor,

$$^{S}\vec{v_4} = {}^{S}\vec{a} + {}^{S}\vec{b} \tag{3.2}$$

where $^{S}\vec{a} = (0, 0, -l_S/2)$ in sensor coordinate frame and $|^{S}\vec{b}| = r_S + r_C$. To find vector $^{S}\vec{b}$, the following procedure is used:

Algorithm 3.1 Finding calibration vector $\vec{b}$

1: **repeat**
2: Fixate the catheter assembly so that vector $\vec{b}$ is vertical visually
3: $^{A}\vec{b} = (-(r_S + r_C), 0, 0)$, where $^{A}\vec{b}$ is vector $\vec{b}$ in Aurora® coordinate system
4: Convert vector $^{A}\vec{b}$ to sensor coordinate frame vector $^{S}\vec{b}$
5: Record the newly found $^{S}\vec{b}$
6: **until** error criterion is met
7: The mean calculated $^{S}\vec{b}$ vector is assumed to be the actual $\vec{b}$

In algorithm 3.1, to achieve a 95% confidence interval in calibration, the error criterion could be defined as $(t_{0.025,n-1}\sigma_{|^{S}\vec{b}|}/\sqrt{n}) < \epsilon_d$ where n is the number of measurement repetitions, $t_{0.025,n-1}$ stands for 95% confidence t-distribution quantile at $n-1$ degrees of freedom, $\sigma_{|^{S}\vec{b}|}$ is the standard deviation of $|^{S}\vec{b}|$ measurements and ϵ_d is the desired precision [61].

Tip position vector $^{S}\vec{v_6}$ is found using a third sensor coil (S_3), through the following steps:

Algorithm 3.2 Finding calibration vector $\vec{v_6}$

1: **repeat**
2: Fixate a third Aurora® sensor coil so that its centre touches the tip of the catheter (O_6), as in figure 3.11(b)
3: Let $\vec{S_2}$ and $\vec{S_3}$ be the position readings from the tip and the third sensor respectively
4: Construct vector ${}^{A}\vec{v_6} = \vec{S_3} - \vec{S_2}$
5: Convert vector ${}^{A}\vec{v_6}$ to ${}^{S}\vec{v_6}$ in sensor coordinate frame
6: Record the newly found ${}^{A}\vec{v_6}$
7: **until** error criterion is met
8: The mean calculated ${}^{S}\vec{v_6}$ vector is assumed to be the actual $\vec{v_6}$

In algorithm 3.2, the error criterion is defined for ${}^{S}\vec{v_6}$ similar to algorithm 3.1. In fact, vector $\vec{v_6}$ found through the above procedure provides the position of a point at a distance r_s from O_6.

When calibrated $\vec{v_1}$, $\vec{v_4}$ and $\vec{v_6}$ are found, the position vectors of distal shaft base (O_1), distal end of the deflecting section (O_4), and tip of the catheter (O_6) can be calculated at any configuration, as follows.

Algorithm 3.3 Finding distal shaft model key positions

1: Convert $\vec{v_1}$, $\vec{v_4}$ and $\vec{v_6}$ to Aurora® coordinate frame
2: $\vec{O_1} = \vec{S_1} + {}^{A}\vec{v_1}$, where $\vec{S_1}$ is the position vector of the base sensor
3: $\vec{O_4} = \vec{S_2} + {}^{A}\vec{v_4}$, where $\vec{S_2}$ is the position vector of the tip sensor
4: $\vec{O_6} = \vec{S_2} + {}^{A}\vec{v_6}$

3.6.2 Model Parameters Estimation

Catheter model's parameters, including translation d_1, twist angle θ_2 and deflection angle θ_3 are the key data required for navigation. However, as the catheter is a flexible device, finding the rigid model parameters is inherently challenging. The sensor configuration and the method to measure position of the base of the distal shaft (O_1), the end of the deflectable section (O_4) and the tip of the catheter (O_6) were outlined in section 3.6.1. In this section, the algorithms to extract model parameters from pose measurements are explained.

Parameter estimation for joint-space control

For joint-space control, the differential variations of joint parameters ($\delta q_a = (\delta d_1, \delta\theta_2, \delta\theta_3)$) are required. The differential variations are calculated directly from pose measurements at two consecutive sensor readings. In the following, we assume the consecutive measurements occur at time instants t_1 and t_2. All the measured vectors are assumed to be in the Aurora® coordinate system. All scalar joint parameters are found so that they correspond to the model parameters as illustrated in figure 2.4.

Translation

The translation parameter (d_1) calculation is straight-forward using the consecutive positions for O_1, calculated from S_1 readings as elaborated in section 3.6.1 . The magnitude of the displacement vector yields the translation,

$$\delta d_1 \cong |\vec{O_1}(t_2) - \vec{O_1}(t_1)| \;\; sign(\; {}^A\vec{z_S}(t_1) \cdot (\vec{O_1}(t_2) - \vec{O_1}(t_1))) \tag{3.3}$$

where ${}^A\vec{z_S}$ is the unit vector along the Z axis of base sensor (S_1) in Aurora® coordinate frame, calculated by converting unit vector ${}^S\vec{z_S} = (0, 0, 1)^T$ to Aurora® coordinate frame, as described in the subsequent section. To find the direction of translation, the displacement of catheter is projected on the sensor's Z axis that is always pointing in the positive direction. Using formula 3.3, if the distal shaft base is translated parallel to the centre line of base sensor (S_1) toward the tip of the sensor coil, a positive translation is measured. Motion in the opposite direction results in a negative translation measurement.

Twist angle

To measure the twist angle (θ_2), a method is required to find out how much the distal shaft base has been rotated around the catheter's centre line. Base sensor S_1 orientation readings can be used to measure the rotation angle of the sensor. To relate the sensor's rotation angle to the twist angle at O_1, we use the following principle from plane geometry:

When a plane is rotated by an angle β about a vector normal to the plane, any vector in the plane is rotated by the angle β.

Base sensor S_1 is attached parallel to distal shaft base. This means any twist at the base, is a rotation about a normal to XY plane of S_1 local frame, i.e., its Z_S axis (see figure 3.11(a)). As a result, the rotation measured in XY plane will be equal to the twist angle. Any vector in XY plane can be used to calculate the

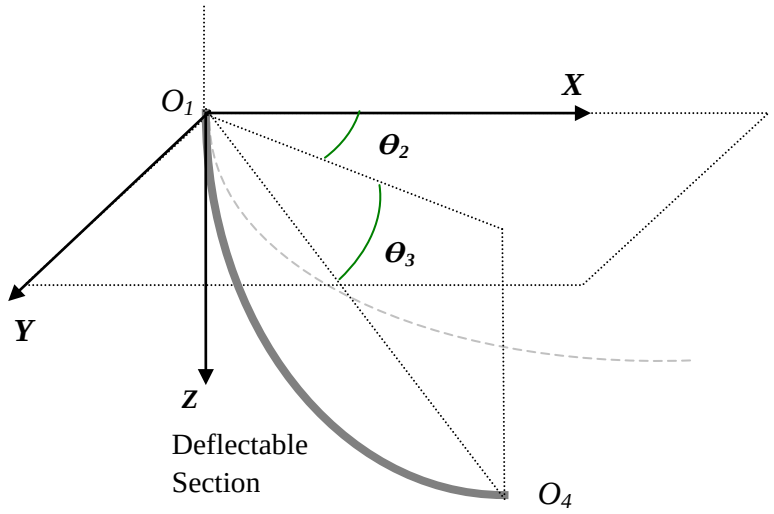

Figure 3.12: Catheter projection in O_1 coordinate frame.

rotation angle, e.g.,

$$\delta\theta_2 = \arccos(\ {}^A\vec{y_S}(t_1) \cdot\ {}^A\vec{y_S}(t_2)) \tag{3.4}$$

where ${}^A\vec{y_S}$ is the unit vector along the Y axis of S_1, calculated by converting unit vector ${}^S\vec{y_S} = (0,1,0)^T$ to Aurora® coordinate frame, as described in the subsequent section. Formula 3.4 yields the absolute value of $\delta\theta_2$. The sign of the twist angle is defined by the direction of actual twist operated at the handle.

Deflection angle

Measurement of the deflection angle can also be simplified cultivating the trigonometric relationships in figure 3.12. In this figure, the deflection angle can be found by projecting $\overrightarrow{O_1O_4}$ on the Z axis of S_1,

$$\theta_3 = \arcsin(\frac{{}^A\vec{z_S} \cdot \overrightarrow{O_1O_4}}{|\overrightarrow{O_1O_4}|}) \tag{3.5}$$

where $\overrightarrow{O_1O_4} = \vec{O_4} - \vec{O_1}$. Using formula 3.5, the differential deflection angle can be calculated as

$$\delta\theta_3 = \theta_3(t_2) - \theta_3(t_1). \tag{3.6}$$

Parameter estimation for task-space control

Differential joint parameters are calculated based on Aurora® sensor readings, as described in the preceding section. However the actual value of joint parameters (q_a) is not known yet. In other words, the actual values of translation d_1, twist angle θ_2 and deflection angle θ_3 are yet to be determined. The joint parameters are used in all Jacobian-based calculations and a successful navigation depends on the accurate estimation of the parameters.

One approach in finding model parameters is to integrate the differential values found previously. However integration is susceptible to measurement noise and inaccuracy and accumulates the noise offset in all measurement readings. In addition, the initial value of each parameter is not known for integration. A better approach is to find the best matching parameters of the model, i.e., find the model parameters that minimize the tip position estimation error. Using equation 2.2, the position estimated by the model is

$$p_m(d_1, \theta_2, \theta_3) = \begin{bmatrix} c\theta_2(\frac{L}{\frac{\pi}{2}-\theta_3}c{\theta_3}^2 + d_7 s2\theta_3) \\ s\theta_2(\frac{L}{\frac{\pi}{2}-\theta_3}c{\theta_3}^2 + d_7 s2\theta_3) \\ d_1 + \frac{L}{\pi-2\theta_3}s2\theta_3 - d_7 c2\theta_3 \end{bmatrix} \tag{3.7}$$

The task-space parameter estimation problem is formalized as follows:

$$q_a = \underset{d_1=0, 0\leq\theta_2<2\pi, -\pi\leq\theta_3\leq\pi}{\operatorname{argmin}} (p_a - p_m) \tag{3.8}$$

where $p_a = \overrightarrow{O_1O_6}$ is the actual position vector of the catheter tip in O_1 coordinate frame. The solution to this problem can be found by brute force search, spanning the whole parameter space with a given resolution step. However, task-space parameter estimation is a classical multi-variable optimization problem and can be solved using the methodologies available in the optimization literature. In CathNav, the problem is solved in two ways. In the initialization phase, to ensure finding the global minimum, the brute force search is utilized to find the best model parameters matching the configuration of the catheter. Despite the slower speed in finding the parameters, brute-force search is chosen because the solution is guaranteed to be found, the computation time is not a concern in initialization.

During the navigation, a three-dimensional Newton-Raphson iterative method [62] is utilized to find the instantaneous model parameters accurately. At each differential step, to find new model parameters, the optimization is localized about

the parameters found at the previous step. In other words, the problem is to find $q_a(t_2)$ using the parameters at the previous instant $q_a(t_1)$:

$$q_a = \text{argmin}(p_a(t_2) - p_m), \tag{3.9}$$

subject to

$$d_1 = 0,$$
$$|\theta_2(t_2) - \theta_2(t_1)| \leq |2\delta\theta_2(t_2)|,$$
$$|\theta_3(t_2) - \theta_3(t_1)| \leq |2\delta\theta_3(t_2)|.$$

The Newton-Raphson method was chosen due to its fast convergence properties and its usage of Jacobian inverse matrices which is already available in our system. Besides, the search is localized in solving (3.9) and the local and global minima in the localized variable ranges are likely the same or very close. In practice, this method reached the solution in less than 10 iterations. In the implementation, the minimization stops when a maximum number of iterations is reached or when any of the constraints are violated. In this case, the optimization might not have converged. An improvement to this technique is to use constrained minimization instead.

3.6.3 Coordinate Systems Conversion

One of the major tasks of CathNav software is to convert the coordinate frames of the devices in the system and the catheter model into a common framework. It also needs to establish a relationship between the actuation axes of the robotic system and the model parameters of the catheter. In this section the coordinate conversions and the rotation matrices involved are elaborated on. In all the coordinate conversions, a rotation matrix is found that converts a 3D vector in one coordinate frame to another coordinate frame. Aurora® field generator is assumed to be placed on the left side of the patient's torso, such that its field generator covers the rib cage volume, as shown in figure 3.2. Figure 3.13 illustrates all the coordinate frames used in the coordinate conversions.

User input conversion

The reference coordinate system is the Aurora® coordinate frame. The user has the option to enter the input commands using the 3D input device in the Aurora® coordinate system. From the user's perspective, the Aurora® and the Falcon operate in

similar coordinate frames. For instance, if Falcon grasp handle is moved upwards, it means that an upward motion (in $-X_A$ direction) in the Aurora® coordinate frame is commanded. For intuitive operation, the Falcon device is placed such that $Y_A \parallel X_F$. By default both devices are on flat even surfaces which means $X_A \parallel Y_F$. Based on the frames illustrated in figure 3.13, the rotation matrix converting the Falcon input to Aurora® coordinate frame, R_F^A, is constructed.

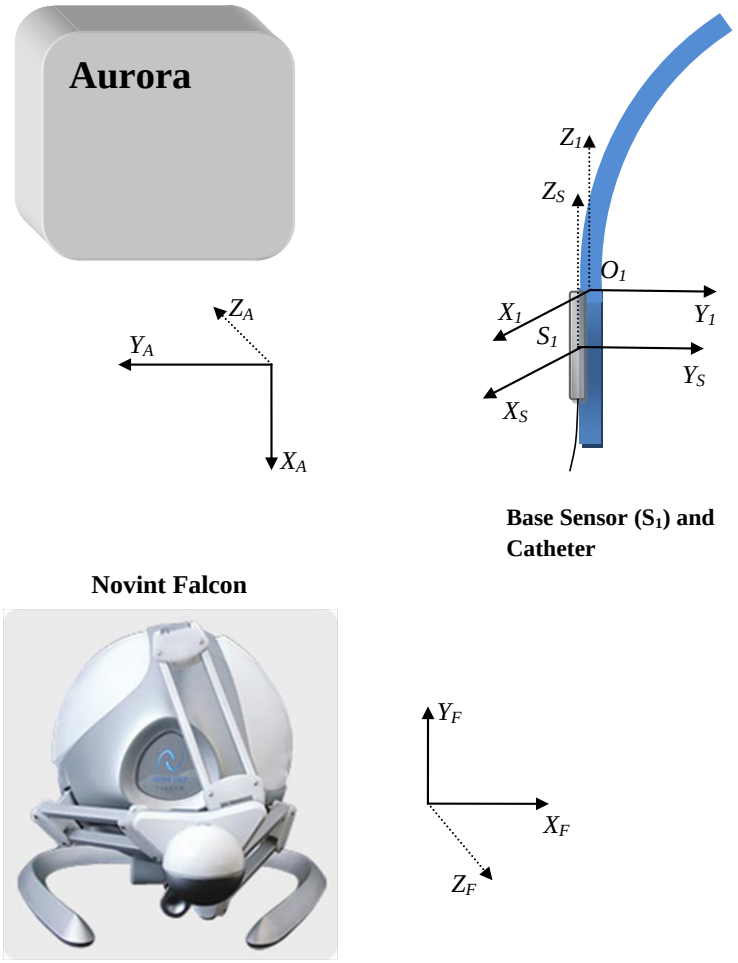

Figure 3.13: Coordinate frames of the navigation system, used in coordinate conversion (see also figure 3.2).

$$R_F^A = \begin{bmatrix} 0 & -1 & 0 \\ -1 & 0 & 0 \\ 0 & 0 & -1 \end{bmatrix} \tag{3.10}$$

With this scheme, the operator can direct the catheter so that by moving the device handle up or down, the catheter moves in posterior or anterior direction. Moving the handle left or right, moves the catheter in superior or inferior direction. Finally moving the handle toward or away from the device base moves the catheter tip laterally toward the left or the right side of the torso.

Sensor to model coordinate conversion

Establishing a relationship between the distal shaft model and the sensor readings is the critical function of CathNav that allows the modeling theory developed for the distal shaft to be applied in practice. If the coordinate frame of O_0 or its parallel frame O_1 (see figure 2.4) is found in the Aurora® coordinate system, the problem is solved.

For each sensor coil the position is known in Aurora® coordinate system. Sensor S_1 yields the position of O_1, as found through calibration algorithms. In addition, each sensor's orientation is known in the Aurora® coordinate system. Aurora® provides the orientation of the sensors in quaternion format. For a normalized quaternion $Q_i = (q_1, q_2, q_3, q_4)$ received for sensor S_i, the equivalent rotation matrix $R^A_{S_i}$ is calculated [63] by

$$R^A_{S_i} = \begin{bmatrix} 1-2(q_3^2+q_4^2) & 2(q_2q_3-q_1q_4) & 2(q_1q_3+q_2q_4) \\ 2(q_2q_3+q_1q_4) & 1-2(q_2^2+q_4^2) & 2(q_3q_4-q_1q_2) \\ 2(q_2q_4-q_1q_3) & 2(q_1q_2+q_3q_4) & 1-2(q_2^2+q3^2) \end{bmatrix} \tag{3.11}$$

The Z_1 axis of O_1 coordinate frame and Z_S axis of S_1 local frame are approximately parallel. It means that an offset twist angle θ_{2_0} could exist between the two coordinate frames. In other words, if O_1 coordinate frame is rotated about its Z_1 axis by the offset angle θ_{2_0}, it will correspond to the S_1 frame. Since the model coordinate frame is arbitrary in terms of its twist angle, we can assume both frames are the same, i.e., $\theta_{2_0} = 0$. This yields the principal relationship between the sensor S_1 and the model base coordinate frame,

$$R^A_{S_1} = R^A_{O_1} \tag{3.12}$$

Equation 3.12 is the important relationship that allows us to bring the modeling formulations in the realm of spatial measurements in a simplified way.

Target to model coordinate conversion

The position controller receives set points for the catheter position from the trajectory planner. The trajectory planner receives the target points in the Aurora® coordinate system from the user interface. The planned set points should be in the model coordinate system for the control to take place. In other words, $R_A^{O_1}$ is needed. Since rotation matrices constructed from unit quaternions belong to special orthogonal group SO(3), using (3.12), $R_A^{O_1}$ is found.

$$R_A^{O_1} = R_A^{S_1} = (R_{S_1}^A)^T \tag{3.13}$$

3.7 Control Method

The navigation strategy outlined in section 2.5 is implemented by CathNav utilizing a multi-threaded program design depicted in figure 3.8. The implemented control strategy is described in this section.

The system is composed of two major components, the robotic assistant and the catheter. The robotic assistant actuates the catheter and the catheter is modeled as a continuum manipulator and is operated by the robotic assistant. The three axes of robotic assistant are controlled by the VXM controllers that receive their set points from CathNav. This means low-level motor control is not a function implemented by CathNav. The remaining control functions including catheter handle control, joint-space control, task-space control and trajectory planning are all components of the navigation system.

It is noted that the catheter is an inherently bounded-input bounded-output (BIBO) stable system due the mechanics of actuation transfer from handle to the distal shaft. More specifically, the following constraints govern the actuation of the catheter.

- Any translation of catheter body cannot create a larger translation at the distal shaft, $d_{handle} \geq d_1$.
- The catheter cannot be twisted at the handle more than 540° by the manufacturer's specification. Any twisting action of catheter body cannot result in a larger twist at the distal shaft unless deformed by external forces. In other words, $\theta_{handle} \leq 540° \Rightarrow \theta_2 \leq 540°$.

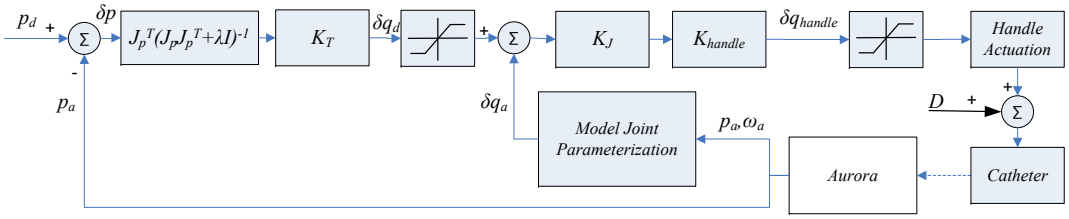

Figure 3.14: Cascaded structure of the controllers.

- Steering knob rotation is constrained, $-45° \leq \theta_{knob} \leq 45°$. The steering knob rotation results in constrained deflection angles at the distal shaft, $-180° \leq \theta_3 \leq 180°$.

For simplicity, and owing to the stability of the open-loop system, a proportional controller is used. A propotional-integral (PI) controller will be a better choice for steady-state tracking. It is noted that joint-space parameters are not measurable directly, and the distal shaft model provides an estimate of the kinematics of distal shaft motion. Consequently, errors are always present in joint-level calculations. Now, the control diagram 2.9 can be expanded in figure 3.14. In this diagram, the cascaded structure of task-space controller, joint-space controller, and handle actuation control is depicted. In the diagram, K_T is the task space controller gain, K_J denotes the proportional joint space controller, and K_{handle} is the handle actuation transfer gain, which can is calculated using the formulations in section 2.4.3. D denotes the disturbances affecting catheter's distal shaft as described in the next section. Both K_T and K_J gains are tuned experimentally using the well-established Ziegler-Nichols tuning rules [64]. K_J is first tuned such that joint-space controller achieves an acceptable performance. Once K_J is tuned, K_T is adjusted to achieve an acceptable task-space controller performance. For safety reasons, any overshoot in catheter positioning must be avoided, and hence high gains or high bandwidth are not recommended. This is to achieve a fail-safe control, as well.

3.8 Disturbance in Navigation

When the flexible catheter is put inside the cardiac chamber, it is subject to the cardiac contractions and relaxations, blood flow and pressure variations, and displacements of the rib cage due to respiration, and patient movement. Even when the catheter model can estimate the catheter position, the disturbances present inside the heart can undermine the position control.

It can be argued that both the sensors attached to the catheter undergo similar but not necessarily equal displacements and disturbances. This is particularly true for the displacements due to respiration and patient movement. As the relative position of the sensors ($\overrightarrow{O_1O_6}$ and $\overrightarrow{O_1O_4}$) is utilized in all calculations, such disturbances are assumed to be filtered out. In addition, a low-pass moving-average filter is utilized to remove the disturbances from the sensor readings. In-vivo experiments verify that this scheme leads to successful navigation.

3.9 High-level Navigation Algorithm

All the components of the navigation system, their inner mechanisms and how they interact with each other were covered so far in this chapter. The overall algorithm of the navigation system, and how the developed tools contribute to the navigation task, in line with the diagram in figure 2.11, is presented as follows.

Algorithm 3.4 High-level navigation algorithm

Require: Calibration vectors ${}^S\vec{v_1}$, ${}^S\vec{v_4}$ and ${}^S\vec{v_6}$ found through (3.1), (3.2) and algorithm 3.2 offline

Require: p_{target} from GUI/Falcon/Reference sensor

Require: $p_a = \overrightarrow{O_1O_6}$ calculated through algorithm 3.3

Require: q_a found through (3.8) and (3.9)

Require: $J_p(q_a)$ calculated by (2.12)

Construct the path to p_{target}
Divide the path into steps.
repeat
  p_d = next step on the path to target
  $---Task-space\ Control--$
  while $\tilde{p} > \epsilon_p$ **do**
    Calculate δq_d using (2.18) and K_T, task-space controller gain
    $---Joint-space\ Control--$
    repeat
      Calculate δq_a using (3.3), (3.4) and (3.6)
      Find $\delta q_{handle} = K_{handle} K_J (\delta q_d - \delta q_a)$
      Manipulate the catheter handle by δq_{handle} through robotic assistant
    until $(\delta q_d - \delta q_a) \leq \epsilon_q$
  end while
until $p_a \rightarrow p_{target}$

In algorithm 3.4, ϵ_p and ϵ_q are task-space and joint-space position error thresholds.

3.10 Conclusion

In this chapter, the specifics of the developed navigation platform were presented. The system components including robotic assistant, position tracking, 3D input device, and navigation software were explained. The design philosophy of the navigation software and its features were also reviewed. The rotation matrices to convert the coordinate systems of tracking, 3D input and the distal shaft model to each other were found. How the virtual joint parameters are estimated for joint-space and task-space control were described. The calibration procedures for Aurora® tracking was also presented. Finally, the control method was revisited.

The theoretical and practical aspects of the navigation system have been covered so far. In the following chapters, the experiments conducted to validate the catheter modeling are described. The results will demonstrate the applicability of the modeling for navigation. In-vivo experiments will also verify that catheter navigation can be accomplished through the system.

Chapter 4

Catheter Model Validation: In-vitro[1]

4.1 Static Model Validation

To demonstrate the validity of curvature constancy and zero torsion assumptions in distal shaft deflection, a measurement fixture was constructed. The catheter handle was mounted on the fixture. Through a simple pulley and weight mechanism, a known force was exerted on the steering knob of the catheter which, in turn, resulted in a known tension force in the pull wire. By exertion of the force, the steering knob was turned until it reached an equilibrium angle. The catheter was threaded through a PVC flexible tubing fixed on a V-shaped support. The catheter body lay straight inside the tubing, virtually eliminating the internal friction between the pull-wires and the catheter's lumen. The deflectable section of the catheter was left unsupported out of the tubing in the air. With this setup, it could be assumed that the pull-wire tension force at the knob was the same throughout the catheter body and in the distal shaft. A picture of the fixture is presented in figure 4.1.

Using the fixture, the approximate pull-wire tension was measured. Having the pull-wire tension force, the flexural rigidity (EI), and curvature of the distal shaft was calculated, as outlined in experimental curvature calculation algorithm in section 2.3.3. Subsequently, a chain algorithm [50] was applied to numerically calculate the end position of the catheter tip given the end-moment load and the flexural rigidity. For each load, the measurements were replicated 20 times. The calculated end position was compared with the position vectors recorded with the Aurora®

[1]This chapter is partly published in [42, 44].

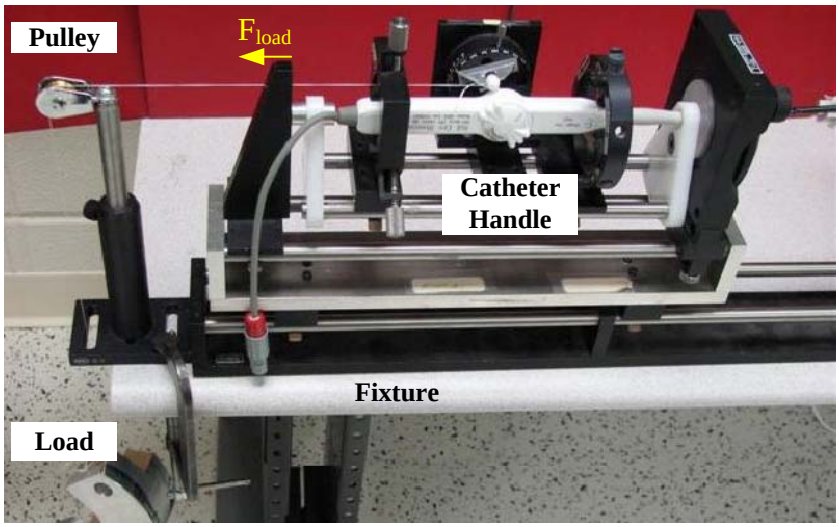

Figure 4.1: The fixture for static experiments. The catheter handle is mounted on the fixture and a load is applied to the steering knob.

system and the validity of the modeling was verified. Figure 4.2(a) demonstrates the distal shaft shape in response to various wire tensions. The end position of the catheter tip is compared with the measured position in figure 4.2(b). The overall root mean square (RMS) error values are 0.41 mm and 0.08 mm along X and Y axes respectively. The standard deviation of error values are 1.49 mm and 0.34 mm, respectively.

Although an approximate approach combining pseudo-rigid modeling with the chain algorithm was utilized to model the statics of catheter bending, the error figures and the precision of end position profile estimates in figure 4.2(b) clearly establish the foundation of the kinematic modeling. In other words, the catheter bends with constant curvature in a single plane in the absence of external loads. Consequently, the validity of the kinematic model can be comprehensively verified and validated as elaborated in the subsequent sections.

4.2 Kinematic Model Verification

To test the verifiability of the kinematic model, the catheter fixture used in the static experiments was replaced by the robotic assistant. The kinematic model was tested when the distal shaft was under no external load and was supported free in the air. The position vector (2.2) reveals that the twisting of the catheter

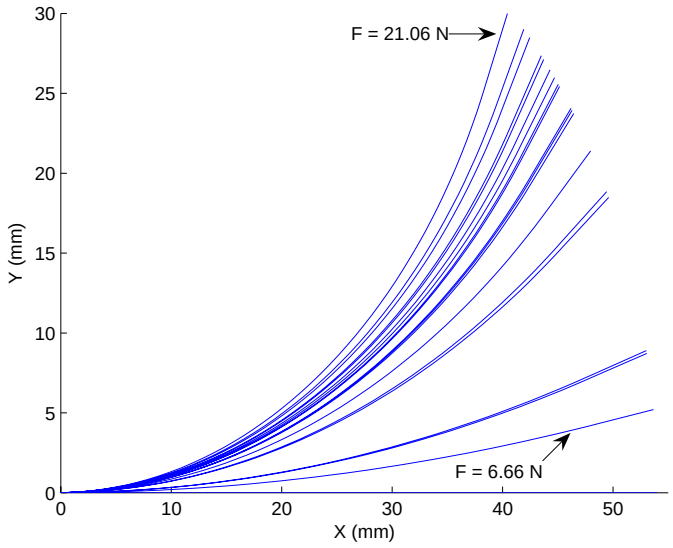

(a)

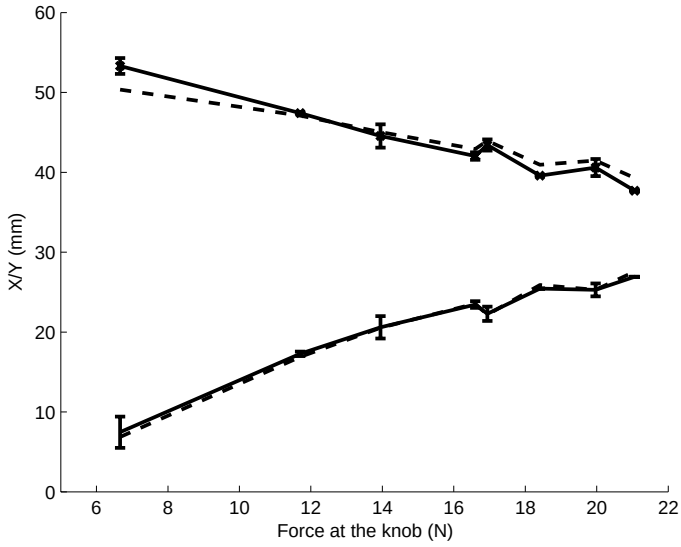

(b)

Figure 4.2: Modeling of distal shaft deflection statics (a) The distal shaft deflection in response to various pull-wire forces as predicted by the static model. The bending section length (L) is 50 mm and the distal end length (d_7) is 5 mm. (b) Measured position coordinates (solid line) along with static model estimates (dashed line) when different forces are applied to the steering knob.

(θ_2) and the deflection of the bending segment (θ_3) are expected to be decoupled motions. As a result, the contributions of each parameter to the position of the catheter tip can be studied independently of the other parameter. It is noted that this decoupling is based on the assumption that no external load is applied to the catheter, and the effect of gravity is negligible. After the relationship between the input actuation and the resultant bending or rotation is investigated, the accuracy of the formulations in predicting the position of catheter tip is evaluated. Due to the built-in symmetry in both the twisting and deflection, only the positive angles were examined.

- *Twist (θ_2)* - To examine the linear relationship (2.25) between twist angles at the handle and at the distal shaft base (O_1 in figure 2.4), the robotic assistant was programmed to twist the catheter by different angles both forwards and backwards. Figure 4.3(a) depicts the average of the measured (found by integrating (3.4)) and estimated (using (2.25) twist angles in a 180° rotation, when the deflection angle is constant at 60°. The average was calculated for 16 back and forth rotations. The linearity of the twist angle relationship is visible in the figure. Least-square line fitting reveals that slope (k_2) and the backlash (B_2) are the same for both directions. The root mean square error (RMSE) in the linear approximation is 0.74° and 0.37° in each direction respectively.

- *Deflection (θ_3)* - To measure the deflection, the catheter was positioned so that the bending plane lay vertical. The steering knob was rotated at various angles, and the pose of the bending section ends were recorded ($O1$ and $O4$ in figure 2.4). The estimated (using (2.23)) and averaged measured (using (3.5)) angles for a 40° rotation, when twist angle remains at 75°, are sketched in figure 4.3(b). The average was calculated over 10 back and forth rotations. The RMSE of the lines fitted for knob angle $> 10°$ are 1.252° and 0.80° in forward and backward directions respectively. Knob angles below 10° fall in the dead-zone of the knob, i.e., $\theta_0 \cong 10°$ in (2.23).

The hysteresis in back and forth motions is clearly visible in figure 4.3. In addition to the linear relationship between the input and output angles in each direction, the position of the bending segment tip (O_4 in figure 2.4) was also examined. Sample position profiles are presented in figure 4.4 where either the twist or the deflection is changed. The corresponding error values in Table 4.1 indicate that the model provides an acceptable estimation of the geometry that governs the

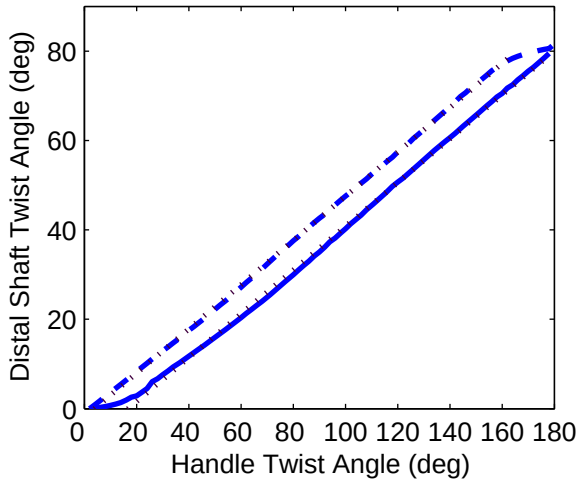

(a)

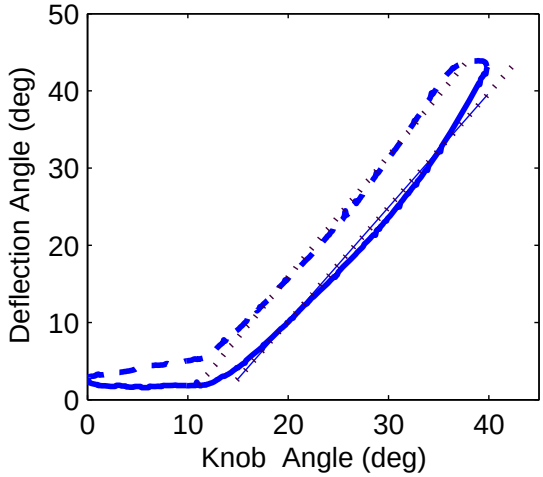

(b)

Figure 4.3: Catheter twist and deflection angles. Forward motion is sketched by solid line, backward motion by dashed line, and the fitted line by dotted pattern. (a) Catheter twist (θ_2) vs. handle twist. (b) Catheter deflection (θ_3) vs. knob rotation.

Table 4.1: Error values in the position calculations (RMSE±standard deviation)

Parameter	X (mm)	Y (mm)	Z (mm)
Twist(θ_2)	0.45±0.39	0.44±0.44	1.24±1.00
Deflection(θ_3)	1.41±0.85	0.44±0.35	0.48±0.26

motion of the catheter. An out-of-plane bending is visible in the Z profile in figure 4.4(a). Since Z is not a function of the knob angle, the estimated position does not change when the knob is not rotated, and the out-of-plane bending cannot be predicted by the model. It is noteworthy that the range of this deviation is small (less than 3 mm), compared to the distal shaft diameter (4 mm).

The decoupled motion test results verify that the model is capable of estimating catheter position despite the existence of actuation hysteresis and nonlinearities. Consequently, the validity of modeling can be investigated rigorously under more realistic conditions. The validation experiments and their results are provided in the next section.

4.3 Kinematic Model Validation

4.3.1 Experimental Setup

To verify the robustness of the model in conditions similar to that of the human body, a phantom that mimics cardiovascular anatomy and dynamics of heart beating is desired. There is no dynamic phantom available in the market, construction of a realistic dynamic phantom is a challenging task. Appendix B provides the specifications and guidelines for construction of such a phantom. Due to technical difficulties in design and construction of a dynamic phantom, a static phantom was designed and constructed to mimic the path the catheter takes inside the body and to emulate the intracardiac pressure levels.

The anterograde approach to reach the right side of the heart was chosen. The dimensions and orientations of the veins on the path, namely, right femoral vein (FV), right external iliac vein (EIV), right common iliac vein (CIV), and inferior vena cava (IVC) were taken from a middle-aged male patient's torso CT scan. The cross-sections of all the vessels were assumed to be elliptical. A series of clear flexible PVC tubes was assembled to emulate the vessels. The length, diameter, and orientation of the tubing sections were based on the CT measurements and

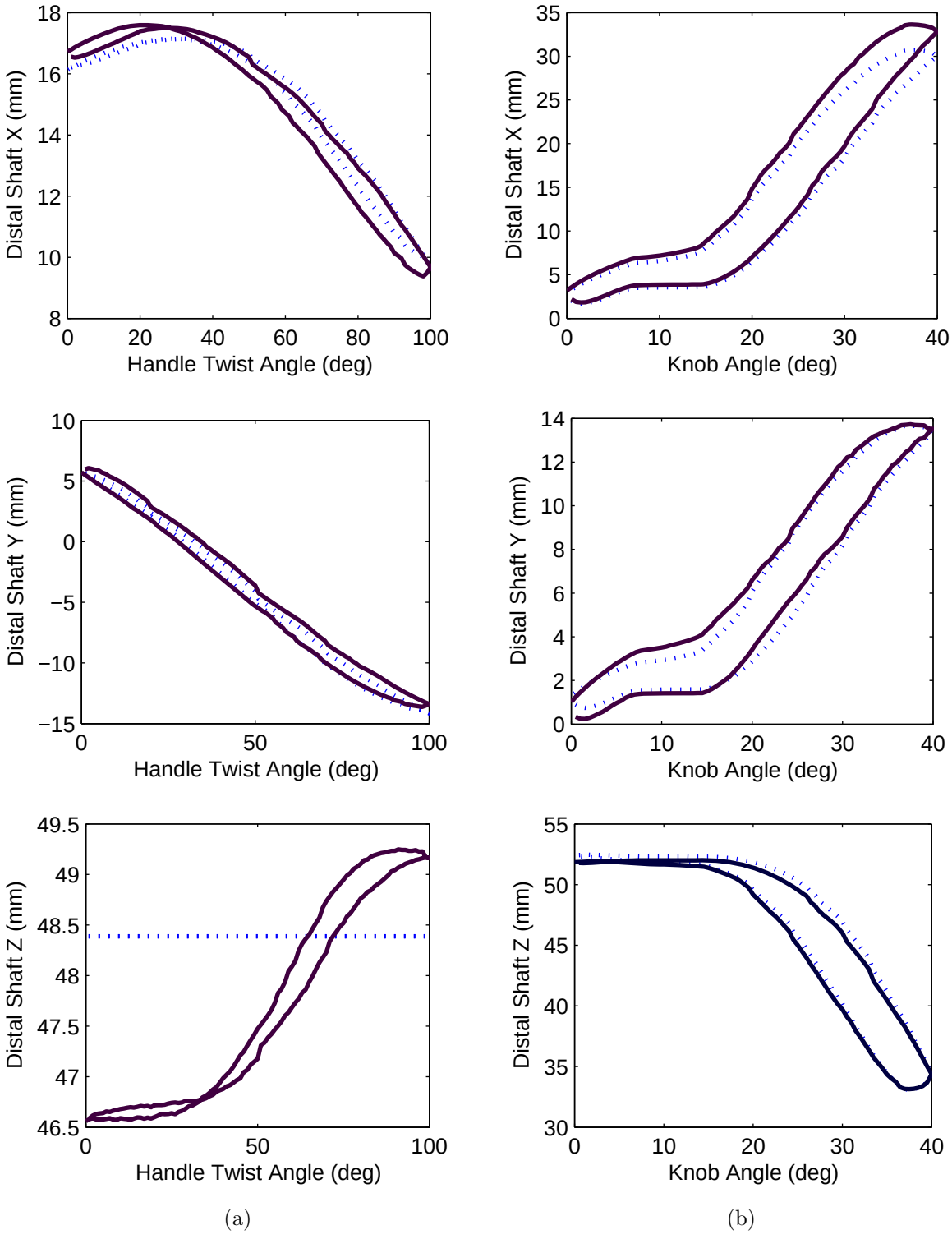

(a) (b)

Figure 4.4: Estimated (dotted line) and measured position profiles (solid line) of the deflectable section end, when (a) the handle is twisted 100 degrees back and forth, and (b) steering knob is rotated 40 degrees back and forth.

are provided in appendix B . The tubes ended in a container that represented the heart. Figure 4.5 illustrates the phantom structure. From the insertion point at the femoral vein, the tubing extended into a second container. Both containers had a diameter of 100 mm.

In this phantom, water was used to mimic blood, and to create intracardiac pressure levels. The container held a water column that exerted the required hydrostatic pressure on the distal shaft of the catheter. The catheter was passed through the emulated path into the container, and water exerted pressure on the distal shaft near the bottom of the container. As the catheter was bent and twisted, the distance of the distal tip from the surface of the water in the container changed. As a result, the hydrostatic pressure on the distal shaft changed due to the variation of the water column height above the distal shaft. The actual pressure on the shaft was the combined pressure of the water column and atmospheric pressure. All the kinematic experiments were replicated under the following pressure levels created by the water column in the container (1 mmHg equals 13 mm Water):

- 0 to 10 mmHg
- 10 to 20 mmHg
- 20 to 30 mmHg

The above levels were chosen to mimic the pressure levels in cardiac chambers. The actual pressure values are 0–25 mmHg in the right ventricle (RV), 0–6 mmHg in the right atrium (RA), 0–120 mmHg in the left ventricle (LV), and 0–10 mmHg in the left atrium (LA) [65]. Due to the limitations in the height of the containers, pressure levels above 30 mmHg were not generated. As a result, pressure levels in all cardiac chambers except LV were covered in the experiments. The fact that most ablation therapies deal with RA, RV, and LA justifies this limitation.

4.3.2 Results

Four sets of experiments were designed to validate the kinematic modeling. In the designed kinematic experiments, the catheter end position was measured in response to variations in joint parameters, and the capability of the model to correctly predict the position was investigated. Given the 4 mm diameter of the catheter tip, if the model predicts the position of the catheter within the distance of the tip radius, or 2 mm, it is clinically acceptable. Each experiment was replicated 20

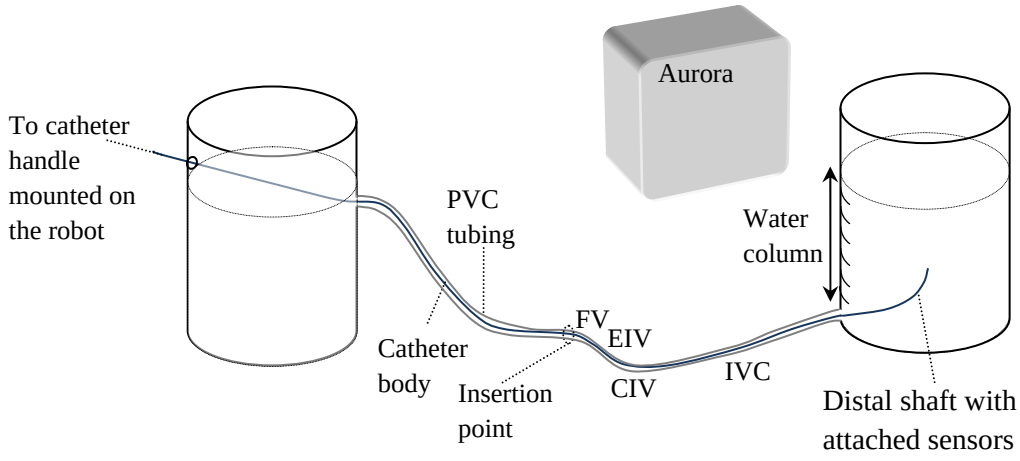

(a)

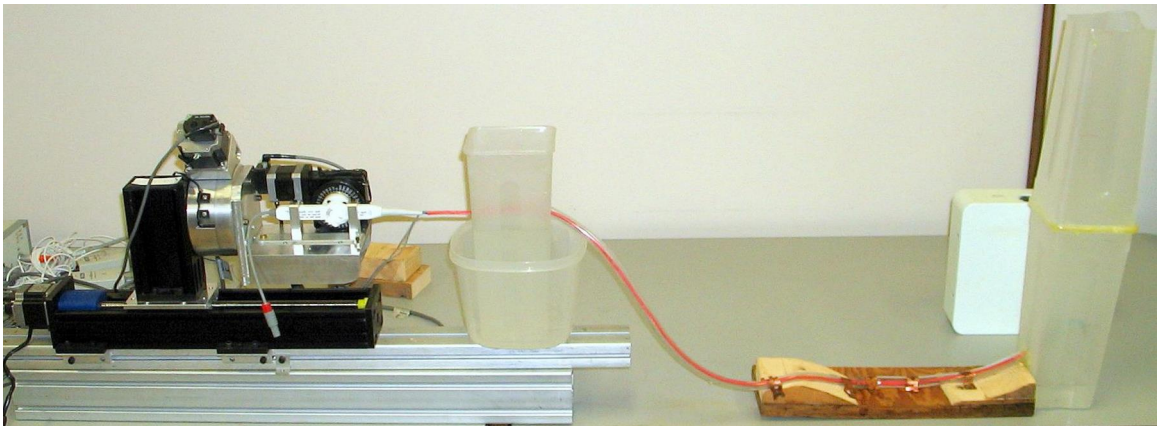

(b)

Figure 4.5: Static heart phantom. (a) The schematic of the phantom. The vessels constituting the catheter path include femoral vain (FV), external iliac vein (EIV), common iliac vein (CIV), and inferior vena cava (IVC). The Aurora® electromagnetic field generator is depicted beside the container that holds the distal shaft. (b) Actual setup. The robot, phantom and Aurora® field generator are shown.

times for statistical soundness and further analysis. In each experiment, some parameters were changed within a given range. In each iteration, the parameters at the handle started and ended at the same values. Model parameters were found through equations (3.3), (3.4) and (3.5). Position measurements were taken from Aurora®sensors attached to the distal shaft.

In each experiment, a Chi-square test was used to verify the goodness of fit (GOF) of the model in terms of position vector of the catheter tip $\vec{O_6}$ in base sensor (S_1) coordinate frame. For each experiment to follow, a table of various statistical measures, including the Chi-square test, is provided that reflects the performance of the modeling. The significance level α was chosen to be 1% in all the experiments. In the tables to follow, MAE, RMSE, SD, and r^2 denote mean absolute error, root mean square error, standard deviation, and the coefficient of determination respectively. Repeatability index was computed by the formula MAE+3 SD [66]. All the measurements were in mm.

To demonstrate the goodness of fit more intuitively, the linear regression between the data and model was also considered. The 99% confidence intervals for the slope β_1 and the intercept β_0 were calculated and are presented in the tables. When the slope confidence interval includes 1 and the intercept confidence interval includes 0, the linear relationship between the model and the measured position is unbiased; otherwise, there is a bias in the model's position estimates.

For each experiment, the Cartesian distance between the predicted position of the catheter tip and measured position is also presented. The validity of curvature constancy assumption in the coupling of parameter d_4 with deflection angle θ_3 in (2.11) was also investigated. The description of each experiment along with the results follows.

Twist Angle θ_2

The catheter was twisted about its centre line up to 360 degrees in both directions. Only the parameter θ_2 in (2.2) was updated and all other parameters were assumed constant in the experiments. The measurements of distal shaft end positions (using Aurora® sensors attached to O_1 and O_4 in figure 2.4) were performed at 5 degree twist steps yielding 144 statistical degrees of freedom (DOFs) in back and forth rotations. Based on the sensor readings in Aurora coordinate frame, the distal shaft twist angle was found using (3.4). Tables 4.2 and 4.3 summarize the results.

The GOF test is clearly significant. The linear relationship is also significant,

i.e., $\beta_1 = 0$ is rejected. The curvature constancy assumption is valid as the d_4 error is small. However as the pressure level is raised, the error figures rise, the repeatability worsens and the linear relationship between the data and the model becomes more biased. In table 4.3, the X component of position vector is affected most by the pressure. A similar phenomenon will be observed in the deflection experiments. Although the deflection angle is constant, the curvature constancy error (d_4) increases with pressure, which indicates the deformation of the catheter under higher pressure levels. This trend indicates the limited ability of the model to predict the position in higher pressures when the deflection angle (θ_3) and translation (d_1) are assumed constant.

Table 4.2: Cartesian distance between the estimated and modeled position along with curvature constancy error in twist angle experiments.

Pressure level	Position error (mm)	d_4 error (mm)
0-10 mmHg	0.25±0.11	0.22±0.13
10-20 mmHg	0.74±0.25	0.67±0.33
20-30 mmHg	2.23±1.53	2.1±1.46

Deflection Angle θ_3

In this experiment, the distal shaft was deflected using the steering knob in the handle. The knob was turned from the straight position up to 45 degrees, which resulted in maximum deflection at the distal shaft. Only the parameter θ_3 in (2.2) was updated and all other parameters were assumed constant in the experiments. Measurements of distal shaft end positions (using Aurora® sensors attached to O_1 and O_4 in figure 2.4) were performed at 1 degree deflection steps yielding 90 statistical DOFs in back and forth rotations. Based on the sensor readings in Aurora coordinate frame, the distal shaft twist angle was found using (3.5). Tables 4.4 and 4.5 summarize the results.

The GOF measure is generally significant except for the X coordinate in pressures above 10 mmHg. The linear relationship is also significant. Even when the GOF is rejected, the coefficient of determination remains above 95%. From the tables, we can conclude that as the pressure is increased, the pressure gradient forces an out-of-plane deflection in the distal shaft, which results in losing goodness of fit and repeatability, especially in the X component of the position vector. If the twist angle θ_2 is changed during deflection, the pressure forces acting on the shaft change and the error figures change, as demonstrated in the next subsection. Compared

Table 4.3: Twist angle analysis.

Pressure (mmHg)	Dimension	χ^2 statistic (quantile=186.4)	MAE (mm)	RMSE±SD (mm)	r^2	Confidence Intervals		Repeatability Index
						β_1 CI	β_0 CI	
0	X	7.48	0.067	0.079±0.041	0.999	[1.06,1.08]	[0.84,1.08]	0.19
to	Y	58.70	0.116	0.132±0.063	1	[1.00,1.00]	[0.05,0.16]	0.304
10	Z	16.11	0.139	0.178±0.112	1	[0.99,1.00]	[-0.09,-0.26]	0.47
10	X	19.32	0.349	0.431±0.432	0.998	[0.99,1.00]	[-0.17,0.40]	1.645
to	Y	26.33	0.328	0.397±0.398	1.000	[1.00,1.00]	[-0.07,0.12]	1.521
20	Z	3.36	0.24	0.312±0.312	0.999	[0.99,1.00]	[-0.01,0.12]	1.176
20	X	16.098	1.074	1.473±1.415	0.667	[2,2.73]	[-4.12,-7.46]	5.319
to	Y	72.62	0.879	1.139±1.11	0.984	[1.25,1.32]	[5.78,7,37]	4.22
30	Z	2.58	0.726	1.196±1.086	0.992	[0.82,0.86]	[-0.97,-0.63]	3.982

to twist angle experiments, the error does not increase as significantly with higher pressure levels. Both experiments exhibit a larger error value in the X component of the position vector, under higher pressures.

Table 4.4: Cartesian distance between the estimated and modeled position along with curvature constancy error in deflection angle experiments.

Pressure level	Position error (mm)	d_4 error (mm)
0-10 mmHg	0.77±0.42	0.71±0.36
10-20 mmHg	1.42±0.86	0.44±0.26
20-30 mmHg	2.04±1.08	0.41±0.23

Combined Deflection and Twist

In this experiment, the steering knob was turned up to 36 degrees and the catheter was twisted up to 360 degrees, in parallel. A linear and a sinusoidal trajectory, each with 20 replications, were traversed at the handle. Only translation d_1 was fixed at zero. For linear trajectory, the twist or deflection angle was increased in linear steps up to 360 (twist) or 36 (deflection) degrees and then decreased back to zero. In sinusoidal trajectory, the increments/decrements follow a sinusoide whose peak is at 360 (twist) or 36 degrees (deflection). The measurement samples of distal shaft end positions (O_1 and O_4 in figure 2.4) had 72 statistical DOFs in back and forth rotations. Tables 4.6 and 4.7 present the outcomes.

The GOF of position vector coordinates is significant except for one instance (Z under 0 to 10 mmHg pressure). Compared to the results in the one-DOF experiments, the error figures fall within the same range, and even under the highest pressure the repeatability is below the designated threshold of 2 mm. In addition, the consistently strong correlation and linearity between the model and the measured position vectors indicate the success of the modeling.

Compared to decoupled twist and deflection experiments, the modeling error is not significantly different, but the GOF has improved and the X component errors are not present. The model shows better resilience in higher pressure levels. It can be concluded that model parameter estimation produces reliable estimates in combined motion as well as the decoupled motion.

Table 4.5: Deflection angle analysis.

Pressure (mmHg)	Dimension	χ^2 statistic (quantile=124.1)	MAE (mm)	RMSE±SD (mm)	r^2	Confidence Intervals		Repeatability Index
						β_1 CI	β_0 CI	
0	X	41.11	0.482	0.579±0.32	0.998	[0.99,1.01]	[-0.5,0.55]	2.22
to	Y	17.45	0.275	0.36±0.23	0.999	[1, 1.01]	[-0.15,0.23]	1.36
10	Z	13.26	0.154	0.183±0.09	0.995	[0.99,1.03]	[-0.32,-0.16]	0.7
10	X	425.27	0.948	1.25±0.82	0.987	[0.57,0.61]	[-1.30,-1.09]	3.42
to	Y	51.40	0.352	0.51±0.36	0.999	[1.02,1.04]	[0.25,0.70]	1.45
20	Z	33.17	0.259	0.32±0.19	0.996	[0.96,1.00]	[-1.75,-0.16]	0.84
20	X	628.21	1.55	1.90±1.11	0.968	[0.55,0.61]	[1.72,2.24]	4.88
to	Y	38.48	0.39	0.50±0.32	0.999	[1.25,1.32]	[5.78,7,37]	1.34
30	Z	1.25	0.19	0.229±0.13	1	[0.82,0.86]	[-0.97,-0.63]	0.59

Table 4.6: Cartesian distance between the estimated and modeled position along with curvature constancy error in combined deflection and twist experiments.

Pressure level	Position error (mm)	d_4 error (mm)
0-10 mmHg	1.46±1.015	1.17±1.00
10-20 mmHg	2.66±1.96	2.16±1.82
20-30 mmHg	0.78±0.60	0.54±0.46

Full Motion

In this experiment, all three DOFs were actuated. The knob was turned up to the maximum of 40 degrees. The catheter was twisted at the same time up to the maximum of 400 degrees. The catheter was also translated up to the maximum of 50 mm. A linear and a sinusoidal trajectory, each with 20 replications, were traversed at the handle for all the three parameters. For linear trajectory, the twist/deflection/translation parameter was increased in linear steps up to its designated maximum and then decreased back to zero. In sinusoidal trajectory, the increments/decrements followed a sinusoide whose peak is at the designated maximum. The measurement samples of distal shaft end positions (O_1 and O_4 in figure 2.4) had statistical 80 DOFs in back and forth motion. Tables 4.8 and 4.9 present the results.

The tables clearly reflect the power of the model. The GOF is significant except for two instances, and the linear relationship is significant. The coefficient of determination is almost 1 and the error values are small. This set of experiments verifies that the kinematic model is capable of estimating the position of the catheter with acceptable precision even when all the three DOFs are actuated simultaneously. In fact, inclusion of all the model parameter changes yields less error and provides more credible position estimates.

Table 4.7: Combined deflection and twist analysis.

Pressure (mmHg)	Dimension	χ^2 statistic (quantile=102.8)	MAE (mm)	RMSE±SD (mm)	r^2	Confidence Intervals		Repeatability Index
						β_1 CI	β_0 CI	
0	X	63.24	0.81	1.06±0.68	1.00	[1.01,1.02]	[-0.92,-0.60]	2.84
to	Y	9.95	0.25	0.45±0.37	0.999	[1.00, 1.02]	[-0.03,0.15]	1.37
10	Z	184.58	0.79	1.16±0.79	1.00	[1.01,1.02]	[0.19,0.55]	3.16
10	X	29.60	0.86	1.38±1.08	0.998	[0.98,1.00]	[-1.31,-0.66]	4.12
to	Y	28.23	0.36	0.48±0.32	0.999	[0.99,1.01]	[0.02,0.33]	1.32
20	Z	50.13	0.91	1.59±1.30	0.993	[1.04,1.08]	[-1.02,0.00]	4.83
20	X	36.01	0.28	0.39±0.27	1.00	[0.99,1.00]	[0.02,0.19]	1.09
to	Y	1.47	0.18	0.37±0.33	0.99	[1.01,1.02]	[-0.15,-0.01]	1.18
30	Z	1.29	0.15	0.27±0.23	1.00	[1.00,1.01]	[-0.24,-0.13]	0.84

Table 4.8: Cartesian distance between the estimated and modeled position along with curvature constancy error in full motion experiments.

Pressure level	Position error (mm)	d_4 error (mm)
0-10 mmHg	1.24±1.18	2.89±2.48
10-20 mmHg	1.50±1.42	3.13±2.71
20-30 mmHg	0.28±0.23	0.77±0.61

4.4 Concluding Remarks

The kinematic model's performance in the prediction of the catheter tip position was shown to be reasonably accurate in the experiments. The assumption of curvature constancy and single-plane deflection were verified through the kinematic experiments. The two assumptions were also confirmed by the approximation of bending statics using pseudo-rigid modeling in the absence of external loads.

It is noted that in all the experiments, the sensors attached to the catheter's distal shaft affect the catheter's deflection. In fact, they affect the geometrical symmetry of the distal shaft and add to the flexural rigidity of the shaft. This means the full range of catheter deflection might not be achieved when the sensors are attached. The only way to alleviate the effect of sensors on the catheter motion, is to track the catheter position by stereo vision, which is not feasible when testing in phantom or in-vivo. Moreover, to track the catheter in-vivo, the electromagnetic tracking seems to be the only practical choice for real-time position control.

As the catheter lies inside its vascular path to the heart, the contact friction between the catheter body and the luminal structure of blood vessels, and the flexibility of the catheter body result in the hysteresis phenomenon in actuation. The hysteresis occurs mainly in the transfer of the actuations from the handle to the twist/deflection/displacement actions at the distal shaft. This means, the relationship between an actuation parameter at the handle and the same parameter at the distal shaft is non-linear. This also means that the forward and backward actuation at the handle results in different curves at the distal shaft. The hysteresis in modeling the distal shaft (relating the motion of the distal-shaft base to its tip motion) is negligible when compared to the whole catheter. That is why we argue that the hysteresis does not affect the modeling but is an issue in applying the model to control the tip position through handle actuation, as the model deals with the configuration of the distal shaft and not the translation of motion from the handle to the distal shaft.

Table 4.9: Full motion analysis.

Pressure (mmHg)	Dimension	χ^2 statistic (quantile=112.33)	MAE (mm)	RMSE±SD (mm)	r^2	Confidence Intervals		Repeatability Index
						β_1 CI	β_0 CI	
0	X	57.9	0.38	1.22±1.16	0.99	[1.01,1.02]	[-0.72,-0.27]	3.88
to	Y	84.39	0.069	0.2±0.18	0.99	[1.00, 1.01]	[0.03,0.11]	0.64
10	Z	0.12	0.012	0.06±0.05	1.00	[1.00,1.00]	[-0.04,0.00]	0.18
10	X	304.09	0.47	1.46±1.39	0.98	[0.97,1.02]	[-1.84,0.22]	2.81
to	Y	86.11	0.12	0.33±0.32	0.98	[0.98,1.04]	[-0.18,0.26]	1.07
20	Z	0.12	0.017	0.08±0.08	1.00	[1.00,1.00]	[-0.06,-0.01]	0.13
20	X	79.55	0.09	0.21±0.18	1.00	[1.00,1.00]	[0.07,0.15]	0.66
to	Y	208.96	0.05	0.12±0.11	1.00	[1.01,1.00]	[-0.04,0.01]	0.37
30	Z	8.17	0.05	0.10±0.087	1.00	[1.00,1.01]	[-0.04,0.03]	0.32

A discussion of the loads and forces acting on the catheter inside the cardiac chambers is in order. The pseudo-static pressure levels created by the phantom are an approximation of the intracardiac pressure dynamics. The blood pressure dynamics and the turbulent blood flow, due to the non-Newtonian nature of blood, can undermine the performance of the model. However, based on the results, the precision of the modeling is acceptable, and the model conforms with the instantaneous catheter configuration. In addition, as the speed of the catheter manipulation in a clinical setting is very low compared to the heart's beating frequency (1–2 Hz), if the modeling and manipulation are synchronized with the heart rate, an acceptable modeling precision is expected when the catheter is not deformed due to contact forces. The laminated internal structure of the catheter dampens the vibrations that could be induced by the dynamics as well. It can be concluded that the proposed model is appropriate for free motion modeling in gross positioning of the catheter in the neighbourhood of target points on the endocardium.

In the next chapter, the performance of navigation as well as modeling is studied through experiments on beating heart. It will be demonstrated that the modeling is valid and the navigation is feasible in vivo.

Chapter 5

Navigation Validation: In-vivo[1]

5.1 Experimental Setup

To study the feasibility of the application of the system in actual interventions, the system was tested and validated on three porcine subjects in the research vivarium in St. Michael's Hospital in Toronto, Ontario, Canada. Porcine subjects were utilized due to their long established tradition as a viable model for testing human intracardiac devices. Swines are similar in size, anatomy and physiology to human making them ideal candidates for human intracardiac catheterization. The experiment protocol was approved by the hospital's Animal Care And Use Committee, in accordance with Canadian Council On Animal Care guidelines. The experiment procedure details are provided in appendix C.

Each subject was sedated with a cocktail of Xylazine (2mg/kg), Ketamine (20mg/ml) and one ampoule of Atropine (0.6 mg/ml). After 15 minutes, the swine was immobilized, allowing for it to be weighed and transferred to the pre-op room. Then it was masked with a gas inhalant of isofluorane at 5%. A 22G angiocatheter was placed in the ear and IV fluids (0.9ml NaCl) was started on a slow drip. The subject was then placed in dorsal recumbency and intubated for artificial respiration. After intubation, it was transferred to the operating room and ECG electrodes were attached for monitoring the electrocardiogram. During the procedure, the subject was maintained on 2.5% - 3% isofluorane. A femoral venous cutdown was done on both hind limbs, as well as a jugular cutdown on the neck. After the procedure, the swine was euthanized with a lethal intravenous (IV) injection of sodium pentobarbital (540mg/ml).

[1]This chapter is partly published in [43].

SteeroCath-T (BostonScientific, Natick, MA) was used to build the catheter assembly, described in section 3.3. The catheter assembly was deployed on the robotic assistant and was inserted through a 22F introducer sheath (Cook Medical Inc., Bloomington, IN) into the right femoral vein and was threaded into the right atrium (RA). The catheter assembly was introduced into RA manually prior to being mounted on the robot. The Aurora® field generator was placed beside the swine chest so that the distal shaft of the catheter (with two attached Aurora® sensors) in the RA could be tracked within the Aurora's measurement volume. A third Aurora® sensor was introduced through the left jugular vein and threaded into the RA as well. This sensor could be positioned at desired landmarks in RA. The sensor position was the target of the navigation experiments. This sensor will be referred to as the reference sensor henceforward. At every instant, the distance vector between the catheter assembly tip and the reference sensor was presented through the software UI to assist the operator in controlling the catheter position. As the reference sensor is very flexible compared to the catheter, it is swayed by cardiac contractions. To filter the cyclic noise in the distance vector, it is passed through a moving average filter [67], before it is fed to the trajectory planner. The moving average filter had an adjustable window size with default value of 15.

The operation was monitored under fluoroscopy (OEC Series 9800 cardiac mobile C-Arm, GE Healthcare Technologies, Waukesha, WI). For better visualization of the navigation process, intracardiac echocardiography (ICE) was used as well. An ICE catheter (Acuson AcuNav, Siemens AG Medical Solutions, Erlangen, Germany) was introduced through the left femoral vein into the RA. ICE images provided a better view of where the catheter assembly and the reference sensor were positioned relative to the intra-atrial anatomy. Figures 5.1 and 5.2 illustrate the actual setup in the operating room.

5.2 Kinematic Model Validation

In order to verify that the distal shaft model can match the reality of distal shaft shape, two scenarios were implemented and tested on the animals. In each scenario, the catheter went through a pre-programmed motion and its position profile measured with Aurora® sensors was recorded. The model parameters were found and the model's position vector (2.2) was compared with the actual position measurements for distal shaft tip (O_6 in figure 2.4). Model parameters were found through task space parameter estimation, as described in section 3.6.2. The differ-

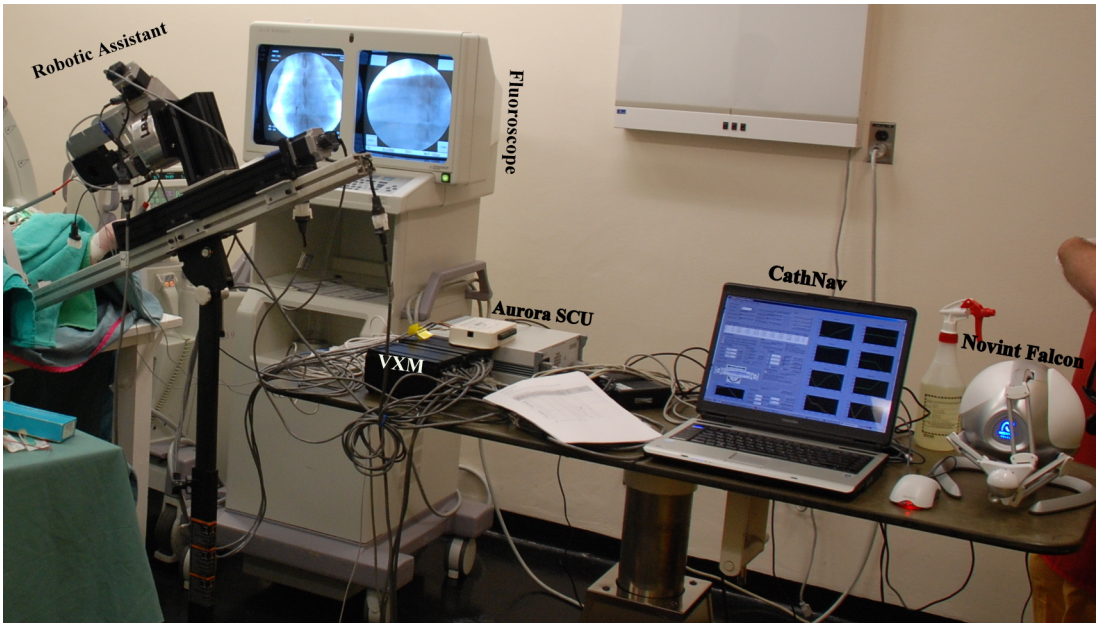

Figure 5.1: The complete system in the operating room.

ence between model position vector and the recorded tip position was defined as the modeling error. The error value was the basis in calculating the accuracy and precision of the modeling in-vivo. Accuracy was defined as the error mean value (μ) and precision was defined as the standard deviation of the error (σ). The error value was calculated for the three coordinates of the position vector (2.2), with respect to O_1 coordinate system in figure 2.4. The overall error was also calculated as the Euclidean distance between the measured position and the model estimation of the position.

Deflection

In this experiment, the distal shaft was deflected by turning the steering knob at the handle in 1 degree steps. The steering knob was turned from zero degrees up to 40 degrees and then turned back to zero. This back and forth rotation was repeated twenty times, resulting in 1600 position measurements for each animal. Table 5.1 presents the accuracy and precision figures.

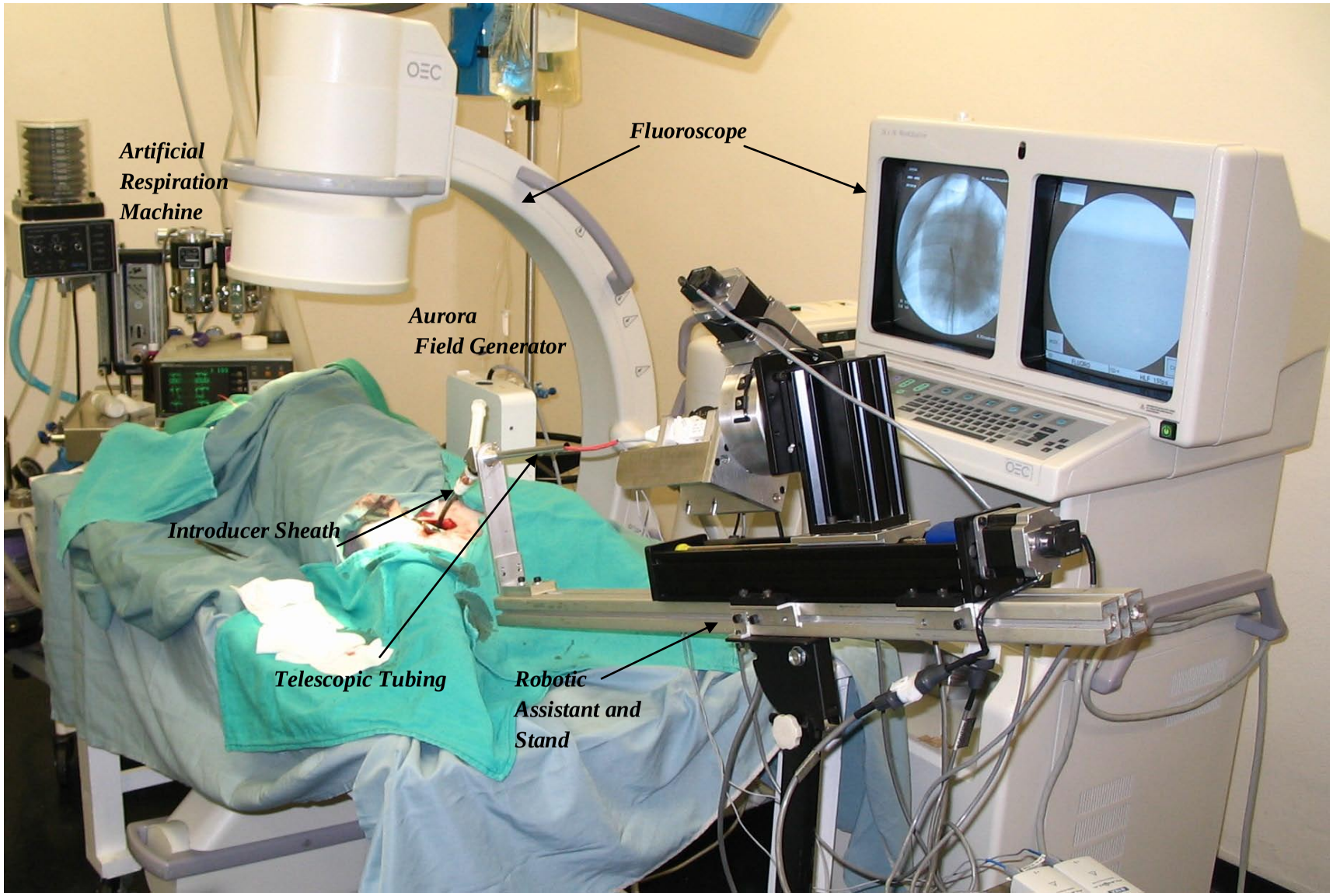

Figure 5.2: Robotic assistant setup in the operating room.

Table 5.1: Modeling error in deflection experiments. Mean (μ) and standard deviation (σ) of the error are presented for x, y, z coordinates of the catheter tip, in addition to the Euclidean distance between the model and the measured position, denoted without the coordinate subscripts. All measurements are in millimetre.

Subject	μ_x	σ_x	μ_y	σ_y	μ_z	σ_z	μ	σ
1	1.78	0.69	0.64	0.28	2.66	2.06	3.40	1.99
2	2.35	0.84	-1.88	0.50	0.63	2.59	4.10	0.58
3	1.81	0.21	0.59	0.15	1.18	0.22	2.26	0.28

Combined twist and deflection

In this experiment, the distal shaft was deflected and twisted linearly at the same time. The steering knob was turned linearly from zero degrees at 1 degree steps up to 36 degrees and then turned back to zero . The handle was also twisted similarly at 10 degree steps up top 360 degrees. This combined twist and deflection trajectory was traversed twenty times resulting in 1440 position measurements for each animal. Table 5.2 summarizes the error figures.

Table 5.2: Modeling error in combined twist and deflection experiments. Mean (μ) and standard deviation (σ) of the error are presented for x, y, z coordinates of the catheter tip, in addition to the Euclidean distance between the model and the measured position, denoted without the coordinate subscripts. All measurements are in millimetre.

Subject	μ_x	σ_x	μ_y	σ_y	μ_z	σ_z	μ	σ
1	2.15	0.76	0.58	0.46	2.42	1.68	3.41	1.68
2	0.67	1.42	-1.88	1.28	2.14	1.35	3.50	1.36
3	1.17	2.11	-2.70	0.94	3.01	1.51	4.81	1.47

The position errors measured in the experiments are generally under 5 mm. This indicates that the proposed model can be utilized as an approximation of the catheter's distal shaft shape and to parameterize the position vector of the tip. The model remains valid in the presence of intra-atrial pressure levels and under the displacements induced by respiration and cardiac contractions. Consecutively, the model is deployed to control the position of the catheter and to navigate the catheter inside the atrium. It is noted that the model does not account for any

interaction of the distal shaft with the intracardiac anatomy. As a result, when the shaft comes into contact with the endocardium, depending on the dynamics of the contact, the model's accuracy can be undermined. As demonstrated in the subsequent section, the control law (2.18) provides the basis for the successful navigation of the catheter, unless contact forces deform the catheter to the extent that the curvature constancy or zero torsion assumptions are strongly violated.

5.3 Automatic Navigation

To validate the capability of the platform, as described in chapter 3 and as set up in section 5.1, in navigating the catheter tip to desired positions, the reference sensor was positioned on three landmarks in the right atrium (low RA, high RA and Tricuspid Valve Annulus) in each animal. The catheter assembly was positioned so that the tip was in mid-atrium at the beginning of each navigation task. The system was commanded to direct the tip toward the reference sensor automatically till it reached and touched the reference sensor. The navigation task was ended when the supervising interventionalist was satisfied with the position of the catheter tip at the landmark, viewed under quasi bi-plane fluoroscopy. The initial and final distance between the catheter tip and the reference sensor were recorded along with the duration of the navigation task. The system was then commanded to take the catheter back to the initial mid-atrial position by "undoing" all the manipulations performed on the catheter during the navigation. Through UI controls and the 3D input interface, the catheter could be positioned manually at the mid-atrium if the catheter did not move completely back to the original position, due to the inherent hysteresis in the transfer of actuation at the handle to the distal shaft, especially when the catheter is twisted. For each landmark, the navigation manoeuvre was repeated five times. The trajectory planned for the catheter tip was a straight line between the instantaneous catheter tip position and the reference sensor position. This scheme was supposed to yield the shortest navigation time.

Figure 5.3 presents the initial and final configuration of the catheter assembly and the reference sensor in a sample navigation. As seen in the figure, the catheter tip touches the reference sensor at the end of navigation. Figure 5.4 illustrates a sample of distance readings between the catheter tip sensor and the reference sensor in a high RA navigation. In this figure, the successful navigation of the catheter in the presence of the disturbances due to the continuous beating cycle is visible. The ideal path to reach the reference sensor and the actual path taken due

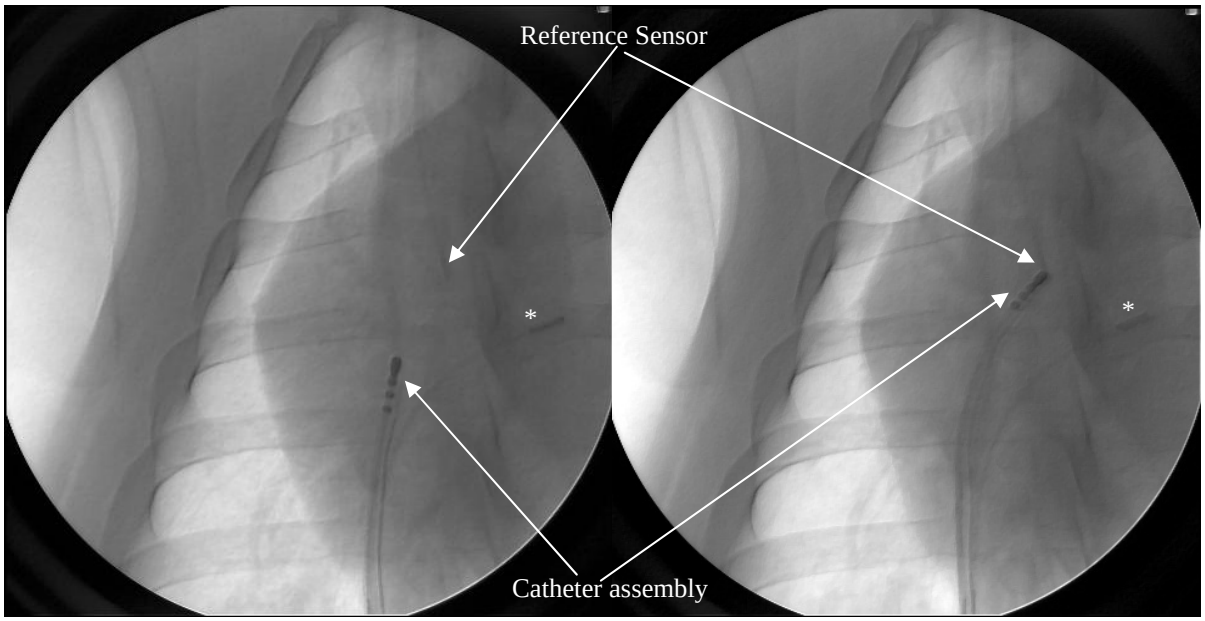

Figure 5.3: Initial (left) and final (right) positioning of the catheter assembly in navigation from mid-RA to high RA, as captured by fluoroscopy. The ICE catheter is marked with an asterisk.

to disturbances and uncertainties is depicted in the figure. The motion induced on the reference sensor by the cardiac contraction/relaxation cycle is clearly visible by the variations in the unfiltered distance readings. Figure 5.5 shows the recorded Euclidean distance between the tip and the reference sensors in a high RA navigation, along with the ideal straight path for this navigation. Again, the cardiac cycle disturbance is visible in the profile.

Table 5.3 presents the outcome of the automated navigation for each landmark. Except for one case where the catheter tip was stuck on its way to the Tricuspid Valve Annulus, the navigation tasks were all conducted successfully. The final distance between the reference sensor and the tip was generally below 10 mm. This means even though the catheter reached at the desired target according to the interventionalist, there was still some distance to the reference sensor. This was partly attributed to the direction of approach to the 9mm-long reference sensor coil, and to the dynamics of the contact between the catheter tip, the reference sensor and intra-atrial anatomy. The typical navigation time was between 30 and 60 seconds.

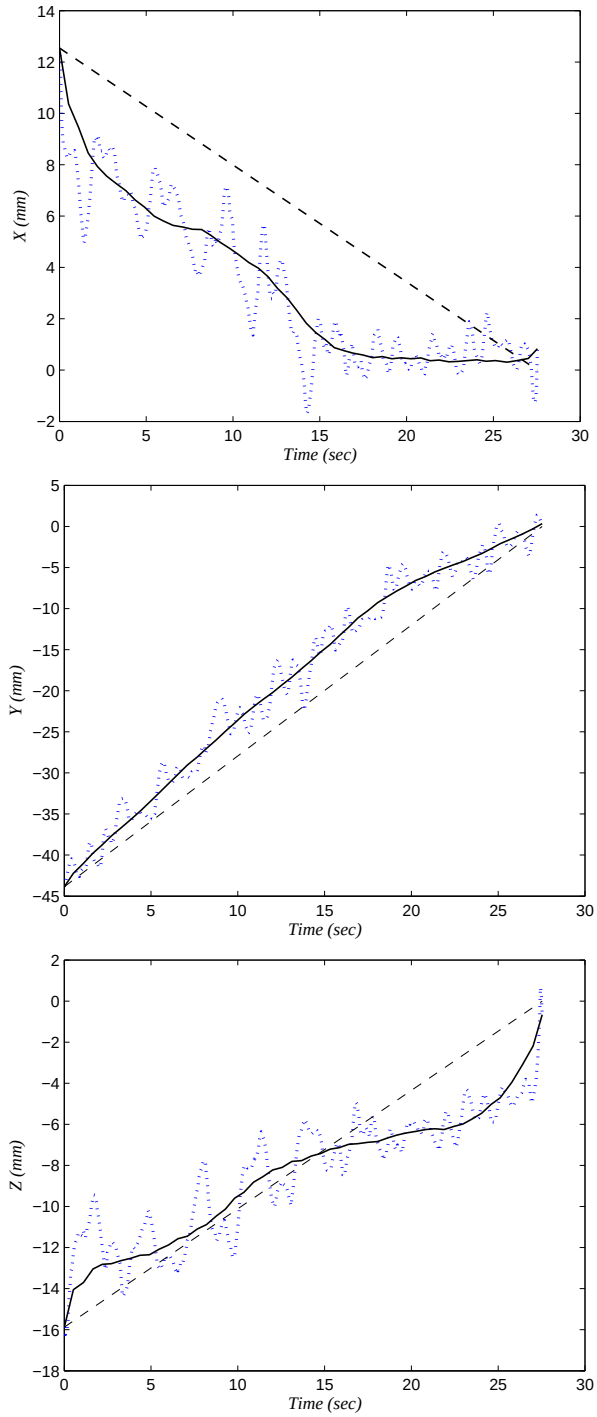

Figure 5.4: Sample automatic navigation profile. X, Y and Z coordinates of the distance vector between the catheter tip sensor and the reference sensor in a sample in-vivo navigation. Dashed line depicts the ideal straight path to the reference sensor. Solid line depicts the actual path the controller realized in navigating the catheter. Dotted line represents the distance readings, with unfiltered cardiac cycle disturbances.

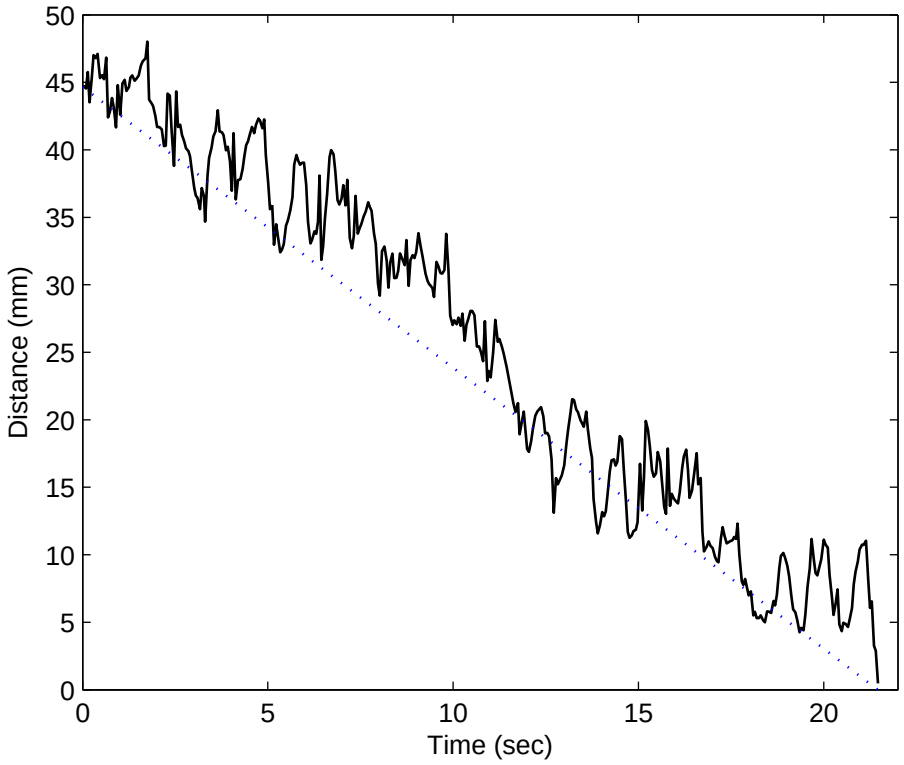

Figure 5.5: Euclidean distance between the tip sensor and reference sensor in a sample high RA navigation.

Table 5.3: Navigation performance in terms of initial and final distance between the catheter tip and the reference sensor and the duration for the system to perform the navigation automatically.

	Initial distance (mm)		Final distance (mm)		Duration (sec)	
Landmark	μ_i	σ_i	μ_f	σ_f	μ_t	σ_t
Tricuspid Valve Annulus	33.45	1.65	9.34	1.25	36.95	16.66
Low RA	30.91	2.76	7.38	2.93	46.16	18.34
High RA	37	3.25	5.02	2.21	45.91	15.29

5.4 Manual vs. Automatic Navigation

It was verified that the navigation system is capable of directing the catheter to reach a set target in the right atrium. To have a preliminary assessment of the system's performance in comparison with the manual positioning of the catheter, the interventionalist was asked to perform the same navigation tasks manually. In other words, the routine navigation of catheter in everyday catheterization operations was performed by manual steering of the catheter. For each navigation task, the interventionalist guided the catheter to reach the target sensor. When the interventionalist was satisfied with the position of the catheter relative to the reference sensor, that navigation task ended. For each task, the final distance between the catheter and the reference sensor was recorded along with the time it took to reach the reference sensor. Before performing each task, the interventionalist practiced reaching the reference sensor, so that the learning curve data is not included in the results. In figure 5.6, the performance of automatic and manual navigation are compared in terms of the final distance and the duration of operation.

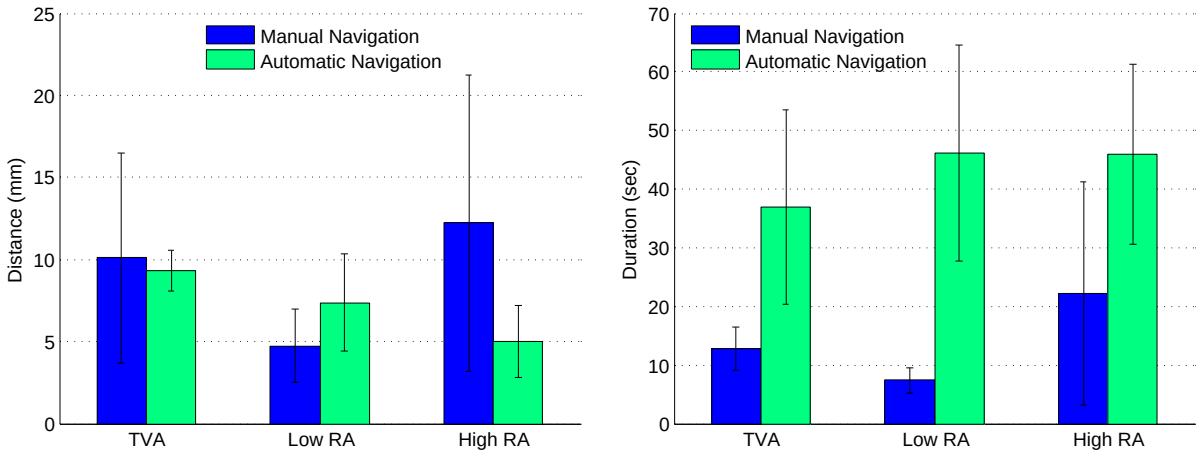

Figure 5.6: Comparison of automatic and manual navigation in terms of mean and standard deviation of (a) final distance between the catheter tip and the target, and (b) the navigation duration.

In figure 5.6(a) the final distance to the reference sensor is compared. While manual navigation to Low RA is better than automatic navigation, the standard deviation of distance is generally larger in manual navigation. This means automatic navigation performance is more consistent when conducting the same operation. The duration of operation, shown in figure 5.6(b), is generally much shorter in

manual navigation. The speed in manual navigation stems from the fact that the interventionalist has learned how to reach the target and is able to utilize his/her experience in effective steering of the catheter. However, the navigation system has no knowledge of an "optimized" way to reach its target. In addition, for safety reasons, the system is only allowed to move the catheter toward its target in small steps that are provided by trajectory planner. Inefficiency in motor control/driver hardware (VXM) is also a factor in slowing the system down. In the next chapter, some guidelines for improving the navigation performance is provided.

Due to the limited number of experiments and large variations in the results, no statistical inference can be made based on the results. More experiments with a larger sampling population is deemed necessary to reach a generalization on how the system performs in comparison with manual catheterization.

5.5 Discussion

The model proposed for distal shaft kinematics was validated through in-vivo experiments. The developed system was utilized to navigate the catheter tip from its instantaneous position to the desired position. The experiments demonstrated that the navigation is feasible in actual operations inside the right atrium, and the precision in reaching the target is generally better than manual navigation. The system steers the catheter more slowly compared to manual navigation.

In the experiments, there were instances where the distal shaft was stuck on its way to the reference sensor. Such obstacles once resulted in a failed navigation attempt while in other instances the system managed to release the catheter. This resulted in variations in the duration of navigation tasks, as large value for σ_t in table 5.3 indicates. For safety reasons, CathNav stops robotic manipulation when the tip configuration does not change after multiple attempts. The intracardiac anatomical features are obstacles that the catheter should avoid on its path. The path planned in CathNav software is a straight line from the catheter tip to the target position. To enhance the navigation capability, the system should accommodate different curves as navigation path of the tip to avoid anatomical obstacles.

The proposed rigid model for the catheter can lose its accuracy when contact forces with the endocardium affect the shape of the distal shaft considerably. It is true that various intracardiac anatomical features such as valves, papillary muscles, chordae tendineae, and myocardial walls exert forces on the distal shaft that can affect the deflection of the distal shaft. In actual operations, the interventionalists

might deform the shaft against the endocardium to reach a desired location as well. The kinematic model can describe the catheter shape as long as the planar deflection and constant curvature assumptions are not violated, i.e., when the external forces do not deform the distal shaft significantly. The experiments showed that in the presence of quasi-uniform distribution of force/pressure on the shaft, the model is able to predict the distal shaft configuration. Upon contact with anatomical features of the heart, depending on the contact dynamics, the model's accuracy decreases. To account for contact deformations, the model can be extended by relaxing the links' rigidity assumption and incorporating flexibility into the links. The developed static model can also be extended to predict flexible link deformations due to given external forces. Nonetheless, how the distal shaft deforms in contact with the endocardium is an open question that is left for future research.

The catheter assembly with the attached Aurora® sensors increases the diameter of the catheter, and limits the deflection of the distal shaft. It also limits the translation of torque from the proximal section to the distal shaft. Ideally, the sensors could be embedded inside the catheter, thus allowing better manoeuvrability of the tip. In addition, it is expected that by inclusion of better actuators for the robot, the navigation time can be reduced.

A benefit of the navigation system is the reduction of x-ray exposure. In manual catheterization, fluoroscopy is used to view the catheter configuration inside the heart and to guide the interventionalist in handle manipulation. This entails the exposure of both the patient and the interventionalist to x-ray. Using the robotic system, the navigation can be supervised and managed away from the patient and the fluoroscope, eliminating the interventionalist's exposure to radiation. Moreover, when automatic navigation is utilized, fluoroscopy would only be required for verification purposes and the fluoroscope could be turned off during navigation. This results in the reduction of patient's exposure as well. Generally, once the distal shaft is placed inside the cardiac chambers, the interventionalist's exposure could be reduced up to 100%. The actual reduction ratio is not measured through this research.

Finally, a brief comparison with the competing technologies [68] already in clinical practice is in order. Sensei™uses a proprietary steerable dual sheath system and achieves a stable control over the passive catheter position that is threaded through the sheath. Sensei™ provides enhanced but not automatic navigation. Our navigation system provides a simpler method to achieve semi-automatic navigation without additional sheaths. Both robotic systems, however, require extra safety measures to avoid traumatic navigation. On the other hand, Niobe® realizes mag-

netic navigation of a proprietary magnetic catheter and performs semi-automated mapping. Niobe® is a very safe solution with no risk of cardiac perforation but it requires a complete catheterization lab customization. In short, the developed system provides the advantage of automatic navigation with less complexity and cost compared to the existing technologies. It is noted that none of the existing systems achieve shorter navigation time compared to manual navigation. The same is true for the developed system. However, the system requires manual insertion of the catheter prior to navigation in contrast to both systems. In addition, to be adopted for clinical practice, the catheter will require the Aurora® sensors to be embedded inside the steerable catheter.

5.6 Conclusion

The animal experiments verified that the catheter modeling provides acceptable accuracy and precision in the estimation of the catheter tip position. The experiments also verified the feasibility of automatic navigation of the catheter from a given position to a desired position marked using a reference sensor. Based on the experimental results, the requirements for future developments of the system are identified. Chapter 6 covers the directions for the enhancement of the system for more challenging navigation tasks.

Chapter 6

Future Directions and Conclusion

The platform developed through this research is the first prototype of its kind. There were many trials and errors in the course of the research and the navigation system is far from perfect. The feasibility of navigation of the catheter through a robotic system without reliance on a specific or proprietary steerable sheath of catheter was proved through in-vivo experiments. The experience gained through this research provides the insight required to plan the work ahead to progress this system to the level ready for deployment in operating room for human patients. In addition, if the navigation system is to be adopted by interventionalists and electrophysiologists, there are features that need to be added to the system . Based on the experience gained through collaboration with medical professionals and in the in-vivo experiments, the recommended enhancements for future developments are outlined in this chapter.

6.1 Robotic Assistant

The developed robotic assistant provides the basic functionality required for navigation. However, there are shortcomings and practical issues in the system that need to be addressed for further developments. In the following, a summary of the issues is provided.

6.1.1 Motor controllers

In the course of the experiments, the VXM controller proved to be the slowest component in the control loop, due to the following shortcomings:

- The commands to the VXM are in the forms of small program codes that are run sequentially by the controller. Once a program is being run, the controller does not accept new commands, except for immediate stop commands. The control software has to wait for VXM to finish running the program before issuing a new command. As a result, if the controller decides that an issued command has to be corrected, the motors has to stop before a corrective action is possible. This issue can undermine the controller's performance.
- The VXM acceleration is limited and it cannot execute small displacements with high speeds, as it has to accelerate to start and decelerate to stop.
- The VXM pair is capable of simultaneous control of only two motors. The robotic assistant has three DOFs, and in motion scenarios where all three DOFs are utilized, one DOF has to be actuated following the other two. This induces another delay source in the control loop.

A fast motor driver/controller solution, capable of simultaneous axis control is deemed necessary for higher control performance. Such a solution, has to accept new control commands at any instant by overriding the old possibly in-progress commands.

In addition to a more capable motor controller, the robot motors could also be upgraded to DC motors for better dynamic performance and closed-loop control of the motor. Apparently, DC motor drives will be also needed in the system. Using DC motors provides the benefit of velocity and acceleration control of the robot, not available with VXM stepper motor controller.

6.1.2 Catheter Feeding Mechanism

The robotic apparatus performs all the catheter actuations at the handle. The steering knob rotations are directly transferred to the distal shaft, but the transfer of translation and twist at the handle to the catheter body is not a trivial task. In fact, one of the mechanical challenges of the robotic assistant is to ensure that the translation and twist actions at the handle are transferred to the catheter body at the point of entry into the introducer sheath.

The catheter operates on the principle that a flexible tube can transfer motion from one end to the other when constrained in a luminal structure. This principle was utilized in the experiments by a telescopic rigid tubing that covered the catheter body from the handle to the introducer sheath. The tubing constrained

and straightened the catheter body. With this mechanism, the translation of the handle resulted in insertion or retraction of the catheter into or out of the introducer sheath, as there was no room for the catheter section inside the tubing to bend or kink. Handle rotations were also transferred from the handle to the inside section of the catheter, assuming the catheter body was rigidly attached to the handle. However, the experiments proved that although the translation is transferred to the body easily, handle rotation is not transferred as well. In fact, the transfer of twist action degrades as the catheter body exhibits signs of axial torsion and fatigue, especially at the point of attachment to the handle. This necessitates a better catheter feeding mechanism capable of both translation and twist transfer.

CardioDrive™(Stereotaxis, St. Louis, MO) is a catheter advancer system that is a part of Niobe® solution. Jayender et. al [69] have utilized a robotic manipulator specifically for the purpose of catheter insertion/retraction. None of the two solutions provide for the transfer of torque to catheter body. A feeding mechanism is required to be designed and developed for effective actuation transfer.

6.2 Catheter Modeling

The rigid model of the catheter was validated in phantom and animal experiments. However, the model validity is based on zero torsion and constant curvature assumptions. Forces exerted on the distal shaft upon contact with the endocardium can invalidate the assumptions and undermine the fidelity of the model, resulting in poor navigation performance.

To address this issue, the model's rigid links can be replaced with flexible beams, modeling the distal shaft as a flexible manipulator. As a result, the model could include the physics of elastic bending due to contact with the intracardiac anatomy, providing for navigation to more difficult to reach landmarks on the endocardium. In addition to better distal shaft modeling, catheter body and its role in the transfer of actuation from handle to the distal shaft could be further studied. More effective models could yield better control over catheter tip position with improved speed and accuracy.

6.3 Navigation

Many features could be added to the navigation system, to achieve higher performance, better safety, and more functionality. In this section, visualization, force feedback, safety, and automated navigation are identified as the major areas of improvement.

6.3.1 Visualization

In the experiments, the 3D input device demonstrated an alternative to conventional twist, push/pull, and bend paradigm for catheter manipulation at the handle with a more intuitive superior/inferior, posterior/anterior, left/right paradigm at the tip where actual navigation takes place. However, it was learned that relying on fluoroscopy and intracardiac echocardiography (ICE) proves insufficient for manual navigation of the catheter through the 3D input device. While the interface provides a significant improvement in navigation approach, a graphical visualization is required to display the cardiac anatomy and the distal shaft position registered on the anatomy. The interventionalists can then conveniently control the catheter tip position through the system. Such a system requires a realistic static model of heart on which the distal shaft is registered during the operation.

6.3.2 Force Feedback

Falcon Novint device was used in the system as a 3D input device rather than a haptic device. Since the interaction between the interventionalist and the system is one-sided and no visualization is provided, the interventionalist does not feel comfortable controlling the system as he is not sure what exactly happens in response to his commands. The haptic device can be used to introduce force/impedance feedback in response to the input velocity/displacement proportional to the motion created at the tip while resisting motion beyond endocardial boundaries. The transparency of the control system is a key factor in the haptic experience the interventionalist receives. The control transparency could be the ultimate goal for the navigation system, such that the resistance that catheter encounters as it advances toward its target is transferred *instantly* to the hand of the interventionalist. Ideally, the interventionalist should feel that (s)he is moving the distal tip with her/his hand.

6.3.3 Control

To achieve transparency, the performance of control methodologies utilized in the system must be improved. The control architecture needs to be fast enough to realize the navigation commands issued by the 3D input device. A key factor is how the non-linearities in the dynamics of actuation from the handle to the tip are overcome. Such nonlinearities vary as the configuration of the catheter body and its contact points with the intravascular anatomy changes. An adaptive approach is deemed necessary to address the time-varying non-linear behaviour of the catheter.

In any robotic navigation system, safety is of crucial importance. For intracardiac navigation, the force that the distal shaft and especially the tip exerts on the myocardium determines the safety of manoeuvres. Excessive force could result in the perforation of cardiac walls and structures, as the catheter can act like a blunt needle. This means a force/tactile safety feature is a pre-requisite for the deployment of such a system in real human operations. If the force exerted by the catheter exceeds a safety threshold the system could automatically stop or retract the catheter to avoid any potential trauma to the cardiac tissue. In addition, such a force/tactile measurement could provide force feedback to the interventionalist through the haptic device.

In addition to position control, orientation control could also be considered to improve trajectory planning for hard-to-reach targets. We have shown that the distal shaft in under-actuated. To achieve position control, orientation DOFs cannot be controlled simultaneously. However, to accommodate effective navigation and ablation, a methodology is required to utilize the DOFs for position, orientation or hybrid control that optimizes performance depending on the target landmark and anatomic constraints.

Finally, from the control theory perspective, the study and analysis of the control system's stability and robustness in both time and frequency domains and how to tune the control system for best performance is designated for the future.

6.3.4 Tracking

To provide a target position for automated catheter navigation, an Aurora® sensor was used in the experiments. However, to use the automatic navigation feature in actual operation, an alternative method is required to input the coordinates of a point on the endocardium as the target position to the system. One possibility is to

utilize intracardiac echocardiography (ICE) for this purpose. ICE can be used as an imaging modality to view the intracardiac anatomy intraoperatively. An operator can mark a target zone on the ICE image. The ICE image can be registered in Aurora® coordinate system by attaching an Aurora® sensor coil to the ICE catheter. As a result, the designated target zone coordinates can be obtained in Aurora® coordinate system. The obtained coordinates can be fed as the target point to CathNav. This technique can be further enhanced by tracking the target zone in the ICE image stream, obtaining the real-time position of the target for navigation.

An approach to target tracking on the endocardium is to delineate the endocardial boundary for each image frame and then track the boundary points as the boundary changes and deforms in the ICE image sequence. An algorithm was proposed for boundary detection by the author in [70]. A method to track the detected boundary is to use graph matching. An overview of graph matching algorithms in image processing is provided in [71]. Once the target zone is tracked, the navigation system could be used to position the catheter tip on the target and then maintain the contact with the endocardium for enhanced ablation. For this purpose, fine motion and contact control are issues to be addressed. Moreover, the target does not necessarily move in the 2D ICE image plane, which means the actual 3D profile of the target is unknown. This is another issue to be dealt with.

6.3.5 Trajectory Planning

The trajectory planning algorithm for CathNav realizes the navigation of the catheter to the target on a straight path. This approach does not avoid cardiac structures that could be the obstacles on the path. The trajectory needs to be customized so that such obstacles are avoided as the catheter progresses toward its target position.

6.4 Conclusion

Through this research, a platform was conceived, developed and deployed to achieve robot-assisted intracardiac catheter navigation. To realize catheter navigation, multiple disciplines and different technologies are utilized. Tracking technologies are required to find the position of the catheter and to utilize this position for navigation and control purposes. Actuation mechanisms are needed to motorize and

automate catheter manipulation. A model is also called for to estimate the configuration of the steerable section of the catheter in response to actuation at the handle. To achieve a navigation system through the course of this research, Aurora® electromagnetic tracking system was identified as a position tracking technology. A robotic system was required to manipulate a steerable ablation catheter. A kinematic model for the distal shaft of the catheter was formulated that models the catheter as a continuum manipulator.

The kinematic model is based on the steering mechanism of the catheter. The model assumes that catheter deflects with constant curvature and zero torsion. This means the catheter bends in one plane of deflection and forms an arc of a circle when deflected. A static pseudo-rigid model of the catheter was also formulated to investigate whether the kinematic assumptions conform to the reality of catheter deflection. The model properties including its reachable workspace and its position and orientation singularities were analyzed. The model was used to formulate differential kinematics of the catheter and to design a strategy for position control of the catheter. Based on the position control strategy, an architecture was proposed to achieve catheter navigation.

Based on the developed architecture, the navigation platform was developed. A robotic assistant was designed and constructed, and a 3D input device was chosen for intuitive catheter steering. A software platform, named CathNav, was developed to communicate with various devices of the system and to implement the navigation architecture, while providing a graphical user interface for the interventionalist to manage and supervise navigation. In this implementation, Aurora® position readings were calibrated, model joint parameters were extracted from position readings, and coordinate systems of model, Aurora® system, Aurora® sensors, robotic assistant and 3D input device were converted to each other as required.

The modeling assumptions of constant curvature and zero torsion were verified through experiments on the catheter using the pseudo-rigid static model. Kinematic modeling was validated through in-vitro experiments using the navigation system and a static phantom. The phantom simulated the anterograde path to the heart and provided the static pressure levels similar to heart's right atrium, right ventricle and left atrium.

The kinematic modeling further was validated by experiments on live animals by threading the catheter into the beating heart of the porcine subjects. In-vivo experiments also demonstrated that the system is capable of automatic navigation of the catheter to designated targets in the right atrium. It was shown that compared

to manual navigation, the system achieves similar accuracy with better precision and lower speed.

The robot-assisted catheter navigation platform, developed through this research, has the potential to be adopted for human deployment. There are some barriers that need be overcome prior to deployment. The catheter needs to have embedded electromagnetic tracking capability. The haptic interface has to be customized to match the needs and the taste of the medical professionals. The robotic system must be sterilizable to be used in the catheterization lab. Animal and human trials must prove the benefit and safety of such a system. Regulatory standards must be observed and the whole system must receive regulatory clearance. Through training and information sessions, electrophysiologists and interventionalists need to learn the benefits of such a system and tend to rely on the system. Finally, when the system is accepted by the interventionalists it will have the chance of deployment.

In the end, the contributions made through this research are summarized:

1. A kinematic model for the distal shaft of steerable catheters, and the study of distal shaft workspace and singularities under the kinematic model [45, 44, 42, 43].
2. A static modeling methodology for the planar deflection of the catheter's distal shaft [42].
3. A method for catheter tip position control [43].
4. A strategy for semi-automated catheter navigation.
5. Three methodologies of motorized, assisted and automatic catheter manipulation.
6. A robotic mechanism for assisted catheter manipulation [44, 42, 43].
7. CathNav: A software platform for robot-assisted catheter navigation [42, 43].
8. In-vitro validation of kinematic modeling through construction a static phantom [44, 42].
9. In-vivo validation of kinematic modeling [43].
10. A complete platform for robot-assisted intracardiac catheter navigation [43].

11. In-vivo validation of automatic navigation through the developed platform [43].

12. A method for fast boundary delineation in ICE images [70].

Appendix A

Robotic Assistant Specifications

This appendix provides the details of robot design specification calculations outlined in table 3.1 or A.1 below.

Table A.1: The specifications for linear and rotary stages of the robot.

Parameter	Linear translation	Handle twist	Knob control
Travel Range	24.22 cm	±540°	±45°
Resolution	0.2 mm	0.1°	0.025°
Accuracy	0.3 mm	0.2°	0.05°
Max Speed	67 mm/s	360°/s	45°/s

A.1 Travel Range

For the linear slide, the distance is based on cardiac chambers dimensions. The range is the maximum displacement required for the catheter to cover the circumference of a cardiac chamber. Assuming the largest cardiac chamber, i.e. left ventricle, has an elliptical cross-section, the circumference of the half-ellipse would be a maximum of 24.22 cm, for end-diastole major axis = 10 cm and end-diastole minor axis = 5 cm. The dimensions are obtained from [72].

According to SteeroCath-T specification, the catheter handle and shaft should not be rotated more than 1.5 full rotations. This allows a 540° range for twist rotary stage. The steering knob of this catheter can be turned up to 45° in each direction, giving 45° range to the knob rotary stage.

A.2 Resolution and Accuracy

Resolution and accuracy figures are determined by the pose measurement system specifications. Position measurement of 6DOF Aurora® sensors achieve an accuracy of 0.6 mm and a precision of 0.4 mm. Resolution and accuracy of the linear and rotary stages are designated to be half of Aurora® accuracy and precision values. Assuming a linear relationship between the displacements at the handle and the displacements at the tip, the required linear stages accuracy and resolution will be 0.3 mm and 0.2 mm respectively.

In terms of orientation, Aurora® provides an accuracy of 0.4° and a precision of 0.2°. Assuming a linear relationship between the twist angle at the handle and the twist angle at the distal shaft, the required linear stages accuracy and resolution will be 0.2° and 0.1° respectively. For knob rotation, since the range of the deflection angle is 180° compared to 45° at the knob. The required accuracy and resolution for knob rotary stage will be a 1/8 of the same figures for Aurora®, yielding 0.05° and 0.025° respectively.

A.3 Maximum Speed

The maximum speed required for the linear slide is based on the maximum speed of left ventricular wall. The myocardium moves nearly 2 cm in 300 ms during systole which is equal to 66.7 mm per second. For twist rotary stage, a complete rotation per second is assumed to be the maximum speed practically required. For knob rotary stage, the maximum feasible speed is to cover the full range of defection in one second.

Appendix B

General Specifications for a Dynamic Heart Phantom

B.1 Overview

The dynamic phantom will simulate the pressure/volume/flow parameters inside the cardiac chambers. It will be composed of a beating ventricle and a closed loop fluid system that simulates blood circulation. A sample mock circulatory system is presented in figure B.1.

The system shall simulate both left and right ventricle, with the potential to add atrial chambers as well. Ideally the cardiovascular physiology shall be mimicked by the dynamic phantom. To this end the components of the phantom and their functional requirements are outline in the next section.

B.2 Components

Referring to figure B.1, the components of the dynamic phantom include:

1. Ventricle: Right and left ventricles can be made from Silopren (LSR 2050 GE Silicones). An inner cast from a porcine ventricle can be used to mould the silicone. To achieve an elasticity similar to heart walls, the thickness of silicone in the mould can vary similar to the real heart.

2. Valves: Two valves regulate the flow into and out of the ventricle. The biological valves act as check valves. Currently prosthetic valves are butterfly

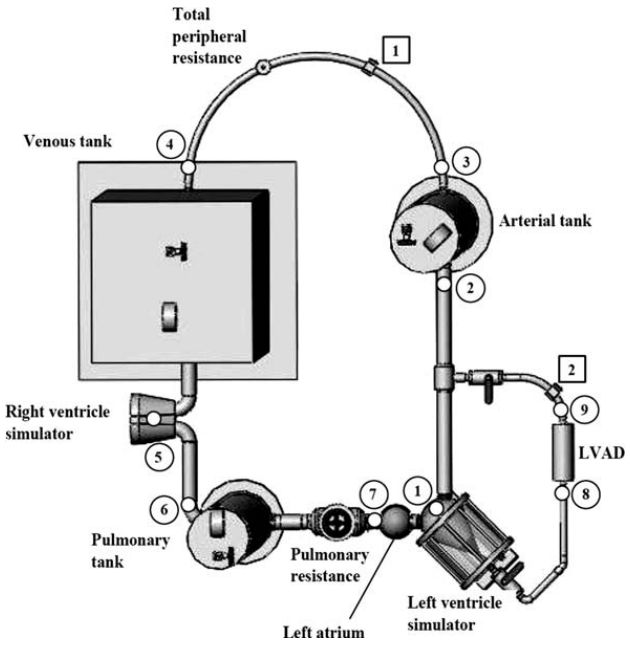

Figure B.1: A sample mock human circulatory system. Numbered circles are pressure sensors and numbered squares are ultrasonic flow sensors. Reproduced from figure 1 in [73] with kind permission of Springer Science and Business Media.

valves with single or double discs. The inner diameter of the valve is 20-25 mm.

3. Heart Driver specifications include:

   (a) A pneumatic or hydraulic driver

   (b) Ventricle output: up to 10 L/min.

   (c) Rate: up to 120 beats/min.

   (d) Operating pressure: up to 120 mmHg

   (e) Strike volume: up to 100 mL

4. The systemic/pulmonary circulation parameters include:

   (a) Mean Arterial Pressure: 81-115 mmHg

   (b) Mean Venous Pressure: 7-8 mmHg

   (c) Arterial Compliance[1] : 2.2 mL/mmHg

[1]Compliance is defined as $C = \frac{\Delta V}{\Delta P}$. For an air-sealed tank it can be calculated by $C = (V_{tank} - A_{tank}h)/(P_{fluid} - \rho gh)$.

(d) Venous Compliance: 50 mL/mmHg

(e) Total systemic peripheral resistance, i.e., systemic vascular resistance 1463 dyne.s.cm^{-5}

(f) Pulmonary vascular resistance: 106 dyne.s.cm^{-5} ’

5. A blood analogue must offer a viscosity of 4x10^{-3} Pa.S. A possible solution can be mixture of around 85% weight pure water, 11% glycerol and 4% D4876 dextran[74]. Alternatively a ready made blood mimicking fluid (e.g., from CIRS, Norfolk, VA) can be used.

6. Instrumentation: pressure meters and flow meters to monitor pressure and volume inside the ventricle.

7. Tubing can be of Tygon or clear flexible PVC tubes.

8. Access path for the catheter: To access the right ventricle the catheter normally enters the body through right femoral vein and passes through right external iliac vein, right common iliac vein, and inferior vena cava to reach the right atrium. This path can be constructed using ready-made mock vessels of different lengths and diameters (e.g., from Limbs and Things, Savannah, GA). In a 3D coordinate system, the mock vessels can be connected together at the key points listed in table B.1. The data in this table is measured from the torso CT of a middle-aged male patient. The cross sections of veins are assumed elliptical and two diameters of the ellipse are presented in the table. The reference coordinate system is shown in figure B.2.

Table B.1: Coordinates of anterograde path to the heart.

X (cm)	Y (cm)	Z (mm)	Length (mm)	Diameter 1 (cm)	Diameter 2 (cm)
9.4	13.5	0	40.35	0.8	0.8
10.9	14.5	36.1	15.31	1.1	1.1
11.4	14.6	50.54	42.67	0.7	0.7
12.6	13.6	90.25	26.72	1.6	1.6
13.3	12.2	111.91	24.21	1.6	1.6
13.9	11.3	133.57	8.25	1.6	1.6
14.3	11.3	140.79	43.2	1.7	1.7
16	11.3	180.5	29.33	3.5	1.7
15.5	11.4	209.38	39.94	2.2	2.2
15.2	11.7	249.09	32.74	2.3	2.3
15.2	12.1	281.58	58.22	3.7	2.2
15	12.8	339.34	36.27	2.4	1.7
14.8	14.4	371.83	9.75	2.2	2.2
14.9	13.5	375.44	-	2.9	2.4

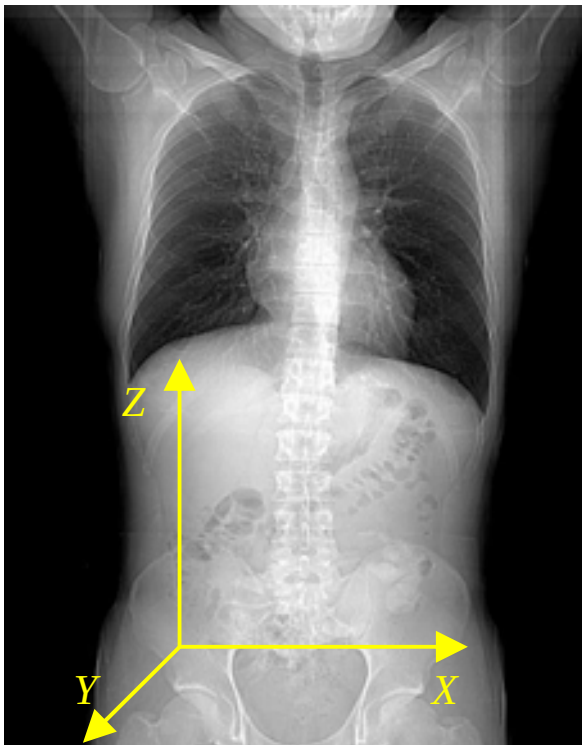

Figure B.2: The reference coordinate system in measurements overlayed on a CT image.

Appendix C

Animal Test Procedure

C.1 Kinematic Validation

C.1.1 Objective

To evaluate the validity of the catheter model in intracardiac environment.

C.1.2 Setup

- Sedated animal prepared for catheterization.
- Fluoroscope device (GE OEC Series 9800 cardiac mobile C-arm)
- NDI Aurora® system with two sensor coils interfaces
- Catheter assembly: One SteeroCath-T equipped with two sensor coils attached on both ends of the deflectable section of the distal shaft and connected to Aurora® (see figure 3.6(b) and section 3.3).
- Robotic apparatus along with control components and the assembly
- CathNav software

C.1.3 Prerequisites

- Aurora® field generator must be mounted on a non-ferric (preferably wooden) and firmly fixed pedestal. The field generator should not move/vibrate while tracking.

- Aurora® system must be tested prior to experiment on the actual animal bed to make sure it can function well given the metallic interferences that might exist in the operating room.
- The robotic apparatus must be completely fixed on a pedestal to avoid any vibrations while operating.
- The CathNav software must be running and communicating with Aurora®, VXM and encoder reader prior to the procedure.

C.1.4 Procedure

1. SteeroCath-T catheter is advanced manually through right femoral entry to the right atrium.
2. The catheter handle is mounted on the robotic system.
3. In the right atrium:
   (a) Position the catheter in using the manual controls of the CathNav software.
   (b) Verify the availability of position measurements of the Aurora® system. The sensors must not be missing and the unitless error value must be well below 1.
      i. If the sensors are missing, stop tracking on the software. Turn Aurora® off and move the field generator closer to the animal torso and possibly at a slightly different angle. Turn on Aurora®, start tracking, and repeat step 3.(b).
   (c) For each scenario in the software:
      i. Select the scenario.
      ii. Set the number of iterations to 20.
      iii. Set the maximum number of steps and each step size.
      iv. Hit "Run Scenario". The system will actuate robotic apparatus for each scenario.
      v. When the scenario is finished, copy and rename the two "Auroraxx.txt" files to a directory named according to the scenario parameters.
      vi. If the catheter motion is restricted by anatomy, note down any catheter configuration anomalies due to the restriction.

C.1.5 End Point

Catheter position, timing and input actuations are all recorded by the software in "Auroraxx.txt" files for further analysis.

C.2 Navigation Validation

C.2.1 Objective

To evaluate the feasibility and performance of enhanced catheter navigation with the CathNav system.

C.2.2 Setup

- Sedated animal prepared for catheterization.
- Fluoroscope device (GE OEC Series 9800 cardiac mobile C-arm)
- NDI Aurora® system with three sensor coils interfaces
- One SteeroCath-T equipped with two sensor coils attached on both ends of the deflectable section of the distal shaft and connected to Aurora®. This catheter is called catheter assembly henceforth.
- One catheter equipped with one sensor coil at the tip. Alternatively, a single sensor can be used. This catheter/sensor is called Reference catheter henceforward.
- Robotic apparatus along with control components and the assembly
- CathNav software
- Select target landmarks, where Reference catheter is positioned and navigation toward them is tried.
- Select base position to start navigation from, when reaching each target.

C.2.3 Prerequisites

- Aurora® field generator must be mounted on a non-ferric (preferably wooden) and firmly fixed pedestal. The field generator should not move/vibrate while tracking.
- Aurora® system must be tested prior to experiment on the actual animal bed to make sure it can function well given the metallic interferences that might exist in the operating room.
- The robotic assistant must be completely fixed on a pedestal to avoid any vibrations while operating.
- By default, the field generator lies on the left side of the animal.
- The CathNav software must be running and communicating with Aurora®, VXM and the encoder reader prior to the procedure.

C.2.4 Procedure

1. Reference catheter is advanced manually through right/left jugular vein into the right atrium.
2. Catheter assembly is advanced manually through right/left jugular vein to the right atrium.
3. The catheter assembly handle is mounted on the robotic system.
4. The availability of position measurements of the Aurora® system is verified. The sensors must not be missing and their unitless error value must be well below 1.
   (a) If the sensors are missing, stop tracking on the software. Turn Aurora® off and move the field generator closer to the animal torso and possibly at a slightly different angle. Turn on Aurora®, start tracking, and repeat step 4.
5. For each select landmark in the right atrium:
   (a) Position the Reference catheter on the select landmark manually.
   (b) Repeat the following steps:

i. Position the catheter assembly on base position using the manual controls on the CathNav software or the 'Undo Tracking' feature.

ii. Record the initial distance to the Reference catheter.

iii. Using the Tracking feature and if necessary, Falcon input and manual controls in CathNav software direct the catheter assembly toward the target.

iv. Stop when the interventionalist is satisfied with the positioning. Record the time it took for the procedure using CathNav timer feature along with final distance.

(c) Dismount catheter assembly from the robotic apparatus.

(d) Repeat the following steps:

i. Position the catheter assembly manually on base position.

ii. Record the distance to the Reference catheter.

iii. Manually navigate the catheter to the select landmark.

iv. When the interventionalist is satisfied with the positioning, record the time it took for the procedure using CathNav timer feature along with final distance to the Reference catheter.

C.2.5 End Point

The following template form is filled for navigation toward each landmark. The raw data of the experiments is provided separately in [75].

- Date:
- Animal Profile: (Type, Gender, and Weight)
- Landmark Description:

Mode	Trial#	Start Distance Vector	End Distance Vector	Duration	Final Distance Vector	Success	Notes
Assisted Navigation	1 2 3 4 5						
Manual Navigation	1 2 3 4 5						

References

[1] K. Chatterjee, Ed., *Cardiology: An Illustrated Text/Reference.* Lippincott, 1991, vol. 1. 1

[2] L. Gepstein, G. Hayam, and S. A. Ben-Haim, "A novel method for nonfluoroscopic catheter-based electroanatomical mapping of the heart," *Circulation*, vol. 95, no. 6, pp. 1611 – 1622, March 1997. 4

[3] J. Sra and J. M. Thomas, "New techniques for mapping cardiac arrhythmias," *Indian Heart Journal*, vol. 53, pp. 423–444, 2001. 4

[4] F. H. M. Wittkampf, E. F. D. Wever, R. Derksen, A. A. M. Wilde, H. Ramanna, R. N. W. Hauer, and E. O. R. de Medina, "Localisa new technique for real-time 3-dimensional localization of regular intracardiac electrodes," *Circulation*, vol. 99, no. 10, pp. 1312–1317, March 1999. 4

[5] F. Wittkampf, P. Loh, R. Derksen, T. A. Simmers, and L. Eckardt, "Real-time, three-dimensional, nonfluoroscopic localization of the lasso catheter," *Journal of Cardiovascular Electrophysiology*, vol. 13, no. 6, pp. 630–630, June 2002. 4

[6] R. J. Schilling, N. S. Peters, and D. W. Davies, "Simultaneous endocardial mapping in the human left ventricle using a noncontact catheter : Comparison of contact and reconstructed electrograms during sinus rhythm," *Circulation*, vol. 98, no. 9, pp. 887 – 898, September 1998. 4

[7] C. C. Gornick, S. W. Adler, B. Pederson, J. Hauck, J. Budd, and M. Jeff Schweitzer, "Validation of a new noncontact catheter system for electroanatomic mapping of left ventricular endocardium," *Circulation*, vol. 99, no. 6, pp. 829–835, February 1999. 5

[8] P. Jia, B. Punske, B. Taccardi, and Y. Rudy, "Electrophysiologic endocardial mapping from a noncontact nonexpandable catheter: A validation study of a

geometry-based concept," *Journal of Cardiovascular Electrophysiology*, vol. 11, pp. 1238–1251, November 2000. 5

[9] S. Meyer and P. Wolf, "Application of sonomicrometry and multidimensional scaling to cardiac catheter tracking," *IEEE Trans. Biomed. Eng.*, vol. 44, no. 11, pp. 1061–1067, November 1997. 6

[10] N. M. DeGroot, M. Bootsma, E. T. V. D. Velde, and M. J. Schalij, "Three-dimensional catheter positioning during radiofrequency ablation in patients: First application of a real-time position management system," *Journal of Cardiovascular Electrophysiology*, vol. 11, no. 11, pp. 1183–1192, November 2000. 6

[11] S. A. Ben-Haim, "Catheter navigation in modern electrophysiology," *Journal of Cardiovascular Electrophysiology*, vol. 11, no. 11, pp. 1193–1195, November 2000. 6

[12] M. Earley, R. Showkathali, M. Alzetani, P. Kistler, D. Gupta, D. Abrams, J. Horrocks, S. Harris, S. Sporton, and R. Schilling, "Radiofrequency ablation of arrhythmias guided by non-fluoroscopic catheter location: a prospective randomized trial," *European Heart Journal*, vol. 27, no. 10, pp. 1223–1229, 2006. 6

[13] R. Fenici, K. Pesola, M. Makijarvi, J. Nenonen, U. Teener, P. Fenici, and T. Katila, "Nonfluoroscopic localization of an amagnetic catheter in a realistic torso phantom by magnetocardiographic and body surface potential mapping," *PACE*, vol. 21, no. 11, pp. 2485–2491, 1998. 6

[14] K. Pesola, J. Nenonen, R. Fenici, J. Loetjoenen, M. Maekijaervi, P. Fenici, P. Korhonen, K. Lauerma, M. Valkonen, L. Toivonen *et al.*, "Bioelectromagnetic localization of a pacing catheter in the heart," *Phys Med Biol.*, vol. 44, pp. 2565–2578, 1999. 6

[15] M. Bock, S. Muller, S. Zuehlsdorff, P. Speier, C. Fink, P. Hallscheidt, R. Umathum, and W. Semmler, "Active catheter tracking using parallel mri and real-time image reconstruction," *Magnetic Resonance In Medicine*, vol. 55, no. 6, pp. 1454–1459, 2006. 6

[16] C. Pappone, G. Vicedomini, F. Manguso, F. Gugliotta, P. Mazzone, S. Gulletta, N. Sora, S. Sala, A. Marzi, G. Augello, L. Livolsi, A. Santagostino, and

V. Santinelli, "Robotic magnetic navigation for atrial fibrillation ablation," *J Am Coll Cardiol.*, vol. 47, no. 7, pp. 1390–1400, April 2006. 7

[17] M. Armacost, J. Adair, T. Munger, R. Viswanathan, F. Creighton, D. Curd, and R. Sehra, "Accurate and reproducible target navigation with the stereotaxis Niobe® magnetic navigation system," *J Cardiovasc Electrophysiol.*, vol. 18, no. s1, pp. 26–31, 2007. 7, 8

[18] M. N. Faddis, W. Blume, J. Finney, A. Hall, J. Rauch, J. S. K. T. Bae, M. Talcott, and B. Lindsay, "Novel, Magnetically Guided Catheter for Endocardial Mapping and Radiofrequency Catheter Ablation," *Circulation*, vol. 106, pp. 2980–2985, December 2002. 7

[19] M. N. Faddis, J. Chen, J. Osborn, M. Talcott, M. E. Cain, and B. D. Lindsay, "Magnetic guidance system for cardiac electrophysiology: a prospective trial of safety and efficacy in humans," *J Am Coll Cardiol.*, vol. 42, no. 11, pp. 1952–1958, December 2003. 7

[20] S. Ernst, F. Ouyang, C. Linder, K. Hertting, F. S. andJulian Chun, H. Hachiya, D. Bansch, M. Antz, and K.-H. Kuck, "Initial experience with remote catheter ablation using a novel magnetic navigation system," *Cicrulation*, vol. 109, pp. 1472–1475, 2004. 7

[21] W. Saliba, V. Reddy, O. Wazni, J. Cummings, J. Burkhardt, M. Haissaguerre, J. Kautzner, P. Peichl, P. Neuzil, V. Schibgilla *et al.*, "Atrial fibrillation ablation using a robotic catheter remote control system: Initial human experience and long-term follow-up results," *J Am Coll Cardiol.*, vol. 51, no. 25, pp. 2407–2411, 2008. 7

[22] P. Kanagaratnam, M. Koa-Wing, D. Wallace, A. Goldenberg, N. Peters, and D. Davies, "Experience of robotic catheter ablation in humans using a novel remotely steerable catheter sheath," *J Interv Card Electrophysiol.*, vol. 21, no. 1, pp. 19–26, 2008. 7

[23] W. Saliba, S. Ernst, V. Reddy, and K. Kuck, *Atrial Fibrillation, From Bench to Bedside.* Springer, 2008, ch. Remote Catheter Navigation, p. 392. 8

[24] K. Ikuta, H. Ichikawa, K. Suzuki, and D. Yajima, "Multi-degree of freedom hydraulic pressure driven safety active catheter," in *Proc. IEEE Int. Conf. on Robotics and Automation (ICRA'06)*, Orlando, FL, May 2006, pp. 4161–4166. 9

[25] Y. Haga, Y. Muyari, T. Mineta, T. Matsunaga, H. Akahori, and M. Esashi, "Small diameter hydraulic active bending catheter using laser processed super elastic alloy and silicone rubber tube," in *Proc. IEEE/EMBS Special Topic Conf. on Microtechnology in Medicine and Biology*, Kahuku, Hawaii, 2005, pp. 245–248. 9

[26] Y. Bailly and Y. Amirat, "Modeling and control of a hybrid continuum active catheter for aortic aneurysm treatment," in *Proc. IEEE Int. Conf. on Robotics and Automation (ICRA'05)*, Barcelona, Spain, April 2005, pp. 924–929. 9

[27] Y. Haga, T. Mineta, and M. Esashi, "Active catheter, active guidewire and related sensor systems," in *Proc. of World Automation Congress*, vol. 14, Orlando, FL, June 2002, pp. 291–296. 9

[28] J. Jayender and R. Patel, "Master-slave control of an active catheter instrumented with shape memory alloy actuators," in *Proc. IEEE/RSJ Int. Conf. on Intelligent Robots and Systems (IROS'07)*, San Diego, CA, Oct 2007, pp. 759–764. 9

[29] L. Cercenelli, E. Marcelli, and G. Plicchi, "Initial experience with a telerobotic system to remotely navigate and automatically reposition standard steerable ep catheters," *ASAIO Journal*, vol. 53, no. 5, pp. 523–529, 2007. 9

[30] K. Ikuta, K. Iritani, and J. Fukuyama, "Mobile virtual endoscope system with haptic and visual information for non-invasive inspection training," in *Proc. IEEE Int. Conf. on Robotics and Automation (ICRA'01)*, Seoul, Korea, May 2001, pp. 2037–2044. 10

[31] S. Dawson, S. Cotin, D. Meglan, D. Shaffer, and M. Ferrell, "Designing a computer-based simulator for interventional cardiology training," *Catheterization and Cardiovascular Interventions*, vol. 51, no. 4, pp. 522–527, December 2000. 10

[32] M. Kukuk and B. Geiger, "A real-time deformable model for flexible instruments inserted into tubular structures," in *Proc. Medical Image Computing and Computer-Assisted Intervention (MICCAI'02)*, Tokyo, Japan, September 2002, pp. 331–338. 10

[33] M. Konings, E. van de Kraats, T. Alderliesten, and W. Niessen, "Analytical guide wire motion algorithm for simulation of endovascular interventions,"

Medical and Biological Engineering and Computing, vol. 41, no. 6, pp. 689–700, November 2003. 10

[34] Y. Cai, C. Chui, X. Ye, J. Anderson, K. Liew, and I. Sakuma, "Simulation-based virtual prototyping of customized catheterization devices," *Journal of Computing and Information Science in Engineering*, vol. 4, no. 2, pp. 132–139, June 2004. 10

[35] W. Lawton, R. Raghavan, S. Ranjan, and R. Viswanathan, "Tubes in tubes: Catheter navigation in blood vessels and its applications," *International Journal of Solids and Structures*, vol. 37, no. 22, pp. 3031–3054, May 2000. 10

[36] M. Rubin, *Cosserat theories: shells, rods and points*. Kluwer Academic Publishers, 2000. 10

[37] W. L. Nowinski and C. K. Chui, "Simulation of interventional neuroradiology procedures," in *International Workshop on Medical Imaging and Augmented Reality (MIAR '01)*, Hong Kong, May 2001, p. 87. 10

[38] S. Cotin, C. Duriez, J. Lenoir, P. F. Neumann, and S. Dawson, "New approaches to catheter navigation for interventional radiology simulation," in *Proc. Medical Image Computing and Computer-Assisted Intervention (MICCAI'05)*, Palm Springs, CA, October 2005, pp. 534–542. 10

[39] J. Lenoir, S. Cotin, C. Duriez, and P. Neumann, "Interactive physically-based simulation of catheter and guidewire," *Computers & Graphics*, vol. 30, no. 3, pp. 416–422, June 2006. 10

[40] Y. Wang, C. Chui, H. Lim, Y. Cai, and K. Mak, "Real-time interactive simulator for percutaneous coronary revascularization procedures," *Computer Aided Surgery*, vol. 3, no. 5, pp. 211–227, 1998. 10

[41] J. Lenoir, P. Meseure, L. Grisoni, and C. Chaillou, "Surgical thread simulation," in *Modelling and Simulation for Computer-aided Medicine and Surgery (MS4CMS'02)*, Rocquencourt, France, November 2002, pp. 102–107. 11

[42] Y. Ganji and F. Janabi-Sharifi, "Catheter kinematics for intracardiac navigation," *IEEE Trans. Biomed. Eng.*, in press. 12, 13, 15, 20, 38, 71, 110

[43] Y. Ganji, F. Janabi-Sharifi, and A. N. Cheema, "Robot-assisted catheter manipulation for intracardiac navigation," *International Journal of Computer Assisted Radiology and Surgery*, in press. 12, 13, 15, 38, 90, 110, 111

[44] Y. Ganji and F. Janabi-Sharifi, "Kinematic characterization of a cardiac ablation catheter," in *Proc. IEEE/RSJ Int. Conf. on Intelligent Robots and Systems (IROS'07)*, San Diego, CA, Oct 2007, pp. 1876–1881. 12, 15, 20, 38, 71, 110

[45] ——, "Catheter kinematics and control to enhance cardiac ablation," in *Proc.of the SPIE*, vol. 6374, February 2006, p. 63740U. 12, 15, 110

[46] G. Robinson and J. B. C. Davies, "Continuum robots: A state of the art." in *Proc. IEEE Int. Conf. on Robotics and Automation (ICRA'99)*, Detroit, MI, May 1999, pp. 2849–2854. 20

[47] M. W. Hannan and I. D. Walker, "Kinematics and the implementation of an elephant's trunk manipulator and other continuum style robots," *J Robotic Syst.*, vol. 20, no. 2, pp. 45–63, February 2003. 20

[48] B. A. Jones and I. D. Walker, "Kinematics for multisection continuum robots," *IEEE Trans. Robot.*, vol. 22, no. 1, pp. 43–55, February 2006. 20

[49] L. Sciavicco and B. Siciliano, *Modelling and Control of Robot Manipulators*, 2nd ed. Springer, 2000. 20, 31

[50] L. L. Howell, *Compliant Mechanisms*. John Wiley & Sons, Inc., 2001, ch. 7, pp. 261–274. 24, 25, 71

[51] ——, *Compliant Mechanisms*. John Wiley & Sons, Inc., 2001, ch. 5, pp. 135–170. 24, 25

[52] H. Das, J. Slotine, and T. Sheridan, "Inverse kinematic algorithms for redundant systems," in *Proc. IEEE Int. Conf. on Robotics and Automation (ICRA'88)*, 1988, pp. 43–48. 31

[53] D. E. Whitney, "Resolved motion rate control of manipulators and human prostheses," *IEEE Trans. Man-Mach. Syst.*, vol. 10, no. 2, pp. 47–53, 1969. 31

[54] A. Deo and I. Walker, "Overview of damped least-squares methods for inverse kinematics of robot manipulators," *J. Intell. Rob. Syst.*, vol. 14, no. 1, pp. 43–68, 1995. 32

[55] Y. Nakamura and H. Hanafusa, "Inverse kinematic solutions with singularity robustness for robot manipulator control," *ASME J. Dyn. Syst., Meas., Control*, vol. 108, pp. 163–171, 1986. 32

[56] E. Wilson, R. Slack, F. Banovac, S. Dieterich, H. Zhang, and K. Cleary, "Electromagnetic tracker accuracy in the CyberKnife suite," in *Proc. SPIE*, vol. 6141. SPIE, 2006, p. 61411R. 43

[57] C. Nafis, V. Jensen, L. Beauregard, and P. Anderson, "Method for estimating dynamic em tracking accuracy of surgical navigation tools," in *Proc. SPIE*, vol. 6141, 2006, p. 61410K. 43

[58] J. Krücker, S. Xu, N. Glossop, A. Viswanathan, J. Borgert, H. Schulz, and B. Wood, "Electromagnetic Tracking for Thermal Ablation and Biopsy Guidance: Clinical Evaluation of Spatial Accuracy," *Journal of Vascular and Interventional Radiology*, vol. 18, no. 9, pp. 1141–1150, 2007. 43

[59] R. Clavel, "Delta, a fast robot with parallel geometry." in *Symposium on industrial robots (ISIR)*, Sydney, Australia, 1988, pp. 91–100. 47

[60] A. J. Willmott, "VL vector library," http://www.cs.cmu.edu/afs/cs/user/ajw/www/software/, 2002. 48

[61] D. Montgomery and G. Runger, *Applied statistics and probability for engineers.* John Wiley & Sons, 2003, ch. Statistical Intervals for a Single Sample, pp. 247–276. 59

[62] W. H. Press, S. A. Teukolsky, and W. T. Vetterling, *Numerical recipes in C++: the art of scientific computing*, 2nd ed. Cambridge University Press, 2002. 63

[63] J. B. Kuipers, *Quaternions and Rotation Sequences.* Princeton University Press, 1999. 66

[64] G. F. Franklin, J. D.Powell, and M. Workman, *Digital Control of Dynamic Systems*, 3rd ed. Addison Wesley, 1998. 68

[65] D. Timms, M. Hayne, K. McNeil, and A. Galbraith, "A complete mock circulatory loop for the evaluation of left, right, and biventricular assist devices," *Artificial Organs*, vol. 29, no. 7, pp. 564–572, July 2005. 78

[66] J. Brethe, E. Vasselin, D. Lefebvre, and B. Dakyo, "Determination of the repeatability of a kuka robot using the stochastic ellipsoid approach," in *Proc. IEEE Int. Conf. on Robotics and Automation (ICRA'05)*, Barcelona, Spain, 2005, pp. 4339–4344. 80

[67] S. W. Smith, *The scientist and engineer's guide to digital signal processing*. San Diego, CA, USA: California Technical Publishing, 1997, ch. 15, pp. 278–284. 91

[68] B. Schmidt, K. R. J. Chun, R. R. Tilz, B. Koektuerk, F. Ouyang, and K.-H. Kuck, "Remote navigation systems in electrophysiology," *Europace*, vol. 10, pp. iii57–61, 2008. 101

[69] J. Jayender, R. Patel, and S. Nikumb, "Robot-assisted catheter insertion using hybrid impedance control," in *Proc. IEEE Int. Conf. on Robotics and Automation (ICRA'06)*, May 2006, pp. 607–612. 105

[70] Y. Ganji, F. Janabi-Sharifi, and S. Safavi-Naeini, "Towards real-time endocardial boundary detection from intracardiac echocardiographic images: a comparative study," in *Proc. SPIE*, vol. 6147, February 2006, p. 61470P. 108, 111

[71] E. Bengoetxea, "Inexact graph matching using estimation of distribution algorithms," Ph.D. dissertation, Ecole Nationale Superieure des Telecommunications, 2002. 108

[72] C. Lentner, Ed., *Geigy Scientific Tables*, 8th ed. Ciba-Geigy, Basel, Switzerland, 1990, vol. 5 Heart & Circulation, pp. 75–76, 124–125. 112

[73] Y. Liu, P. Allaire, Y. Wu, H. Wood, and D. Olsen, "Construction of an artificial heart pump performance test system," *Cardiovascular Engineering*, vol. 6, no. 4, pp. 151–158, 2006. 115

[74] H. Samavat and J. Evans, "An ideal blood mimicking fluid for doppler ultrasound phantoms," *Journal of Medical Physics*, vol. 31, no. 4, pp. 274–278, 2006. 116

[75] Y. Ganji, "Animal test protocol," University of Waterloo, Tech. Rep., 2008. 124